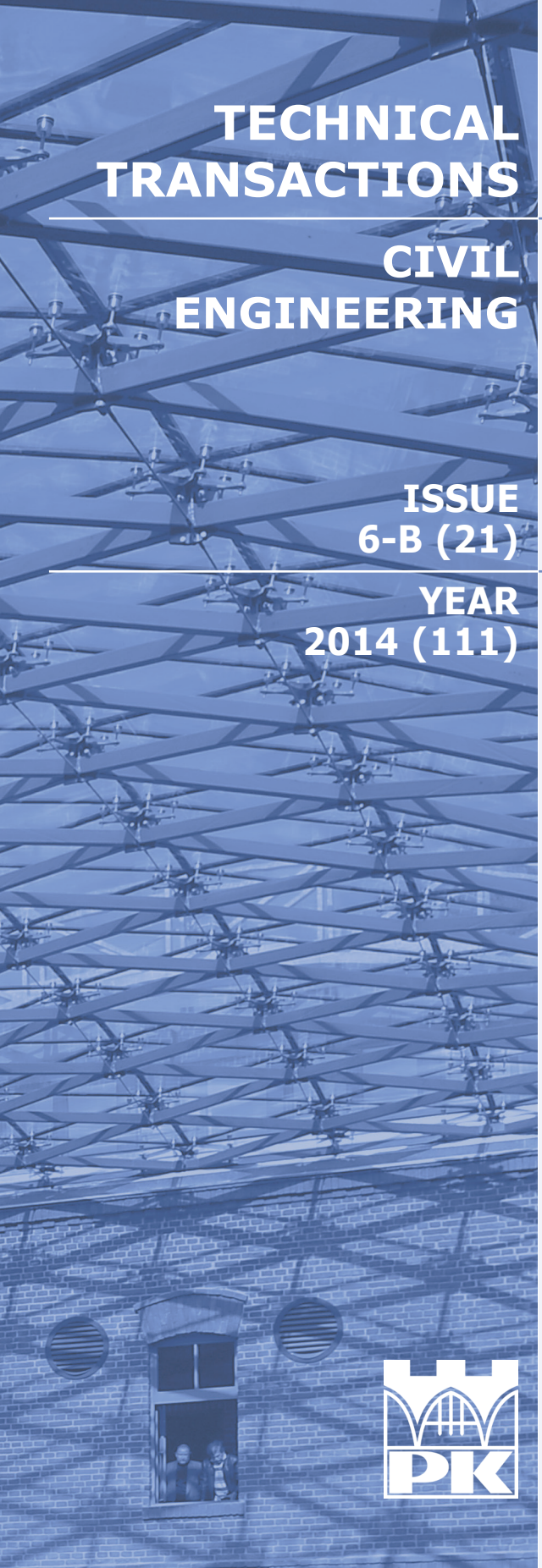

TECHNICAL TRANSACTIONS

CZASOPISMO TECHNICZNE

CIVIL ENGINEERING

BUDOWNICTWO

ISSUE 6-B (21)

ZESZYT 6-B (21)

YEAR 2014 (111)

ROK 2014 (111)

WYDAWNICTWO POLITECHNIKI KRAKOWSKIEJ

TECHNICAL TRANSACTIONS | CZASOPISMO TECHNICZNE

CIVIL ENGINEERING | BUDOWNICTWO

ISSUE 6-B (21) | ZESZYT 6-B (21)
YEAR 2014 (111) | ROK 2014 (111)

Pierwotną wersją każdego Czasopisma Technicznego jest wersja on-line
www.czasopismotechniczne.pl www.technicaltransactions.com

Civil Engineering Series
6-B/2014

TECHNICAL TRANSACTIONS | CZASOPISMO TECHNICZNE
CIVIL ENGINEERING | BUDOWNICTWO
6-B/2014

ŁUKASZ BEDNARSKI*, SŁAWOMIR MILEWSKI**, RAFAŁ SIEŃKO***

DETERMINATION OF VERTICAL AND HORIZONTAL SOIL DISPLACEMENTS IN AUTOMATED MEASURING SYSTEMS ON THE BASIS OF ANGULAR MEASUREMENTS

WYZNACZANIE PIONOWYCH I POZIOMYCH PRZEMIESZCZEŃ GRUNTU W AUTOMATYCZNYCH SYSTEMACH POMIAROWYCH NA PODSTAWIE POMIARÓW KĄTOWYCH

A b s t r a c t

The increasing interest in monitoring systems for soil displacements, prompted the authors to search for calculation methods which would allow the construction of monitoring devices without the need to place sensors in inclinometric tubes. The application of the spline interpolation method and the local approximation method by means of weighted moving squares allowed for the creation of curves which describe the soil deformation with the required accuracy. The basic equations of this calculation method and numerical examples are presented in the paper.

Keywords: *soil deformation measurements*, *inclinometers*, *spline interpolation*

S t r e s z c z e n i e

Wzrastające zainteresowanie systemami monitorowania przemieszczeń gruntów skłoniło autorów do poszukiwania metod obliczeniowych, z wykorzystaniem których możliwe byłoby budowanie urządzeń pomiarowych bez konieczności zabudowy czujników w rurach inklinometrycznych. Zastosowanie metody interpolacji składanej oraz metody lokalnej aproksymacji za pomocą techniki ważonych ruchomych kwadratów umożliwiło zbudowanie krzywych opisujących deformację gruntu z założoną dokładnością. W artykule przedstawiono podstawowe równania metody obliczeniowej oraz przykłady numeryczne.

Słowa kluczowe: *pomiary deformacji gruntu*, *inklinometry*, *interpolacja sklejana*

* Ph.D. Eng. Łukasz Bednarski, AGH University of Science and Technology.
** Ph.D. Eng. Sławomir Milewski, Institute for Computational Civil Engineering, Faculty of Civil Engineering, Cracow University of Technology.
*** Ph.D. Eng. Rafał Sieńko, Institute of Building Materials and Structures, Faculty of Civil Engineering, Cracow University of Technology.

1. Introduction – contemporary design tools

Currently, linear objects are very often located on soils of a high compressibility since terrains of more favourable geological structure are the most often taken by building and other locations are not possible. This causes the necessity to apply various geotechnical methods leading to the strengthening of the subsoil. Often, the economically favourable solution is making an overloaded embankment. Obtaining the soil improvement effect is in this case related to the consolidation of the soil. The consolidation effect is based on the reduction of the soil volume as a result of water outflow and decreasing distances between soil particles. The duration time of the consolidation process depends, first and foremost, on the infiltration coefficient c_v and the load value resulting from the built overload embankment. It has been observed in accurate investigations [1] that increased stress in the soil causes a certain reduction of the consolidation coefficient. This effect, as well as the natural variability of soils, is the reason that the theoretically determined settlement of the improved base and its minimal time can differ from the real situation. Therefore, during the consolidating improvement process performing its constant control is recommended. Apart from the measurements of water pressure changes, the basic parameters describing the effect of soil improvement are vertical and horizontal displacements. Measurements of vertical displacements allow for tracing the consolidation process over time, while horizontal displacement measurements enable controlling the effect of soil driven out from strengthened spaces. More and more often, the automatic monitoring systems which allow for observation of soil displacement both at the stage of object building and during operation, are used for these measurements.

2. Measurement methods of vertical and horizontal soil displacements

The measurement of vertical soil displacements is usually perceivable as measurements of its surface deformation. Broadly understood geodetic surveying methods from the classic levelling, via satellite techniques GPS [2], up to laser scanners, are here applied. However, with regard to the consolidation process, it is essential to observe the soil response to the overload applied in the space where displacements occur, meaning within the improved soil.

The basic way of measuring vertical soil displacements is through the use of plate benchmarks [3]. This measurement allows for determining the soil displacements in the measuring points and at time intervals at which observations are made. More and more often, hydraulic prophilometers, manual or automatic, are used for measuring the vertical soil displacements. Hydraulic prophilometers are devices in which the sensor measures the hydrostatic liquid pressure change caused by changes of the measured value in relation to the assumed reference point. Vertical soil displacements in the selected places can also be measured by means of indenting extensometers or individual points of hydraulic measurement.

The best known and the most commonly applied method is taking inclinometric measurements [4]. These measurements allow for determining vertical as well as horizontal displacements. This method is used both for manual measurements and for building automated measuring systems tracing the consolidation process.

3. Inclinometric measurements

Inclinometric measurements are based on determining shape changes of the inclinometric tube placed in the soil due to the ground deformation. The measurement is done by means of the probe called the inclinometer. The measurement can be done manually, by an individual probe shifted along the inclinometric tube or automatically by stable inclinometers (a few or several dozen inclinometers connected together). Angular positions n of measured segments (probes) of a known length L are determined (Fig. 1). These items of information are then recalculated into vertical or horizontal displacements, depending on the kind of task. The input data are as follows:

- total length, at which the measurement is done, L_t,
- number of measuring sensors (segments, probes, protractors) n, connected by articulated joints of length L: ($L = L_t / n$),
- angles of inclination of individual probes α_i, $i = 1,\ldots, n$, (acc. to Fig. 1), in their middle points,
- reference height d (height of the first point of the segment).

Measuring sensors determine points of the broken line situated on the original curve. Coordinates can be calculated from the equation:

$$\begin{cases} x_i = L\cos(\alpha_1) + L\cos(\alpha_2) + \ldots + L\cos(\alpha_{i-1}) = L\sum_{j=1}^{i-1}\cos(\alpha_j) \\ d_i = d + L\sin(\alpha_1) + L\sin(\alpha_2) + \ldots + L\sin(\alpha_{i-1}) = d + L\sum_{j=1}^{i-1}\sin(\alpha_j) \end{cases}, \quad i = 1,\ldots,N \tag{1}$$

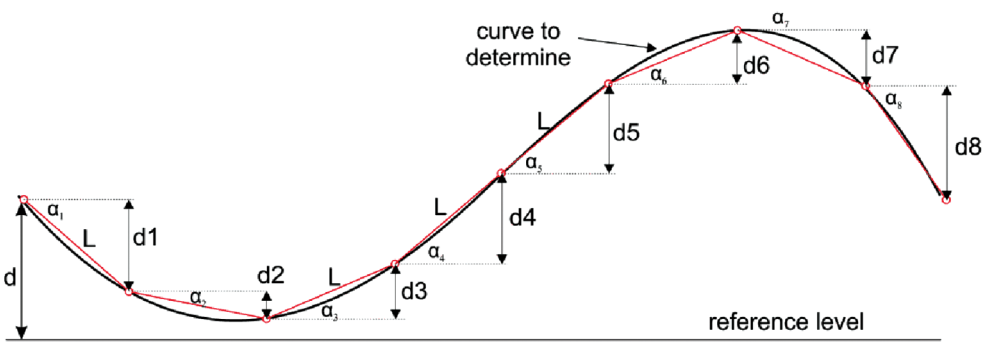

Fig. 1. Principle of inclinometric measurements

This solution (later referred to as the 'simplified solution') allows for obtaining the displacement in an arbitrary point of the segment by connecting points of coordinates (1) with straight segments (broken line). Then, the vertical soil displacement function can be written in one equation, joining with each other straight lines in individual segments:

$$d(x) = a_1 x + a_2 + \sum_{i=2}^{N-1} b_i \left(x - x_i\right)_+, \quad \left(x - x_i\right)_+ = \begin{cases} x - x_i, & \text{for } x > x_i \\ 0, & \text{for } x \le x_i \end{cases} \tag{2}$$

where:

$$a_1 = \frac{d_2 - d_1}{x_2 - x_1}, \quad a_2 = d_1 - a_1 x_1 \tag{3}$$

and:

$$b_j = \frac{d_{j+1} - \left(a_1 x_{j+1} + a_2\right) - \sum_{i=2}^{j-1} b_i \left(x_{j+1} - x_i\right)}{x_{j+1} - x_j}, \quad j = 2, 3, \ldots, N-1 \tag{4}$$

Points (1) are lying on the original curve, with the accuracy determined by the protractor measuring precision (measuring range). In spite of the simplicity of such an approach, the solution does not correspond with real soil deformation. It can be expected that the largest errors will occur in the middle of the measuring segments.

4. Inclinometric measurements in automated monitoring systems

Inclinometric measurements can by easy read autamatically. Sets of stable inclinometers are placed in previously prepared vertical measuring openings or in horizontal tubes. After connecting them to the device reading the data, the automatic monitoring system is ready – this allows for a very fast measurement of the soil displacement profile. The read-out of all sensors from the given measuring cross-section requires only a few seconds. This provides the possibility of tracing, for example, the consolidation process and the soil displacement from under the over-loaded embankment during building works and adjusting their successive stages to the progressing consolidation process. Automatic systems can be equipped with additional sensors, e.g. of the water pore pressure measurements.

High equipment costs constitute a significant limitation in the inclinometric measurements automation. The measuring probe length is usually 1 meter. This means that, for the profile 30 meters long, the measuring chain should consist of 30 sensors. Additionally, for communicating with sensors, a recording device of 30 channels is needed. One of the ways of decreasing the costs of the monitoring system can be the elongation of measuring probes. However, this operation has physical limitations relating to the diameter of standard inclinometric tubes and to the bending stiffness of the measuring probes.

To avoid these limitations, it is possible to place special probes directly into the soil. However, in this case, it is necessary to take into account length changes of the measuring set due to soil deformation. When inclinometric tubes are applied, the above problem does not exist since the measuring chain retains its length displacing itself inside the tube. Length changes of the measuring chain do not allow the application of simple equations for the measured results analysis.

Thus, there is a need for development of the measuring method which would allow the above mentioned limitations to be overcome. Information on an angular position of each measuring segment must be recalculated into vertical soil displacements in a way which would enable making the automatic measuring system without the need for protecting tubes.

5. Complex calculation methods of soil displacement and assessment of their accuracy

The problem of identifying vertical soil displacement on the basis of data concerning angular positions of measuring segments requires solving the mathematical approximation task [6], [7], i.e. in general cases, fitting the curve to the measured data.

Defined in such a way, the complex solution not only better describes the real soil movements after deformation, but can also serve as the accuracy indicator of the obtained previously simplified solution (1). This solution will be determined in the form of a curve of the proper order (e.g. multinomial), Fig. 2, which will be controlled by fitting to the measuring points of coordinates:

$$\begin{cases} x_i = \dfrac{L}{n}(i-1) \\ d_i = L\mathrm{tg}(\alpha_1) + L\mathrm{tg}(\alpha_2) + \ldots + L\mathrm{tg}(\alpha_{i-1}) = L\sum_{j=1}^{i-1}\mathrm{tg}(\alpha_j) \end{cases}, \quad i = 1,\ldots,N \tag{5}$$

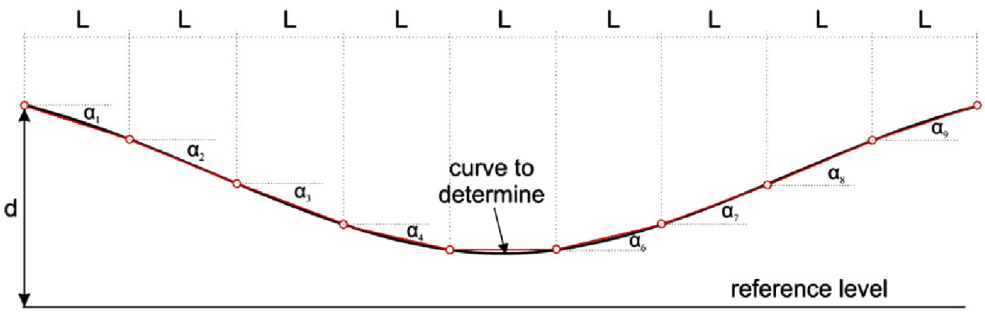

Fig. 2. Principle of determining the subsidence curve by means of the complex solution

The simplest approximation, in the result of which the curve will be obtained, is the interpolation [5], [7]. The interpolation simplicity relies on the fact that the curve passes through all given points and that this is the only condition which has to meet. Out of various interpolation techniques, the most often the so-called Lagrange's interpolation formula is applied:

$$d(x) = \sum_{i=1}^{N} d_i L_i(x), \quad L_i(x) = \prod_{\substack{j=1 \\ j\neq i}}^{N} \frac{x - x_j}{x_i - x_j} \tag{6}$$

However, this formula has a significant limitation. In a similar fashion, as in each multinomial interpolation, at a large N, the solution in between points can become unstable, especially at the segment ends. This phenomenon is called Runge's effect and most often occurs in cases when, for large numbers of initial data, the original function (given either in a continuous or discrete way) indicates large differences in values (large gradients). Therefore, in practice, the applicability range of equation (6) is also limited.

Another interpolation technique applied here is the so-called spline interpolation [7], in which curves of low orders (most often 2 or 3) are applied on individual segments which are then splined together in such a manner as to retain the continuity of the function and its successive derivatives (determined by the curve order). Its certain variant is the broken line (2), for which only the function continuity is ensured. In the case of the spline square interpolation, the equation for the displacement can be written as:

$$d(x) = a_1 x^2 + a_2 x + a_3 + \sum_{i=2}^{N-1} b_i \left(x - x_i\right)_+^2, \quad \left(x - x_i\right)_+^2 = \begin{cases} \left(x - x_i\right)^2, & \text{for } x > x_i \\ 0, & \text{for } x \le x_i \end{cases} \tag{7}$$

where coefficients a_1, a_2, a_3 are the solution to the set of equations:

$$\begin{cases} d(x_1) = d_1 \\ d(x_2) = d_2 \\ d'(x_1) = \mathrm{tg}\left(\alpha_1\right) \end{cases} \Rightarrow \begin{cases} a_1 x_1^2 + a_2 x_1 + a_3 = d_1 \\ a_1 x_2^2 + a_2 x_2 + a_3 = d_2 \\ 2a_1 x_1 + a_2 = \mathrm{tg}\left(\alpha_1\right) \end{cases} \Rightarrow \begin{cases} a_1 = \ldots \\ a_2 = \ldots \\ a_3 = \ldots \end{cases} \tag{8}$$

And coefficients b_i, $i = 2, 3, \ldots, N - 1$ are resulting from the following recurrence formula:

$$b_j = \frac{d_{j+1} - \left(a_1 x_{j+1}^2 + a_2 x_{j+1} + a_3\right) - \sum_{i=2}^{j-1} b_i \left(x_{j+1} - x_i\right)^2}{\left(x_{j+1} - x_j\right)^2}, \quad j = 2, 3, \ldots, N-1 \tag{9}$$

The application range of equation (7) is wider than of equation (6). Solutions by means of spline functions are worth being applied when the measurement data are numerous ($N >> 6$), and the soil deformation is relatively mild (modelling of depressions, hillsides).

The last method discussed here is the interpolation method, this is a local approximation method by means of the weighted moving squares technique [6]. In a similar fashion as in the case of spline curves, local multinomial curves of low orders are used, however, they are ascribed to points not to segments, and their passing through the given points is controlled by weighted function. Its singularity in the given points assures interpolation properties of the final curve in spite of coefficients selected by approximation (minimisation of errors understood as the weighted sum of squares of deviation values on the curve and the given value).

The local curve (multinomial of a low order) is built on a group of a few points from the nearest vicinity of the point for which the approximation value is needed. A group of such points is called a star. The number of star points (m) depends on the task

dimensionality and on the curve order. For the parabola (p = 2) at least 3 points should be taken, but no more than 6–10 (for more points, the curve loses the local character). In order to determine the displacement of the arbitrary point x, the following matrix values should be calculated:

$$\underset{[m\times s]}{\boldsymbol{P}(x)} = \begin{bmatrix} 1 & h_1 & \frac{1}{2}h_1^2 \\ 1 & h_2 & \frac{1}{2}h_2^2 \\ \dots & \dots & \dots \\ 1 & h_m & \frac{1}{2}h_m^2 \end{bmatrix}, \quad \underset{[m\times m]}{\boldsymbol{W}(x)} = \begin{bmatrix} \omega_1(x) & 0 & \dots & 0 \\ 0 & \omega_1(x) & \dots & 0 \\ \dots & \dots & \dots & \dots \\ 0 & 0 & \dots & \omega_m(x) \end{bmatrix} \tag{10}$$

$$\underset{[s\times m]}{\boldsymbol{M}(x)} = \left(\boldsymbol{P}(x)\boldsymbol{W}(x)\boldsymbol{P}(x)\right)^{-1}\boldsymbol{P}(x)\boldsymbol{W}(x)$$

where s – number of approximation parameters ($s = p + 1$), $h = x_i - x$ and:

$$\omega_i(x) = \frac{1}{|h|^{2(p+1)} + \varepsilon} \tag{11}$$

ε is a very small number, corresponding to the calculating accuracy (e.g. $\varepsilon = 10^{-16}$ for the real type of dual precision). Then, the displacement is expressed by the equation:

$$d(x) = \sum_{i=1}^{m} M_{1,i}(x)d_i \tag{12}$$

This method can be successfully applied in cases where there are a lot of measuring results and the soil deformation is highly variable (e.g. in the case of a fault or hole). A certain difficulty in its application can constitute the fact that the analytical form of the curve is unknown – its calculation by a point after point according to equations (10)–(12) is possible.

Each of the complex equations (6), (7) and (12) can be used for the assessment of the simplified solution quality (2). A difference between the simplified solution and one of the complex solutions should indicate the true error of the simplified solution, which for real measurements, will not be known. Whereas the error of complex solutions can be assessed in a few ways. Analogous to the assessment of the simplified solution error, curves of higher orders than in the case of (7) and (12) can be built. It is also possible to retain the same order (second), but instead to build interpolations on a larger number of data. In this case, angular measurements can be supplemented by additional virtual data calculated on the basis of the complex solution.

6. Numerical examples

With the aim of testing the measuring data, at the length L_t = 30 m, were simulated by means of curves not being multinomial (of ordinates from the range ± 0.5 m). Calculated angles were additionally disturbed within limits of the measuring accuracy of protractors (± 0.1% of the measuring range (–10° 10°) i.e. ± 36’’). The data prepared in such a way were used in controlling calculations.

Three commonly occurring types of soil deformations, differing in their forms and in number of extreme points, were subjected to analysis. Results of calculation for each type of deformation are shown in the figure (Figs. 3–5). The calculations were performed for the configuration of n = 10 or 30 inclinometers (of the same length).

The upper diagram (Figs. 3–5) contains:

- accurate solution (on which angles were found) – dashed blue line,
- simplified solution (2) – dotted pink line,
- one selected complex solution (typical for the given deformation form) – solid red line.

The lower diagram (Figs. 3–5) contains solution errors and their assessments:

- accurate error of the simplified solution (difference between the simplified solution and the accurate mathematical solution) – dotted pink line,
- estimated error of the simplified solution – dotted green line,
- accurate error of the complex solution – dashed blue line,
- estimated error of the complex solution – solid red line.

Maximum displacement values of the module and errors are given in diagram headings. The first case constitutes a large, basin type soil subsidence, which may be modelled by equation (6) or (7). Equation (7) and a configuration of 10 inclinometers of a length L = 3 m were used in calculations. The results are presented in Fig. 3.

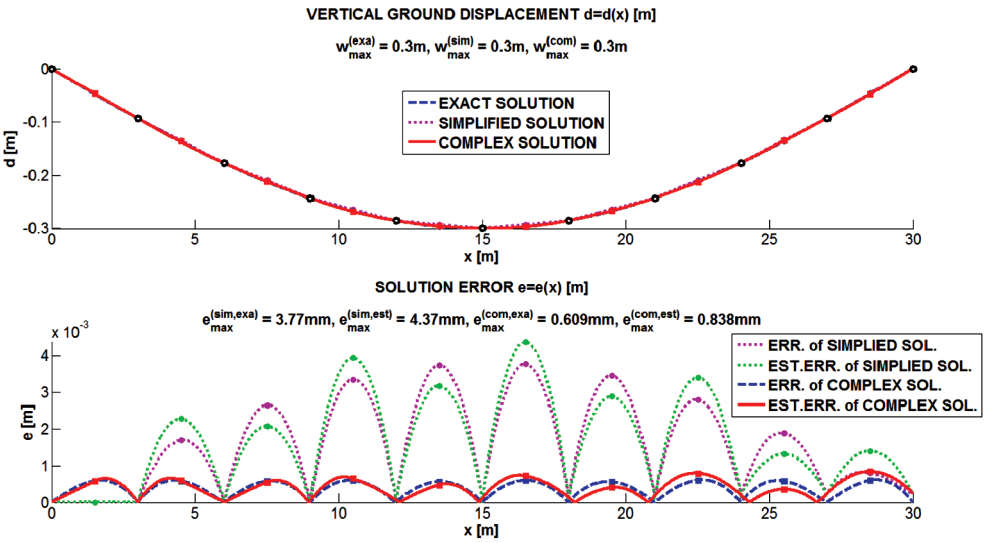

Fig. 3. Calculation results for the first form of the soil deformation (configuration of 10 inclinometers)

The error of the complex solution is one order smaller, and the solution successfully estimates the simplified solution error.

The second case constitutes the slope and its model will be the spline square interpolation, calculated according (7). The results, also for $n = 10$, are presented in Fig. 4.

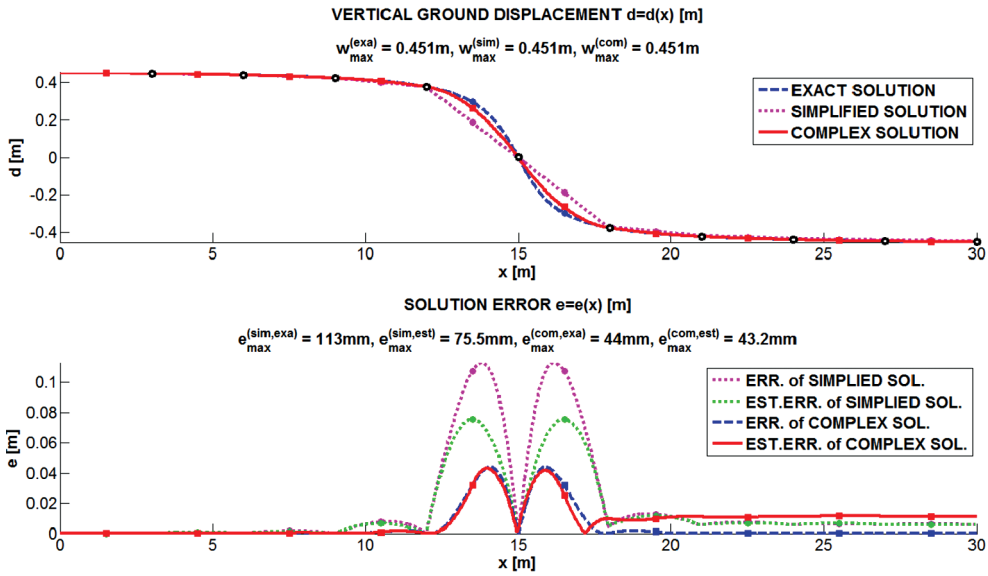

Fig. 4. Calculation results for the second form of soil deformation (configuration of 10 inclinometers)

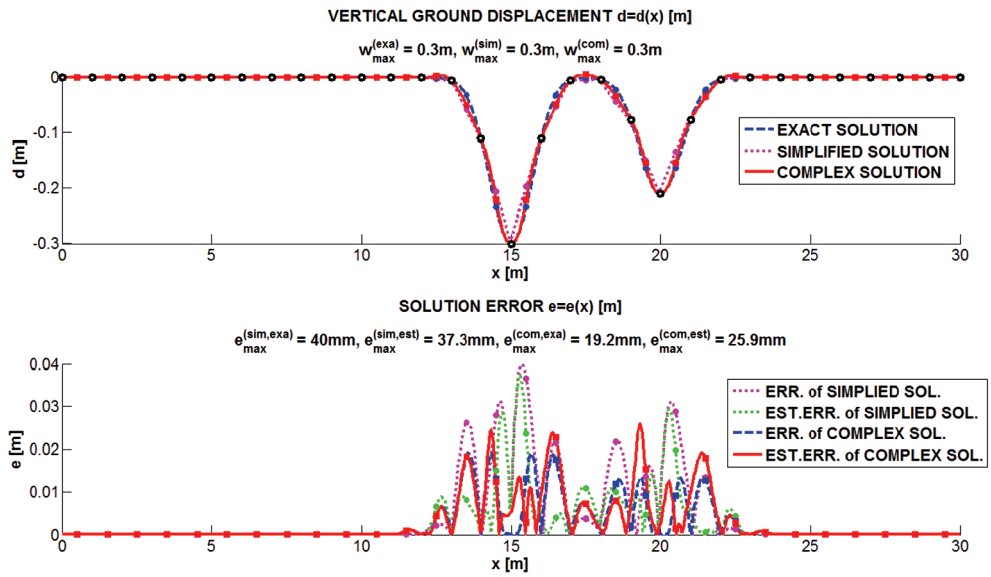

Fig. 5. Calculation results for the third form of soil deformation (configuration of 30 inclinometers)

The last case (3rd) constitutes two crater type depressions of different depths. The configuration of $n = 30$ inclinometers with a length $L = 1$ m each, and the local weighted approximation (10)–(12) were used in calculations. The results are presented in Fig. 5.

The estimated errors can be used not only in statements of how accurate was the solution, but also, for example, the optimal planning of numbers and placements of measuring sensors. For the second calculation example there is a need for an increased number of sensors in the middle zone and of decreased outside it. One of the plans for the discussed system is checking its usefulness for the dynamic measurements of bridges.

7. Conclusions

The presented method of analysis of data obtained from the measurement chains built from inclinometric rods allows:

– improvement of the result accuracy in cases of applying the classic inclinometric measurements,
– performance of measurements of soils displacements by means of measuring chains, without protecting tubes.

Renouncement of using inclinometric tubes, the method allows the building of automated systems of significantly long measuring elements, and to achieve sensible costs of building the measuring system.

Two methods of fitting curves to measured data were presented and discussed here. The commonly applied simplified technique is based on the assumption of there being straight segments between the measuring sensors, constituting the straight broken line (first order spline function). Though it interpolates data points, its accuracy is usually low, with the highest errors located between the sensors. The second, more complex approach, is based on mathematical approximation methods, like Lagrange interpolation, spline functions of the higher orders (2, 3), and the most general method, local approximation generated by moving the least squares. The numerical tests performed clearly showed that these methods reproduce the actual solution (soil displacement) in a much more accurate manner, especially in cases where solution gradients are high (ground collapse or hillsides). Moreover, these solutions may be applied as the error estimators for the simplified solution, if necessary.

References

[1] Skutnik Z., Borowczyk M., Krysiak S., *Long term pore water pressure measurements for effective stress evaluation in Warsaw clays*, Proc. of the 13th Danube-European Conference on Geotechnical Engineering, Ljubljana 2006, 113–118.

[2] Hu J., Li Z.W., Sun Q., Zhu J.-J., *Three-Dimensional Surface Displacements From InSAR and GPS Measurements With Variance Component Estimation*, Geoscience and Remote Sensing Letters, IEEE, Vol. 9, Issue 4, 2012, 754–758.

[3] Mikkelsen P.E., *Advances in inklinometer data analysis*, Symposium of Field Measurements in Geomechanics, FMGM, Oslo, Norway 2003.
[4] Cichoń Cz. et. al., *Metody komputerowe w liniowej mechanice konstrukcji, wybrane zagadnienia*, Wydawnictwo PK, Kraków 2009.
[5] Lancaster P., Salkauskas K., *Curve and Surface Fitting*, Academic Press, 1986.
[6] Press W.H., Teukolsky S.A., Vetterling W.T., Flannery B.P., *Numerical Recipes*, Cambridge University Press, 2007.

TECHNICAL TRANSACTIONS | CZASOPISMO TECHNICZNE
CIVIL ENGINEERING | BUDOWNICTWO
6-B/2014

PIOTR BĘTKOWSKI*, ŁUKASZ BEDNARSKI**, RAFAŁ SIEŃKO***

STRUCTURAL HEALTH MONITORING OF A RAIL BRIDGE STRUCTURE IMPACTED BY MINING OPERATION

SYSTEM MONITOROWANIA KONSTRUKCJI MOSTU KOLEJOWEGO PODDANEGO ODDZIAŁYWANIU EKSPLOATACJI GÓRNICZEJ

A b s t r a c t

Structures located in areas affected by mining operation are subjected to movements and tilting. Continuous monitoring of the structure's response to these forces allows for the control of their impact on the technical condition of the structure. In the case of railway structures, the measurements may allow further determination of the impact of modifications to the geometry of the structure on the track. This paper presents the results of observing indications of Structural Health Monitoring installed on an actual bridge construction under which mining operations were being conducted.

Keywords: *Structural Health Monitoring (SHM)*, *mining deformations*, *bridge*, *displacement measurement*

S t r e s z c z e n i e

Obiekty zlokalizowane na terenach podlegających wpływom eksploatacji górniczej ulegają przemieszczeniom i przechyłom. Ciągłe monitorowanie odpowiedzi obiektu na wymuszenia pozwala kontrolować ich wpływ na stan techniczny konstrukcji. W przypadku obiektów kolejowych pomiary mogą umożliwiać dodatkowo określanie wpływu zmiany geometrii konstrukcji na torowisko. W artykule zaprezentowano doświadczenia z obserwacji wskazań systemu monitorowania zainstalowanego na rzeczywistym obiekcie mostowym, pod którym prowadzona była eksploatacja górnicza.

Słowa kluczowe: *systemy monitorowania konstrukcji (SHM)*, *deformacje górnicze*, *most*, *pomiar przemieszczeń*

* Ph.D. Eng. Piotr Bętkowski, Faculty of Civil Engineering, Silesian University of Technology.
** Ph.D. Eng. Łukasz Bednarski, AGH University of Science and Technology.
*** Ph.D. Eng. Rafał Sieńko, Institute of Building Materials and Structures, Faculty of Civil Engineering, Cracow University of Technology.

1. Introduction

Mining operations can cause damage to structures [1]. The basis for the control of the technical condition of the structure is information gathered regarding the occurring changes. Obtaining such information is possible through regular inspections, surveying, and by installing an automatic Structural Health Monitoring system [2–4]. Bridge structure susceptible to terrain deformation requires constant monitoring of its geometry. The use of an automatic SHM system allows for an increased quality and accuracy of information relating to the changes occurring within the structure, while reducing the amount of work for data acquisition and analysis, resulting in a significant increase in the safety of the structure [5, 6]. This paper presents an analysis of the requirements to control the structural health of a bridge structure and presents the first results of the automatic SHM system installed on the structure, within the proximity of which, mining operations are conducted.

2. Location and description of structure

The presented railway bridge is located in Pawłowice over Wyzwolenia Street and the Pawłówka stream. The street and stream intersect with the axis of the structure at a near right angle. The stream is a small body of water in a partially fortified bed.

The bridge is located on the 23.449 km railway line No. 159 Orzesze–Wodzislaw Slaski, trail Warszowice-Studzionka station branch. On the bridge, or rather two parallel bridges, two railway tracks are laid – one track on each of the structures.

Railway No. 159 is heavily loaded. Intense cargo and passenger traffic make repairs on the bridge structures difficult.

Fig. 1. View of the east side of the bridge

The bridge consists of two parts which are separate structures. These two structures are assigned individual tracks:

- under track No. 1 is a riveted steel structure,
- under track No. 2 is a welded steel structure.

Each structure is a two-span design, with two simply supported girders. In each of the spans there are twin steel plate girders. The bridge deck was designed to be open. The intermediate support (pillar) was designed from reinforced concrete, abutments are placed on a mound, and the wings are made parallel to the axis of the track.

2.1. Track 1 – riveted steel bridge (west)

This is an older structure, erected in 1946. The components are joined using steel rivets. The construction of the bridge consists of two long main spans (23.7 m each) and two short spans, with a much smaller cross-section, which are about 2.0 m in overall length, and extend beyond the main plate girders by 1.6 m (Fig. 2) . These spans, due to their short length and low stiffness, do not significantly affect the performance of the main girders. The bearings at the outer ends of the spans mainly limit their deflection.

Fig. 2. View of the abutment and span

The geometry of the structure:

- horizontal clearance: 2 × 20.7 m (two main spans),
- length of each span: 26.9 m (with abutments),
- vertical clearance: 8.15 m (over the road),
- total length: approximately 60 m (including abutments).

2.2. Track 2 – welded steel bridge (east)

The newer of the two parallel structures was erected in 1973 as a steel-welded beam bridge. Abutments of the bridge under track No. 2 were separated from abutments under track No. 1 by movement joints. The pillar (intermediate support) was added to the existing bridge pillar under track No. 1 in such a way that they form a single structure.

The geometry of the structure:

- horizontal clearance: 2 × 22.5 m,
- lenght of each span: 27.50 m,
- vertical clearance: 8.20 m,
- total length: approximately 60 m (including abutments).

3. Mining operation

Geodetic measurements have been performed practically since the beginning of the exploitation of coal deposits in the area of the bridge, i.e. from May 1973, by the mine KWK Pniówek. Before that date, there was no mining operation in the area. The support settlement measured from May 1973 to April 2014 was:

- north abutment approximately 2.09 m,
- south abutment approximately 1.89 m.

Horizontal displacements from March 1994 to April 2014 (before the year 1994, there were no regular abutment distance measurements):

- abutments distance under track No. 1 was reduced by 83 mm (in the axis of the track),
- abutments distance under track No. 2 was reduced by 80 mm (in the axis of the track).

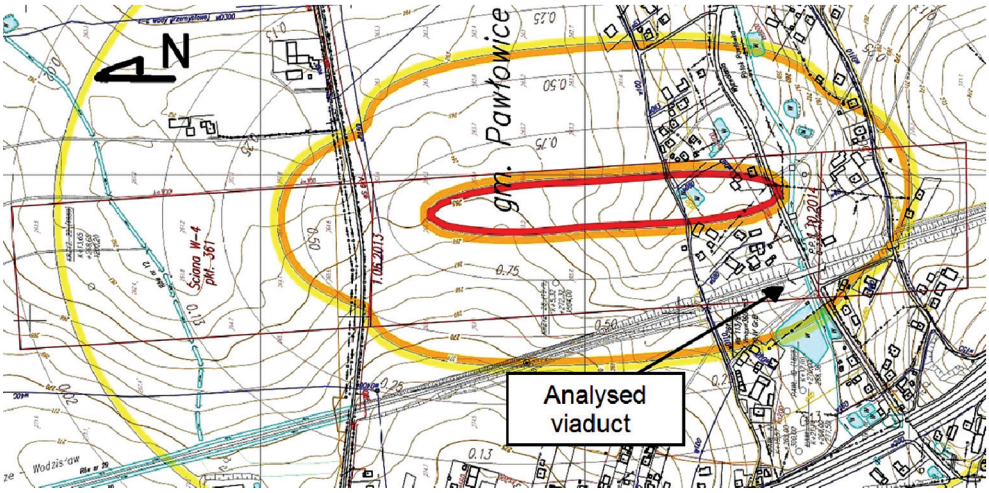

Fig. 3. The position of the bridge related to deck W4. The map of subsidence

A tilt of the abutments relative to the axis of the bridge (the track) was observed, this has resulted in changes in the distance of the abutments' edges. For example, under track No. 2 this distance decreased by 88 mm on the east side and 72 mm west side.

There have been no measurements of the width of the expansion gaps and bearing displacements (despite the fact that displacement transducers are mounted on the bearings).

Currently, in the area of the viaduct, exploitations are being conducted (in wall W4, deck 361 at a depth of approximately 900 m below ground level).

The thickness of the exploited layer is 2.6 m. Influences of the previous exploitation conducted in the area in early 2012 already revealed themselves on the surface – hence, the currently measured terrain deformation should relate to wall W4, 361 deck (Fig. 3).

In the autumn of 2013, this wall was moving closer to the structure (dispersion measured in the area). In summer of 2014, mining operations passed under the structure (axis of the wall was located east of the structure). Completion of the mining operation in wall W4 should occur the fall of 2014. The center of subsidence's the basin associated with this wall will be located southeast of the structure, and the viaduct will be on the side of subsidence's basin.

The time period for the effects of the exploitation to manifest themselves on the surface, is anywhere from about 2 months to as long as 1.5 years. This time period depends upon the geological structure of the rock above – the greater the strength of the rocks, the later the effects of mining on surface will reveal themselves and generally, the increase of deformation occurs faster.

Currently (beginning of July 2014), there is a downhill creep on the site, the abutments are getting closer to each other. Eventually, in connection with the exploitation of wall W4 (deck 361), it is estimated that it is possible for the abutments to get as close as approximately 60 mm.

Projected values of ground deformation (at the end of 2014):

- $w = -0.40$ m (subsidence),
- $T_{II} = 1.0$ mm/m (deflection in the vertical plane parallel to the axis of the bridge / the south-bound track),
- $T_{\perp} = -1.7$ mm/m (deflection in the plane perpendicular to the axis of the bridge / the east-bound track),
- $\varepsilon_{II} = -1.2$ mm/m (creeping in the plane of the axis of the bridge / track),
- $\varepsilon_{\perp} = -0.6$ mm/m (creeping in a plane perpendicular to the axis of the bridge).

In 2011, a complete survey of the bearings was performed identifying the current horizontal displacements of the platform relative to the supports; measurements of width of expansion gaps, the grade line and lateral inclination of the tracks were made. Utilizing mining projections, an evaluation of current and required capabilities of kinematic spans was conducted. It has proved necessary to reconstruct the bearings and adjust the width of certain expansion gaps. It has been calculated that by 2020, each of the abutments can get as close as 150 mm to the central pillar. At the end of 2012, the structure was adjusted to 2020 mining forecasts which would influence the structure.

4. Need for monitoring

Real dangers associated with the planned mining exploitation:

- creeping (compression) of land is forecasted, which will cause the abutments to approach each other,
- tall cracked the pillar of reinforced concrete is prone to deflection and horizontal forces,
- one-directional bearings might become locked as a result of the twisting of abutments – in this structure, there are slide bearings and roller bearings. Slide bearings (bridge under track 1) and roller (track 2) work properly only if the displacements occur along one axis. In the analysed case, the nature of deformation is inclined to the structure, the abutments and the pillar can thus be twisted relative to the axis of the structure. In instances of locking of the bearings, new cracking of the pillar and abutments would occur. It is also possible for damage or even destruction of the fixed supports and bearings to occur.

The structure is sensitive to the torsion of the abutments, as the one-directional plain bearings become rapidly wedged in the case of simultaneous rotation and linear horizontal displacement of the outer supports. As a result of this phenomenon, the ability of the span to move independently relative to the abutments. This creates a couple of horizontal forces in the horizontal plane. The spans, which are not prepared for such a bending moment, are at risk. Also, the cracked pillar is not resistant to shearing forces in the lower plane bearings. In order to ensure safety of the structure, it is important to perform frequent rectification of the lower plates of the bearings to eliminate the impact of abutment torsion on the span.

Due to the complex geotechnical conditions in the area of the structure (the presence of the stream), the nature of deformation is difficult to predict. The pillar is built on native soils (clay sands, silt sands and clays dominate in the soil). Substantial force is transferred from the pillar on to the ground due to heavy weight (half the weight of the two spans plus rolling stock). Abutments are placed on an embankment, they have large foundation plates, are low and carry the load only from the middle of the spans each.

In the area of the bridge, multiple mining operations are carried out in various directions in relation to the structure, this means that the influences of individual operations overlaps in time.

These factors make the predicted values of horizontal displacement of the past significantly different from the measured values, hence it is necessary to conduct regular surveying and possibly re-adjust the position and width of the of the bearing joints before 2020.

5. Structural Health Monitoring

In October of 2013 on the eastern part of the structure, automatic Structural Health Monitoring system was installed. The system consists of an observation subsystem, responsible for collecting information and data transfer, as well as acting as a warning subsystem responsible for the analysis of the obtained measurement results and informing the user about forthcoming hazards. In accordance with ITB Instruction 443/2009 [7], this device can be classified into the group of SHM systems.

As physical parameters, which change and have impact on the changes of the technical condition of the structure, were selected. In the analysis of the structure's deformation, it was assumed that each element behaves like a rigid body [8].

The location of the measuring points and the principle of signing the values of linear and angular displacements are shown in Fig. 4.

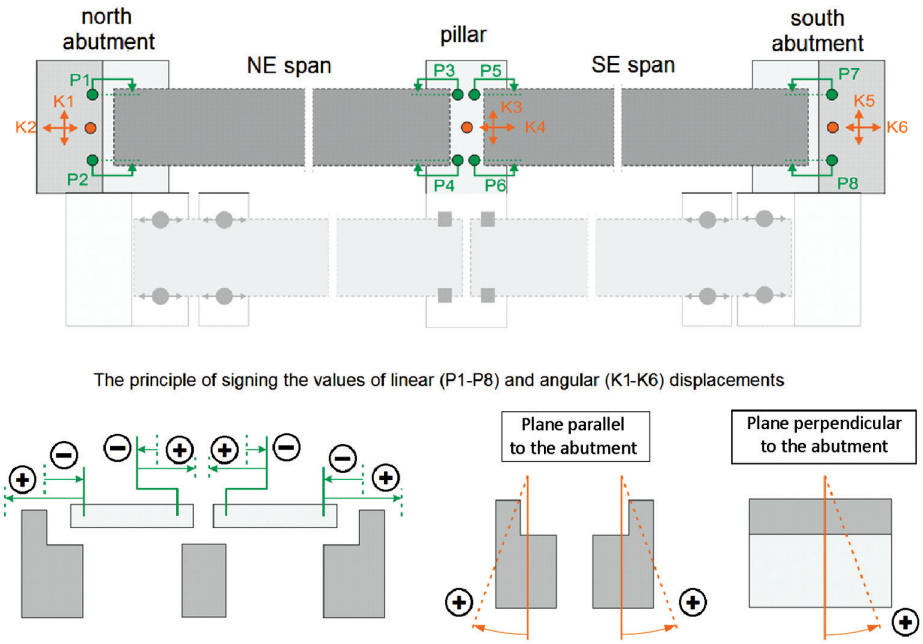

Fig. 4. Distribution of measurement points: P – measurements of horizontal displacement, K – measurements of supports angles

Fig. 5. Support structures for mounting angle sensors and displacement sensors at the intermediate support (view on the west side)

Due to the planned 10-year monitoring period, stringed displacement sensors (transducers) were utilized with a measuring range of 200 mm as well as string angle sensors.

The system is powered by battery, replaced during the periodic inspections of the structure. The sensors are read every 15 minutes, and once a day, readings are sent via the GSM network to the measuring server where they are processed and automatically analysed. The system generates daily reports on the structure's behaviour and sends them to the persons responsible for its safety.

6. Measurement results

System installation and start of data collection in the fall of 2013 allowed observing the beginning of the unfolding impact of mining activities on the monitored object. Changing in the span distances relative to the abutments was observed at the beginning of April 2014. During this time, the mining operations passed under the structure.

The negative sign in measurements on the charts below indicates closing of the expansion gaps. The increase in horizontal displacements is particularly visible on the northern abutment (sensors P1 and P2 in Fig. 6).

The non-existence of a linear relationship between of displacements recorded by sensor P2 with temperature changes demonstrates either locking of or permanent damage to the bearings on the support of the structure.

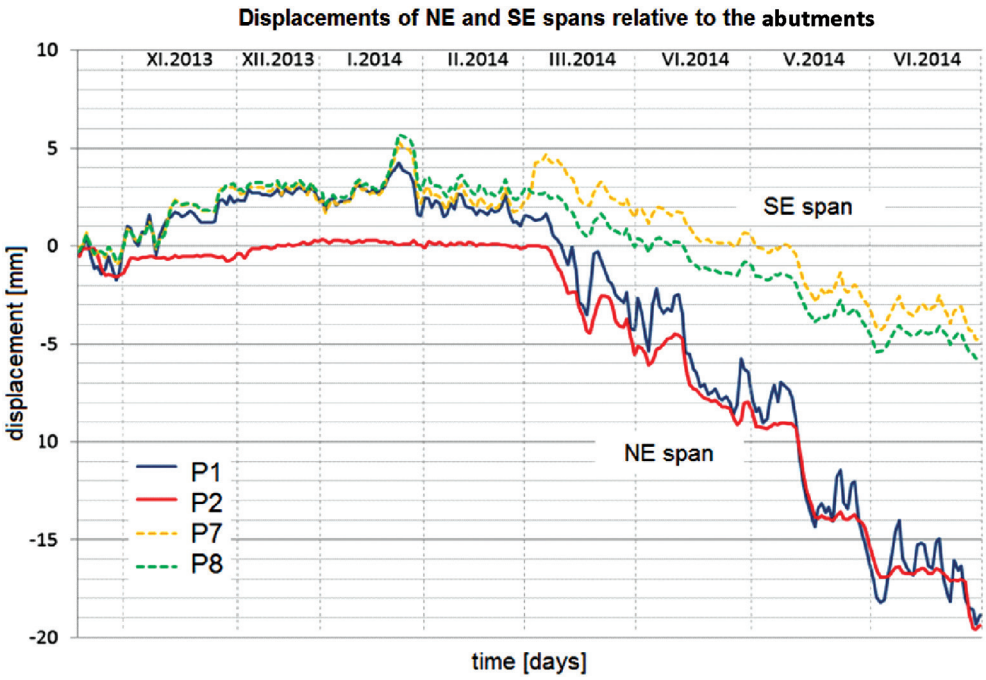

Fig. 6. Graph of horizontal displacements (along the axis of the structure) NE and SE spans relative to abutments

Displacements of spans relative to immovable intermediate support (the pillar) were observed. Values added for the NE span prove displacement towards the abutments. Part of the measured horizontal displacements are related to the depletion of slack in connections between the plate girders of the bridge, the steel support and the reinforced concrete pillar. Unfortunately, there is certainly deformation and twisting of the pillar relative to its axis.

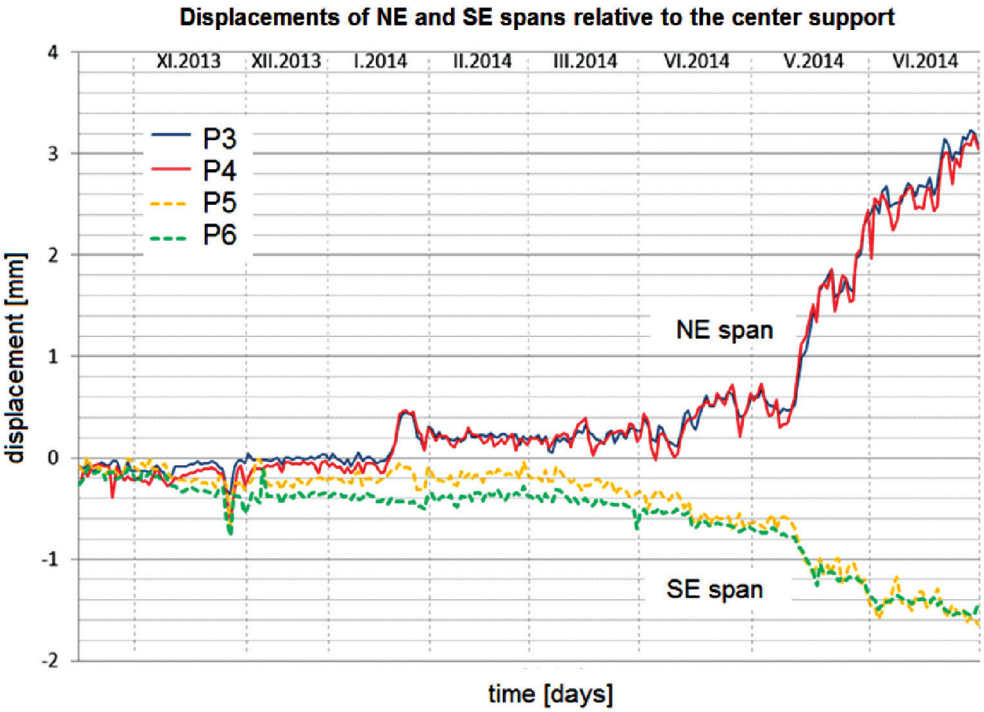

Fig. 7. Graph of horizontal displacements (along the axis of the structure) NE and SE spans relative to center support

The observed linear horizontal displacements were confirmed by the angular displacement of the abutments and the pillar. In those measurements, parts of the bridge were treated as rigid.

Figure 8 shows changes in the inclination of the north-east and south-east abutments in the period from November 2013 to June 2014. Analysis in a vertical plane parallel to the axis of the structure's angular displacement values (sensors K2 and K6), together with the values of horizontal displacements relative to the abutments and measured with sensors P1, P2, P7 and P8 shows that the abutments are getting closer. The value of this approximation in the foundation level is greater than in the level of the support platform. The horizontal displacement of the north and south abutments, resulting from their rotation, assuming the theoretical height from ground level of H = 8 m, is suitably X_N = 7.0 mm (in direction N) and X_S = 4.2 mm (in direction S). Displacements resulting from horizontal movement of abutments are respectively equal to $P_{NE} \approx 20$ mm

and $P_{SE} \approx 5$ mm, wherein $P_{NE} = 0{,}5(P1 + P2)$ and $P_{SE} = 0{,}5(P7 + P8)$. If we sum up the values of displacements resulting from the horizontal movement and the rotation of the abutments, we calculate the value of creeping at ground level at 36.2 mm. Projected deformation of land is forecasted to be approximately –1.2 mm/m, which at a distance of approximately 45 m between the abutments, allows assessment of their horizontal displacement at around 54 mm. This means that at present, creeping is already about 67% of the forecasted figure.

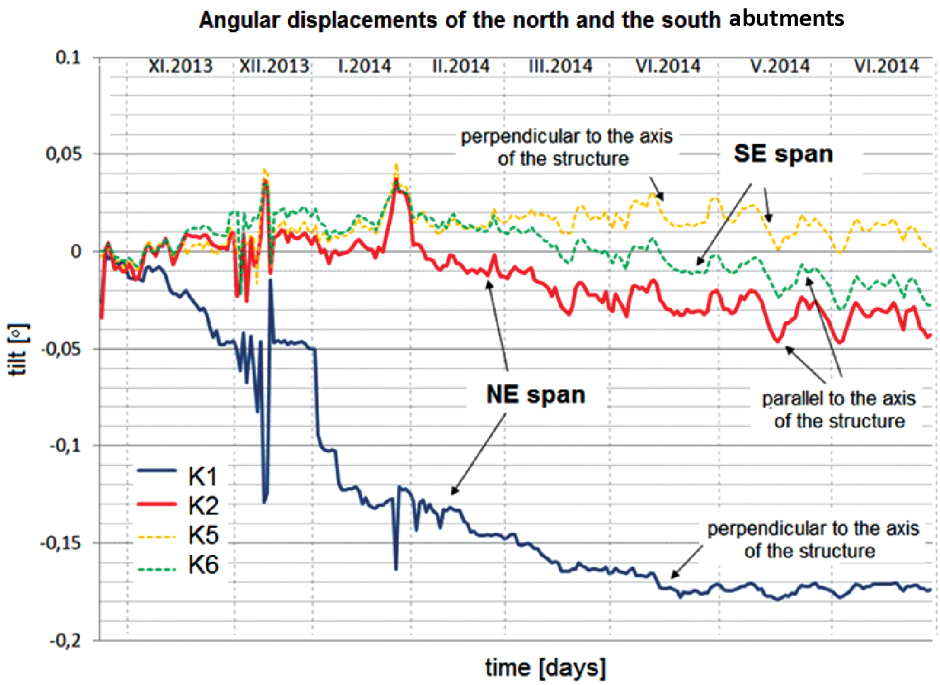

Fig. 8. Chart of tilting of the northern and southern abutments in a plane parallel and perpendicular to the axis of the structure

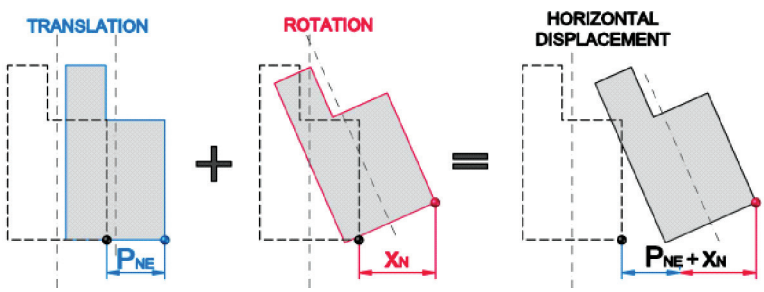

Fig. 9. Horizontal displacement of the north abutment resulting from translation and rotation

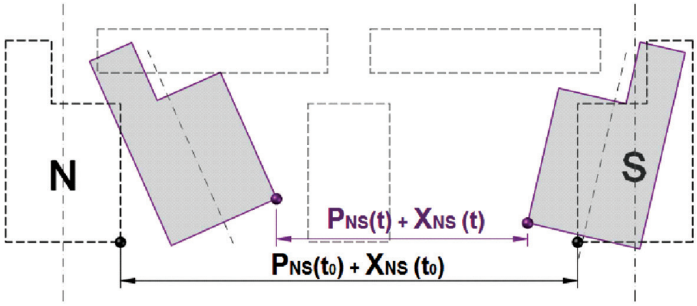

Fig. 10. Relative displacement of abutments – visual drawing

An interesting observation is the measurement of the tilt of the northeastern abutment in a plane perpendicular to the axis of the tracks. The value of the measured angle is now K1 ≈ –0.18°. This means that the abutment (assuming the theoretical amount H = 8 m) is tilted so that the upper part of the structure has moved approximately 25 mm to the west. Such behaviour of the northeastern support may result in the observed locking (wedging) of rolling bearings (probe P2).

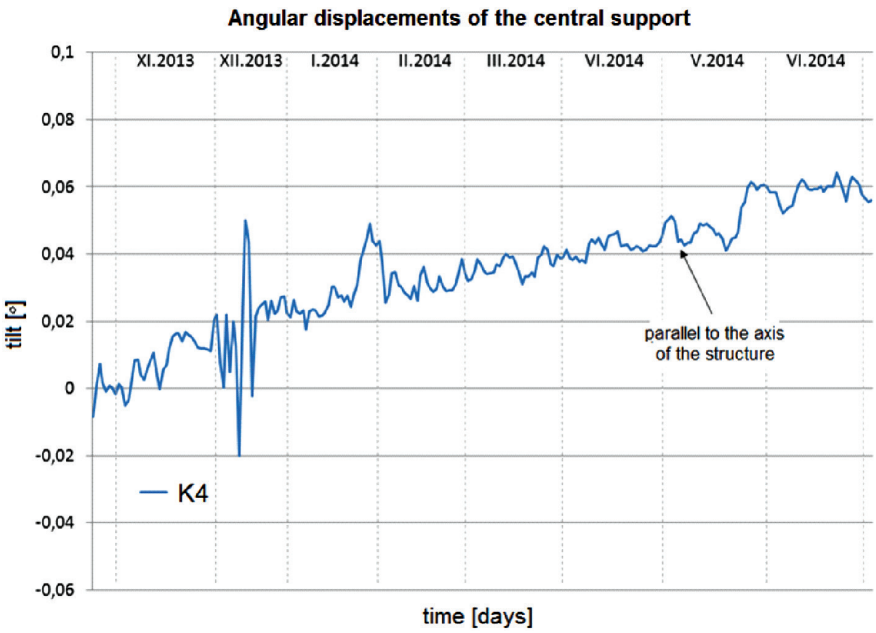

Fig. 11. Chart of tilting support in plane parallel to the axis of the structure ('+' denotes a tilt towards the north)

The above findings inconsistent with the forecasted indicator of deformation, which in this plane, is $T_{\perp}$ = 1.7 mm/m (deflection in the plane perpendicular to the axis of the bridge on the eastbound track) at a height of abutment equal to 8 m – this should mean a displacement

of the upper surface of the support of 14 mm in the opposite direction to that which was measured.

Noteworthy is the fact that the southeastern abutment is not subject to tilting in the plane perpendicular to the axis of the bridge.

The measurement of the tilt of intermediate support (the pillar) in the plane of the object's axis (Fig. 11) indicates that the pillar tilted towards the north so that the horizontal displacement of its head is currently approximately 8.4 mm.

7. Remarks and conclusions

Structures situated in areas influenced by land deformation caused by mining, are subject to movements and tilts. Anticipating these extortions enables the design of structures adapted to variable geometry of the land. Ongoing monitoring of the structure's response to these extortions allows for the control of their impact on the technical condition of the structure. In the case of railway structures, the measurements may allow further determination of the impact of changes in the geometry of the structure on the track.

Structures in areas where mining activities are carried out are often subjected to overlapping deformations derived from the extractions form different coal deposits in different directions. Installation of Structural Health Monitoring allows for regular measurements without the involvement of human resources. In view of the long disclosure period of the mining operation influences, this solution ensures the proper conduct of observations.

Continuous access to the measurements via a dedicated measurement platform as well as the ability to define the threshold values at which the monitoring system will automatically take action related to, for example, sending information about risk to the persons responsible for the structure creates a significant increase in its security and allows active management such as the movement of rolling stock.

The Structural Health Monitoring system installed on the structure in Pawłowice already provided very important information, a moment was captured in which the terrain deformation caused modification of the geometry of the bridge. Currently, there is monitoring of the horizontal displacements relative to the support, therefore, it was possible to point out the support in which blocking occurs and recommend changing the direction of the bearing work. The control of horizontal displacement in the place of the theoretically fixed central support allows for the monitoring of the technical condition of the split top plate of the reinforced concrete pillar and permanent bearings – this has a real consider changing to 'significant, positive' impact on the safety of the structure.

Real dangers for the structure are the breaking (cutting) of permanent bearings on the pillar and blocking of one-way roller bearings on abutments. Monitoring system allows to notice the displacement on permanent bearings and the lack of transfers on moving bearings in the certain period of time what allows controlling both threats and in the emergency e.g. immediately close the viaduct for the railways.

Analytical evaluation (computational) of the influence of mining deformations on the height concentration tension of structure is, in this case, inappropriate. A large numbers of variables, for example, those relating to damage (splits, cracks) of the pillar and abutments, and certain visible deformations of the geometry of steel girders as a result of earlier mining

deformations, are important factors which make it difficult to create a good computational model. Additionally, the mining extortion is slowly growing, a redistribution of stresses is scheduled and as a result, the inner strength of the structure will fall – this phenomenon is not well understood and requires further research.

The use of simple geometrical relationships allowed the estimation of deformation in the area and for comparing the findings with the forecasted values.

Given the amount of information provided by SHM systems and the various possibilities of their use in practice, it seems that in the near future, the number of bridges located within mining areas equipped with this type of device will significantly increase.

References

[1] Bętkowski P., *Obserwacja i naprawa dwuprzęsłowego stalowego mostu kolejowego położonego na terenach górniczych*, [w:] *Ochrona obiektów na terenach górniczych*, praca zbiorowa (monografia) pod red. A. Kowalskiego, GIG, Katowice 2012, 17–25.

[2] Kadela M., Bednarski Ł., *Wytyczne obserwacji ciągłej obiektów zlokalizowanych na terenach górniczych*, Przegląd Górniczy, 8/2014, 78–84.

[3] Parkasiewicz B., *Monitoring przemieszczeń elementów budowlanych w warunkach prowadzenia eksploatacji górniczej na przykładzie obserwacji wiaduktu w Rudzie Śląskiej*, Przegląd Górniczy, 8/2012, 83–91.

[4] Kadela M., *Systemy monitorowania obiektów liniowych na terenach górniczych*, Materiały z konferencji naukowo-technicznej zorganizowanej w ramach XII Dni Miernictwa Górniczego i Ochrony Terenów Górniczych, Brenna 2013, 163–172.

[5] Salamak M., Weseli J., Radziecki A., *Monitoring of highway bridges in areas under mining exploitation influence*, 5th International Conference on Current and Future Trends in Bridge Design, Construction and Maintenance, Beijing, China, 17–18 September 2007, 469–478.

[6] Sieńko R., *Monitorowanie konstrukcji budowlanych a wzrost ich bezpieczeństwa*, Przegląd Budowlany, 4/2007.

[7] Instrukcja ITB 443/2009. System kompleksowego zarządzania jakością w budownictwie. Bezdotykowe metody obserwacji i pomiarów obiektów budowlanych, Warszawa 2009.

[8] Salamak M., *Obiekty mostowe na terenach z deformującym się podłożem w świetle kinematyki brył*, Wydawnictwo Politechniki Śląskiej, Gliwice 2013.

TECHNICAL TRANSACTIONS | CZASOPISMO TECHNICZNE
CIVIL ENGINEERING | BUDOWNICTWO
6-B/2014

JACEK BOROŃ*

SELECTED QUALITATIVE CHANGES TO THE SOLVING OF ENGINEERING OPTIMIZATION PROBLEMS

WYBRANE ZMIANY JAKOŚCIOWE W ROZWIĄZYWANIU INŻYNIERSKICH PROBLEMÓW OPTYMALIZACJI

Abstract

This article presents and describes some qualitative changes that have occurred in the engineering design of building structures over the last forty years. With widespread access to computers and the development of software tools, optimization problems, which in the nineteen--seventies were solved analytically or, when justifiable, using mathematical machinery (e.g. first Polish minicomputers type Odra 1,300) are now often settled through the use of specialized add-ins to spreadsheets. This state of affairs has created a basis for significant changes in the quality of educational opportunities in the context of construction faculties within technical universities. These changes are illustrated with a simple example of the optimization (determination of the *dimensions of the beam subjected to bending).*

Keywords: *engineering design*, *mathematical programming*, *optimizers*

Streszczenie

W artykule przedstawiono i opisano zmiany jakościowe, jakie zaszły w projektowaniu inżynierskim konstrukcji budowlanych na przestrzeni ostatnich czterdziestu lat. Dzięki powszechnemu dostępowi do komputerów i rozwojowi oprogramowania narzędziowego problemy optymalizacji, które w latach siedemdziesiątych ubiegłego stulecia były rozwiązywane analitycznie lub tylko w uzasadnionych przypadkach za pomocą maszyn matematycznych (tak wtedy określano pierwsze minikomputery typu Odra 1300), są obecnie rozwiązywane za pomocą m.in. dodatków do arkuszy kalkulacyjnych. Taki stan rzeczy stworzył podstawy do istotnych zmian jakościowych także na polu możliwości edukacyjnych na wydziałach budowlanych uniwersytetów technicznych. Wspomniane zmiany zilustrowano przykładem optymalizacji przekroju poprzecznego belki zginanej.

Słowa kluczowe: *projektowanie inżynierskie*, *programowanie matematyczne*, *optymalizatory*

* Ph.D. Eng. Jacek Boroń, Faculty of Civil Engineering, Wroclaw University of Technology.

1. Introduction to the nature of the optimization

According to [3], the optimization of civil engineering structures involves, inter alia, choosing the geometric parameters and strength properties of both structural elements and entire structures. This choice entails searching for the extreme values in terms of specific criteria. The searching process is conducted in an objective and rational manner, therefore, without the need to draw on a designer's intuition, special skills or professional experience. In this way, optimization replaces the part of the design process which entails the selection of shapes and dimensions and then checking the strength conditions and other constraints. Due to its specific nature, certain experts label the optimization of civil engineering structures as the synthesis of structures. The question is whether the optimization can and should replace the design process in its traditional sense, i.e. is the goal of optimization to include all the variables and parameters defining the structure so that a solution to an optimization problem is tantamount to obtaining the target structural design? The author of this paper does not think it is possible to provide a clear-cut answer to this question at the present time, as an optimization problem involving all the variables and parameters of a more complex structure might turn out to be impossible to solve, or looking for such a solution might be pointless due to e.g. a lot of effort required and high computational costs. In such cases, it is advisable that a rigorously formulated optimization problem involves only part of the variables and parameters, and that a designer decides about the second part, because in the mathematical model for optimization there will always be variables and parameters which are obvious and which should not burden the optimization. The goal of synthesis is to avoid arbitrariness during, for example, the process of selecting structure shapes, as optimization aims to determine the relations between internal forces, shape parameters, and the distribution of material, which in turn should undoubtedly bring multilateral benefits. To sum up the above considerations, although the optimization of civil engineering structures should be counted among the methods of structural mechanics or of the so-called general theory of optimization, and should not be considered as an economic activity, like any other technical activity, it still concerns economic issues.

2. Understanding how optimization software works

This paper now presents an illustration of the issue by presenting the standard add-in to the MS Excel® spreadsheet. The add-in is called Solver® and is developed by Frontline Systems. Although MS Excel® has only been equipped with the basic version of Standard Excel Solver® since 1997, the add-in's computational capabilities are able to solve problems which contain even several dozen decision variables and the same number of constraints. What else makes this add-in a useful tool? Most of all, a simple user interface which can be grasped even by people with only a general idea of how to use spreadsheets. The Excel Solve® interface does not deter designers with extensive mathematical nomenclature or complex formulas, nor does it force users to design on their own or probe the essence of the applied mathematical procedures.

The primary objective of the Excel Solver® optimization software is to find a solution to a problem – that is, to determine the values for the decision variables which satisfy all

constraints (imposed on both the individual decision variables and the relationships between them) whilst at the same time, providing the extreme value (i.e. the minimum or maximum value) of a single objective function (which is a kind of yardstick of the solution quality and the function of the aforementioned decision variables). A well-formulated mathematical model of optimization is always solvable, but the solution time can be different and depends, perhaps above all, on the following three features of that model:

- The size of the model (understood as the number of decision variables and constraints, which translates into the total number of equations to be solved);
- The mathematical relationships (i.e. linear or non-linear) between the objective and constraints and the decision variables;
- The possibility of applying integer constraints (which entails a requirement that the area of feasible solutions includes only whole number values and involves the use of the methods of discrete optimization, which prolong the solution time).

Other issues, such as poor scaling, can also affect the solution time and quality, but the three above-mentioned features affect the intrinsic solvability of a problem (represented with a mathematical model). Naturally, the time needed to find a solution can also be reduced by faster algorithms and faster processors; however, solving some of the non-convex (i.e. concave) or non-smooth problems can take years, even with the fastest computers conceivable.

The total size of the mathematical model and the use of integer constraints can quite easily be assessed as early as the stage of examining the correctness and suitability of the model itself. A much harder task is to assess the mathematical relationships in the model, and it is these relationships which often have a decisive impact on the quality of the solution and on how long it takes to find a solution.

Summing up [4]:

- If the objective function and the constraints are linear functions of the decision variables (i.e. the latter are raised to the power of one), there is a fair chance that it will be possible to find a globally optimal solution (a globally conditional extreme value) relatively quickly, given the size of the mathematical model. In addition, such a linear problem is labelled as convex, this means that all the functions occurring therein are also convex. The best method for solving such problems is the Simplex LP Solving Method [7].
- If the objective function and the constraints are smooth non-linear functions of the decision variables (i.e. the latter are raised to the power other than the power of one), the search for a solution will take longer. If, in addition, the problem is convex (see Fig. 1a)), it is certain that at a global optimum will be reached. However, if the problem is non-convex (see Fig. 1b)), even finding a locally optimal solution might prove difficult. The best method for solving this type of problem is the GRG Nonlinear Solving Method.
- If the objective function and the constraints are non-linear and non-smooth, and the problem is also non-convex (in practice, if you use e.g. the spreadsheet IF, CHOOSE or LOOKUP functions that use some or all of the decision variables), the best you can obtain is a so-called good solution (which is better than the initial values, but is neither a locally nor a globally optimal solution). A whole range of Evolutionary Solving Methods has been developed in order to solve such problems.
- It may happen that within one problem, there is a desire to use integer, binary, and any other constraints and solve this problem with all the three Solving Methods mentioned above. However, this will make such a problem non-convex and all the more difficult to solve.

With the Simplex LP Solving Method, while searching for a globally optimal solution, a solution may be encountered that is close to optimal (only slightly worse in quality and still worthy of attention) and found much quicker. On the other hand, with the GRG Nonlinear and Evolutionary Solving Methods, in most cases it is expected to lead to a good, but probably not optimal, solution (and therefore not the best one).

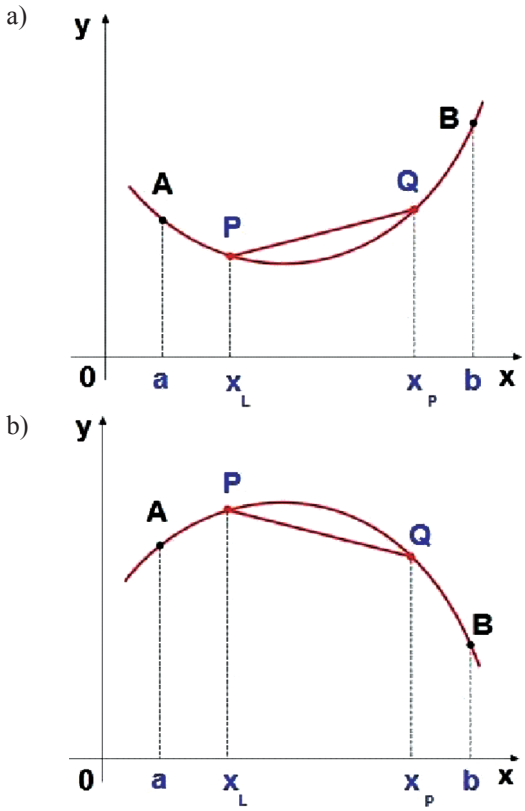

Fig. 1. Graphical representation of problems: a) convex problem and b) concave problem

3. Possible applications and computations

3.1. Rectangular wooden cross-section, graphical and analytical solution

Using the simplest example possible, the summary of which is taken from [5], we will show the difference between traditional designs (also known as intuitive or classic) and optimal designs (which is a kind of synthesis that uses mathematical programming).

The task is to design a rectangular cross-section of a wooden beam which is able to transfer a pre-set bending moment *M*.

$$M = 167 \text{ kNm} = 0.167 \text{ MNm}$$

The allowable stress (σ_{dop}) for the beam's material is:

$$\sigma_{dop} = 10.00 \text{ MPa}$$

The beam will fulfil its function if it is able to transfer the pre-set bending moment (i.e. the stress in the beam's cross-section does not exceed the allowable values). Naturally, the designed girder must demonstrate sufficient protection against the loss of stability while bending. To simplify this task, this condition has not been explicitly formulated, but it will be satisfied once the beam's cross-sectional dimensions remain within practically reasonable limits. The ratio of cross-sectional dimensions should therefore adopt the tested values which guarantee sufficient protection against the loss of stability.

In traditional design, the course of action is to adopt some numerical values (width and height of the beam's cross-section), use these values in the beam stress formula and check whether this condition is satisfied. If the stress exceeds the allowable value σ_{dop}, a designer must adjust the dimensions accordingly and use them in the formula once again. This procedure is repeated until stress σ remains within the allowable value limits σ_{dop}.

$$\sigma = \frac{M}{W} = \frac{6 \cdot M}{b \cdot h^2} \leq \sigma_{dop}$$

where:

- b, h – beam cross-sectional dimensions: b – width and h – height,
- M – the previously mentioned bending moment; it was assumed M = 167 kNm (0.167 MNm),
- W – section modulus of rectangle; it was assumed $W = (b \cdot h^2)/6$,
- σ_{dop} – allowable stress; it was assumed σ_{dop} = 10.00 MPa (both its value and dimensioning method were adopted for illustrative purposes only).

A designer will try to 'use' the cross-section to the fullest, i.e. to choose its dimensions (b and h) so that the resulting stress values are close to the allowable limits. In further considerations, it will become whether achieving the allowable stress values is really sufficient to make the most of the material. Once the cross-section dimensions which do not exceed the beam stress limits are found, the problem is practically solved, i.e. the designed cross-section of the beam is able to transfer the pre-set bending moment (the only limitation of optimization).

However, the question of whether the selected cross-section is optimal (in other words – the best), cannot be satisfied with only one variant of the cross-section even if the allowable stress values have been reached – that is, even if the cross-section is 100% used. This is insufficient because you cannot be sure that the selected cross-sectional dimensions of the beam are the best of all possible options. In order for a girder to be optimal, it is not enough if it only fulfils its task of being able to transfer the pre-defined bending moment, as it is certainly possible to design beams with other cross-sectional dimensions which would also satisfy these requirements. Therefore, it must be clarified what is meant by saying that one design is better than the other. For this purpose, a criterion for assessing the quality of a design solution will have to be specified. The most frequently used criterion is the economic criterion,

representing the generalized cost of a structure. In this example, the girder quality assessment criterion has been associated with the area of the beam's cross-section. The optimal girder will have the smallest cross-sectional area of all the girders able to transfer the pre-defined bending moment. It is obvious that a designer can design and compare only a limited number of girder variants, and that there will always be a possibility of there being another structure which has a smaller cross-sectional area and is therefore better. This possibility is always present in traditional design.

For example, in a rectangular cross-section of the following dimensions:

$$b_{\mathrm{I}} = 40 \text{ cm} = 0.40 \text{ m}$$

$$h_{\mathrm{I}} = 50 \text{ cm} = 0.50 \text{ m}$$

$$A_{\mathrm{I}} = b_{\mathrm{I}} \cdot h_{\mathrm{I}} = 40 \cdot 50 = 2{,}000 \text{ cm}^2 = 0.2 \text{ m}^2$$

where:

A_{I} – cross-sectional area of the first, pre-established girder,

the bending moment M stated earlier yields the following stress values:

$$\sigma = \frac{M}{W} = \frac{6 \cdot M}{b_{\mathrm{I}} \cdot h_{\mathrm{I}}^2} = \frac{6 \cdot 0{,}167}{0.40 \cdot 0.50^2} = 10.00 \text{ MPa}$$

$$\sigma = 10.00 \text{ MPa} = \sigma_{dop} = 10.00 \text{ MPa}$$

On the other hand, in a rectangular cross-section of the following dimensions:

$$b_{\mathrm{II}} = 20 \text{ cm} = 0.20 \text{ m}$$

$$h_{\mathrm{II}} = 71 \text{ cm} = 0.71 \text{ m}$$

$$A_{\mathrm{II}} = b_{\mathrm{II}} \cdot h_{\mathrm{II}} = 20 \cdot 71 = 1{,}420 \text{ cm}^2 = 0.142 \text{ m}^2$$

where:

A_{II} – cross-sectional area of the second, pre-established girder,

the bending moment M stated earlier yields the following stress values which do not fully utilize the stress limits:

$$\sigma = \frac{M}{W} = \frac{6 \cdot M}{b_{\mathrm{II}} \cdot h_{\mathrm{II}}^2} = \frac{6 \cdot 0.167}{0.20 \cdot 0.71^2} = 9.92 \text{ MPa}$$

$$\sigma = 9.92 \text{ MPa} < \sigma_{dop} = 10.00 \text{ MPa}$$

However, let us consider the areas of these cross-sections:

$$A_{\mathrm{I}} = 0.2 \text{ m}^2 > A_{\mathrm{II}} = 0.142 \text{ m}^2$$

From the above, it follows that the beam with the cross-section A_{II} is better than the previous beam (in terms of the adopted criterion) but in this way, it is still impossible to compare all the possible projects of beam cross-sections (i.e. possible pairs of numbers for *b* and *h*). Let us now formulate the mathematical conditions of stability which were not explicitly stated earlier. To this end, it is necessary to determine the limits for the ratio of cross-sectional dimension of the girder. It must be noted that in this example, these limits are not derived from the stability conditions, but are adopted arbitrarily (now we are interested in principles and not the accuracy of the numbers). We assume that the ratio of cross-sectional dimension of the beam must satisfy the following conditions:

$$\frac{h}{b} \geq 1.00 \text{ (square or rectangular cross-section)}$$

$$\frac{h}{b} \geq 4.00 \text{ (rectangular cross-section, with the appropriate proportions)}$$

In addition, the optimality condition has been added, this defines the minimum cross--sectional area of the girder:

$$A = b \cdot h = \text{minimum}$$

The example includes only two variables which allow for a graphical representation of the task on the plane. Let us adopt a Cartesian coordinate system where the cross--section height *h* is on the horizontal axis, and the cross-section width *b* is on the vertical axis (see Fig. 2). The coordinates of each point from the first quarter of the plane may be the dimensions of the beam's cross-section. Conversely, each girder cross-section of width *b* and height *h* can be represented as a point of this plane. Let us also present on this plane an area bounded by the above specified conditions. The first condition can be represented graphically on the plane after replacing the inequality for the allowable beam stress with the equality, and after substituting *M* and σ_{dop} for numerical values. Next, the equality has to be transformed so that the *b* dimension becomes the function of the *h* dimension.

$$\sigma = \frac{M}{W} = \frac{6 \cdot M}{b \cdot h^2} = \sigma_{dop}$$

$$\frac{6 \cdot 167\,\text{kNm}}{b \cdot h^2} = 10{,}000 \text{ kN/m}^2$$

$$b = \frac{1}{h^2 \cdot 10}$$

Therefore:

Condition no. 1 is shown as constraint no. 1: $b = \dfrac{1}{h^2 \cdot 10}$,

condition no. 2 is shown as constraint no. 2: $b = h$,

and condition no. 3 is shown as constraint no. 3: $b = \dfrac{h}{4}$.

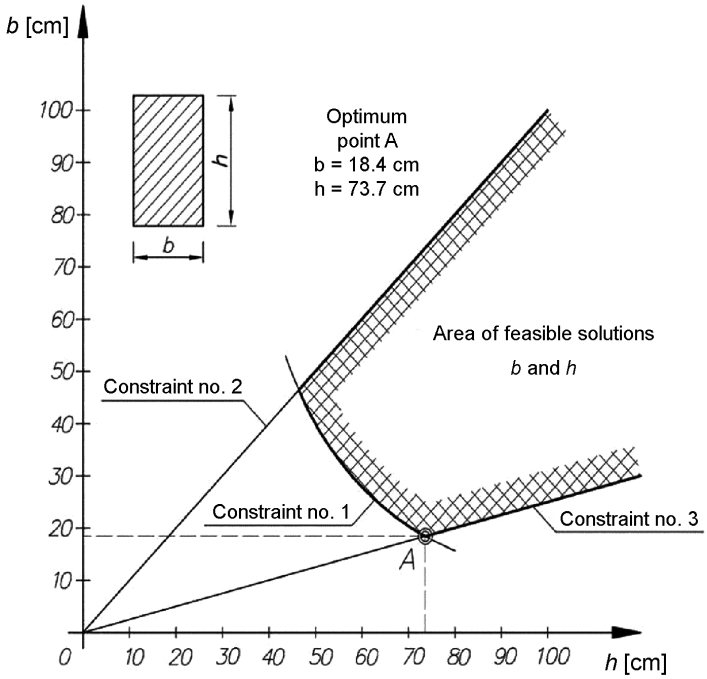

Fig. 2. Optimization of a rectangular cross-section of a bending beam

As shown by the figure above, the point A (the optimum) lies at the intersection of the lines drawn according to the following equations:

$$\begin{cases} b = \dfrac{1}{h^2 \cdot 10} \\ b = \dfrac{h}{4} \end{cases}$$

Solving the above system of equations has yielded the optimum cross-sectional dimensions of the beam:

$$b = 18.4 \text{ cm} = 0.184 \text{ m}$$

$$h = 73.7 \text{ cm} = 0.737 \text{ m}$$

3.2. Rectangular wooden cross-section, numerical solution using Standard Excel Solver®

Let us now solve the same problem with the popular optimization software. First, it is necessary to place the mathematical model in the spreadsheet: the decision variables *b* and *h* (cells H59:H60); the optimization criterion (formula $z = b \cdot h$ in cell H62); the constraints (definitions in cells B62:B64; see Fig. 3).

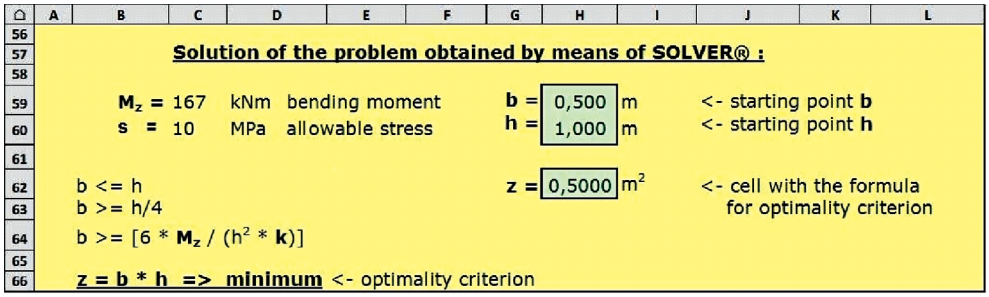

Fig. 3. Fragment of the spreadsheet with the essential elements of the optimization model

Building of the mathematical model continues by opening the Excel Solver® dialogue box and entering the address of the objective function, the type of the extreme value (i.e. the minimum value), the location of the decision variables and the constraint formula (see Fig. 4). Due to the nonlinearity of the problem, the GRG Nonlinear Solving Method is the right method here. The next step is to run SOLVE, keeping the other default settings of the add-in intact.

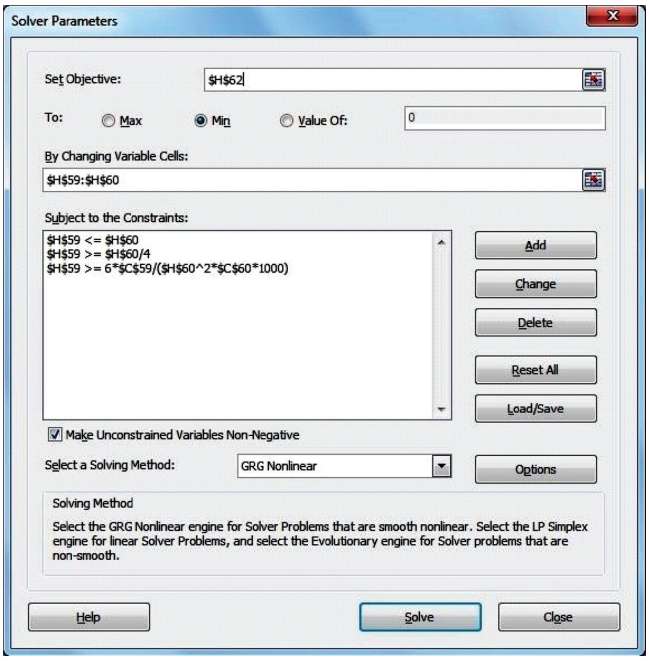

Fig. 4. Dialogue box: Solver Parameters

In this case, the solution time reduces down to a fraction of a second, and Solver® informs the user about the effects of its actions in the next dialogue box (see Fig. 5).

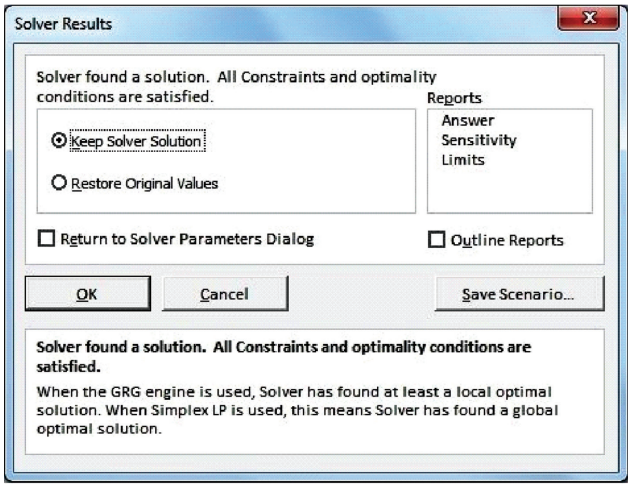

Fig. 5. Dialogue box: Solver Results

The dialogue box shows that Excel Solver® has found an exact solution, which can be stored and seen in the spreadsheet by clicking OK (see Fig. 6).

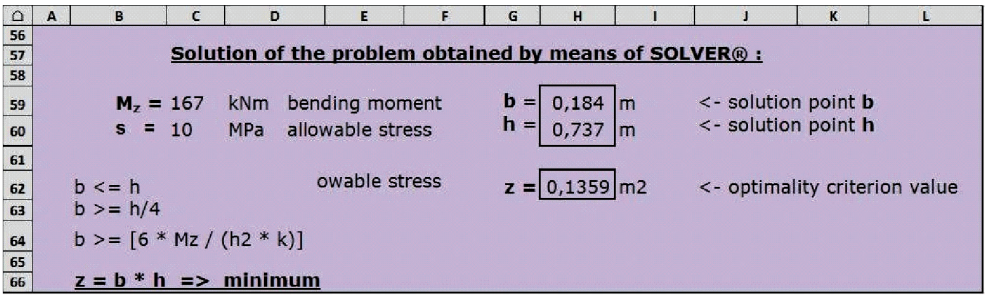

Fig. 6. Fragment of the spreadsheet with the solution to the optimization problem

While still in the Solver Results dialogue box (see Fig. 5), there is the opportunity to additionally produce and save (in a separate worksheet of the current workbook) any of the available reports (e.g. the answer report, the sensitivity report, or the limits report). The sample answer report (see Fig. 7) includes all the elements of the mathematical optimization model and also additional information on which constraints are 'binding' and which are not.

What is most important is that the results of the structural optimization of a simple wooden element, obtained with the use of two completely different methods (with 40 years between them), are exactly the same. Problems which once required designers to

have access to company computers are now successfully solved in the privacy of one's home, in university laboratories or while travelling thanks to the wide availability of desktop PCs and laptops.

Microsoft Excel 14.0 Answer Report
Worksheet: [solver-belki_raporty.xls]Belka drewniana
Report Created: 2014-03-08 17:45:36
Result: Solver found a solution. All Constraints and optimality conditions are satisfied.
Solver Engine
Engine: GRG Nonlinear
Solution Time: 0,016 Seconds.
Iterations: 3 Subproblems: 0
Solver Options
Max Time 100 sec, Iterations 1000, Precision 0,0000001
Convergence 0,000001, Population Size 100, Random Seed 0, Derivatives Forward, Require Bounds
Max Subproblems Unlimited, Max Integer Sols Unlimited, Integer Tolerance 0,001%, Solve Without Integer Constraints, Assume NonNegative

Objective Cell (Min)

Cell	Name	Original Value	Final Value
$H$62	z = from local extremes, which can be several	0,5000	0,1359

Variable Cells

Cell	Name	Original Value	Final Value	Integer
$H$59	b = from local extremes, which can be several	0,500	0,184	Continous
$H$60	h = from local extremes, which can be several	1,000	0,737	Continous

Constraints

Cell	Name	Cell Value	Formula	Status	Slack
$H$59	b = from local extremes, which can be several	0,184	$H$59<=$H$60	Not Binding	0,552972825
$H$59	b = from local extremes, which can be several	0,184	$H$59>=$H$60/4	Binding	0,000
$H$59	b = from local extremes, which can be several	0,184	$H$59>=6*$C$59/($H$60^2*$C$60*1000)	Binding	0,000

Fig. 7. Sample Answer Report to the optimization problem

4. Conclusions

The Excel Solver® optimization add-in, developed and constantly streamlined by Frontline Systems®, is a universal and user-friendly tool to solve various problems, including civil engineering optimization problems. It must be remembered that optimization problems may be both simple and 'cheap' and complex and 'expensive' to solve. This is due to the mathematical relationships within the optimization model itself (linear and non-linear/ convex and non-convex problems) which determine the difficulty of obtaining a solution and the level of certainty as to whether the solution is a real conditional extreme value or merely a value somewhere near the extreme. Additionally, these relationships have a substantial impact on the size of mathematical models, and thus, on the possibility of solving the problems which such models describe. Some highly advanced optimization tools are able to divide the main problem into sub-problems (linear, smooth non-linear, and non-smooth) and then to match each subproblem to the most appropriate solving method. What we, the users of tool software (both engineers and managers), care most about [2] is that the mathematical relationships in models are as simple as possible.

References

[1] Baker K.R., *Optimization Modeling with Spreadsheets*, 2nd ed., Wiley, 2011.

[2] Boroń J., *Optimizers in Solving Managerial and Structural Problems*, [in:] *Information Systems Architecture and Technology: Model Based Decisions*, eds. J. Świątek et al., Oficyna Wydawnicza Politechniki Wrocławskiej, Wrocław 2008, 15–25.

[3] Brandt A.M., *Podstawy optymalizacji elementów konstrukcji budowlanych* (*Basics of Optimization the Components of Building Structures, in Polish*), Państwowe Wydawnictwo Naukowe, Warszawa 1978.

[4] Frontline Solvers, http://www.solver.com/.

[5] Leśniak Z.K., *Metody optymalizacji konstrukcji, przy zastosowaniu maszyn matematycznych* (*Methods for Structural Optimization Using Mathematical Machines, in Polish*), Arkady, Warszawa 1970.

[6] Powell S.G., Baker K.R., *Management Science: The Art of Modeling with Spreadsheets*, 4th ed., Wiley, 2013.

[7] Vanderbei R.J., *Linear Programming: Foundations and Extensions*, 3rd ed., International Series in Operations Research & Management Science, 2008, Vol. 114, Springer Verlag.

[8] Winston W.L., Venkataramanan M., *Introduction to Mathematical Programming: Applications and Algorithms*, Vol. 1, 4th ed., Thomson Learning, 2002.

TECHNICAL TRANSACTIONS | CZASOPISMO TECHNICZNE
CIVIL ENGINEERING | BUDOWNICTWO
6-B/2014

GRZEGORZ BOSAK*

WIND TUNNEL TESTS OF THE EFFECTS OF AERODYNAMIC INTERFERENCE ON A STADIUM ROOF

BADANIA MODELOWE WPŁYWÓW INTERFERENCJI AERODYNAMICZNEJ NA ZADASZENIE STADIONU

A b s t r a c t

This paper summarizes results of wind tunnel tests of a non-standard stadium roof. Aerodynamic laboratory studies were accomplished in a boundary layer wind tunnel. The main objective of the research was to determine the distribution of the mean wind net pressure coefficient over the stadium roof surfaces as affected by the aerodynamic interference between the stadium structure and a large oval sports event hall, located nearby. Interference coefficients of wind pressure and global wind forces acting upon the surfaces of the stadium roof were calculated. The aerodynamic studies showed a significant influence of the oval Atlas Arena sports-event hall on the wind load subjected to the stadium structure.

Keywords: *wind tunnel tests*, *aerodynamic interference*, *wind action on a stadium roof*

S t r e s z c z e n i e

W artykule przedstawiono rezultaty badań modelowych w tunelu aerodynamicznym niestandardowego zadaszenia stadionu. Badania zostały wykonane w tunelu aerodynamicznym z warstwą przyścienną. Podstawowym celem analiz było określenie rozkładu wartości współczynnika średniego ciśnienia wiatru na powierzchniach zadaszenia w warunkach występowania interferencji aerodynamicznej pomiędzy konstrukcją stadionu a rozległą owalną halą widowiskowo-sportową położoną w bliskim sąsiedztwie. Wyznaczono współczynniki interferencji odnoszące się do ciśnienia wiatru na powierzchni zadaszenia oraz do sumarycznych sił działania wiatru na konstrukcję dachu stadionu. Badania wykazały znaczący wpływ hali widowiskowo-sportowej Atlas Areny na działanie wiatru na konstrukcję stadionu.

Słowa kluczowe: *badania modelowe w tunelu aerodynamicznym*, *interferencja aerodynamiczna*, *działanie wiatru na zadaszenie stadionu*

* Ph.D. Grzegorz Bosak, Department of Structural Mechanics, Faculty of Civil Engineering, Cracow University of Technology, Cracow, Poland.

1. Introduction

The subject of the article is to evaluate the influence of aerodynamic interference on the wind action on a stadium roof. There were three circumstances which gave reasons for an aerodynamic modelling of the stadium roof structure in a wind tunnel. Firstly, the stadium roof was open to the north-west (see Fig. 1a)). What is more, in the geographical region of concern, this coincides with the direction of the most frequent strong winds. Secondly, a large oval sports event hall was located nearby (see Fig. 1b)). This could result in a significant aerodynamic interference affecting the stadium roof. Finally, the shape of the roof membrane was similar to a funnel (see Fig. 1c)), which could cause complex and various wind pressure distributions on the roof surfaces and as a result, difficulties in predicting wind action on the main bearing steel frames (see Fig. 1d)) during the design stage.

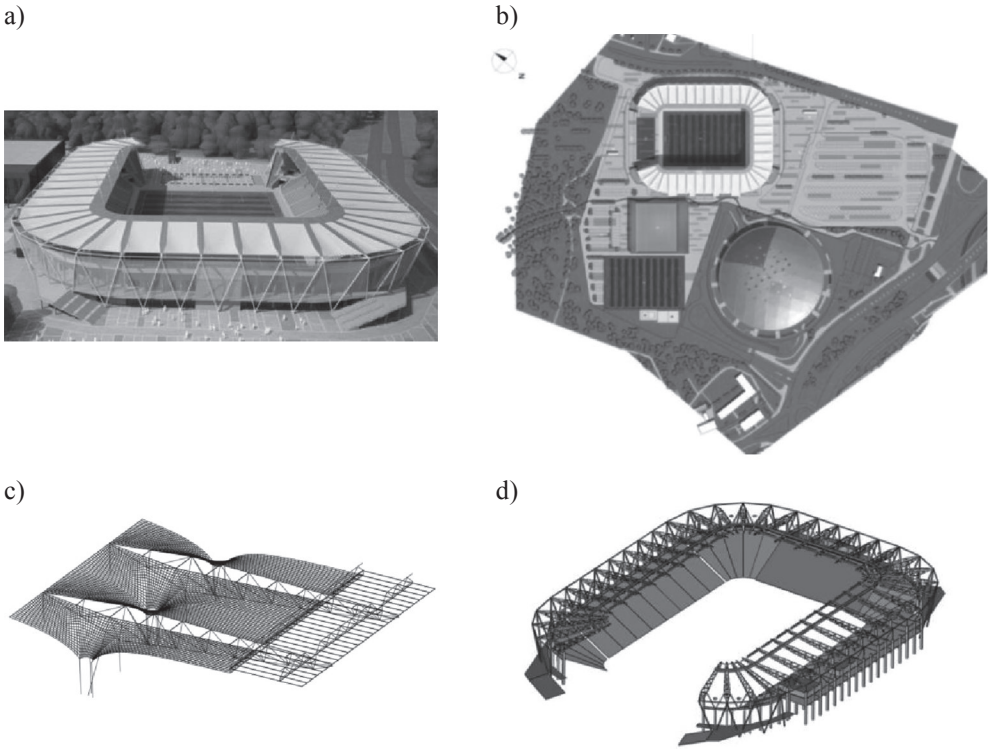

Fig. 1. Computer visualization: a) of the stadium structure, b) of the stadium with the immediate surroundings, c) of the shape of the stadium roof membrane; d) of the main bearing system of the stadium roof

The roof surface consists of a funnel shaped region and a flat inner ring (see Fig. 1c)). The structure is not symmetrical from an aerodynamic point of view. The stadium stands and stadium building objects have different configurations in particular parts of the structure (see Fig. 1d) and Fig. 2).

As can be seen in Fig. 1a), the whole roof surface is divided into 39 segments. Each segment is placed between the main steel frames and has a complex geometrical shape (see Fig. 1c)). In addition, the stadium façade is made of claddings which are permeable to air.

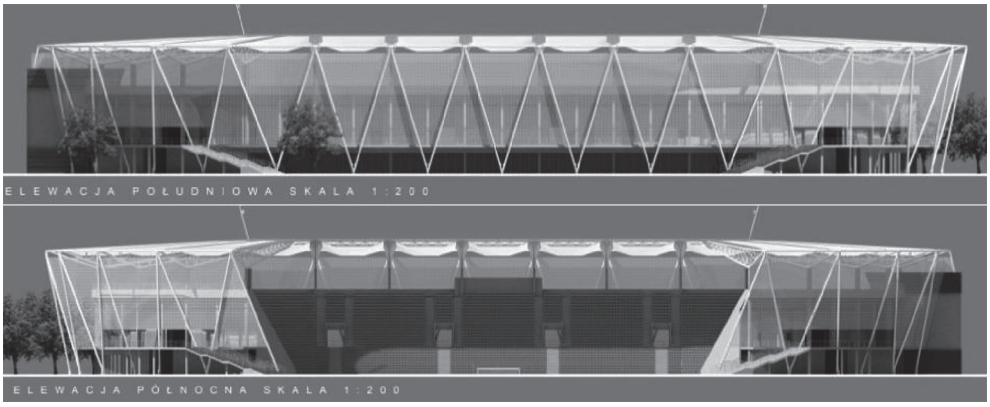

Fig. 2. Computer visualization of the stadium facades

All the above mentioned reasons motivated an aerodynamic wind tunnel investigation of a model.

2. Characteristics of the wind tunnel tests

The wind tunnel tests were conducted, using 1:200 scale stadium model, in the wind tunnel of the Wind Engineering Laboratory of Cracow University of Technology. The stadium and its immediately surrounding area within a radius of 250 m was modelled. This mainly consists of two structures: the stadium structure and the oval sports-event hall. Additionally, a training hall located near the stadium was taken into consideration. During the wind tunnel tests of the aerodynamic interference, the stadium and the training hall were studied as one object (see Fig. 3a)).

a) b)

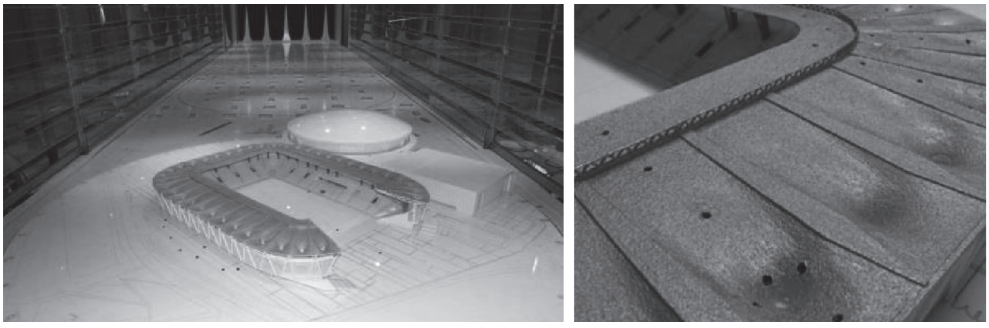

Fig. 3. a) stadium model with its immediate surroundings in the wind tunnel working section, b) a part of the stadium roof model with pressure taps

The stadium model, at a scale of 1:200, and the other model objects of the immediate surroundings were placed on a 200 cm diameter turn-table, which allowed for the simulation of any wind direction in the working section. The measurements were taken for 36 wind directions with steps of 10° each. The model was instrumented with 224 pressure taps (see Fig. 3b)). The mean wind pressure and the standard deviation of wind pressure fluctuations were measured at each tap. On the basis of the measured data, mean pressure coefficients were calculated. A view of the tested model in the wind tunnel working section is presented in Fig. 3a).

The experiments were performed for the following conditions: power law exponent of mean wind velocity profile α = 0.3; area-averaged turbulence intensity on the level of the stadium roof I_v = 20%; reference velocity on the height level of the stadium roof model V_{ref} = 13.5 m/s. All of the wind tunnel properties such as the configuration of an adjustable ceiling, ejection of floor blocks, RPM of the fan, type of circulation, settings of barrier and spires had been optimised due to the model size, its scale, external shape, and roughness of the terrain. The mean wind velocity profile obtained in the wind tunnel working section during the experiments is presented in Fig. 4.

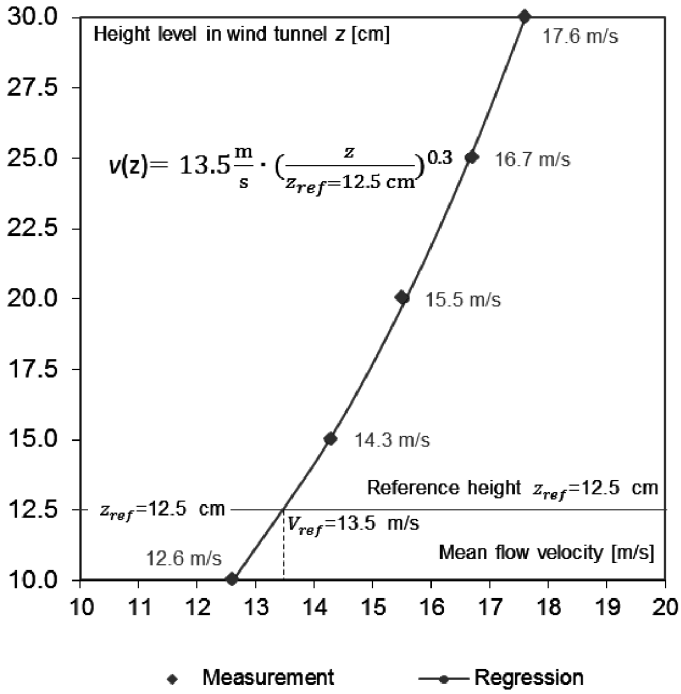

Fig. 4. Mean wind velocity profile obtained in the wind tunnel working section

A profile pressure probe, a pressure electronic scanner, which allow measuring differential pressure (a difference between the wind pressure on the top surface and the wind pressure on the bottom surface of the stadium roof membrane) in 64 taps simultaneously, and a hot–wire anemometer system were used during the experiments. The tunnel investigations were based on methodology presented in [1].

Below, in Fig. 5, a flow chart of the measuring system of differential wind pressure on the roof surfaces is presented.

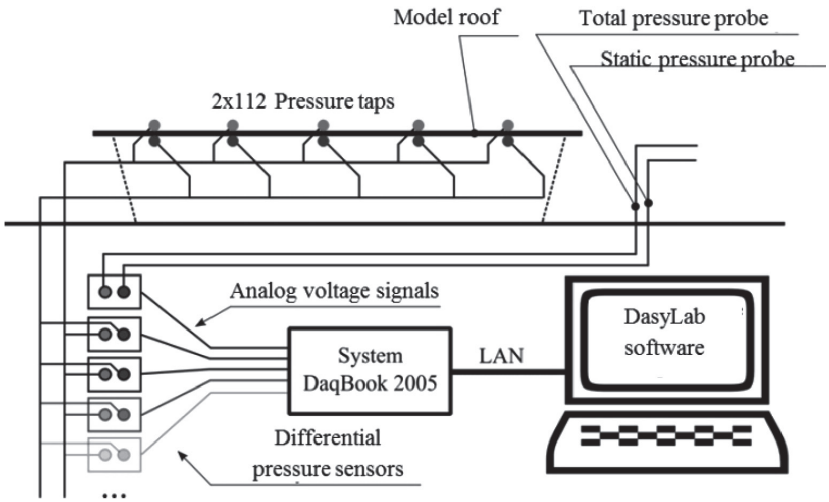

Fig. 5. The flow chart of the measuring system of differential wind pressure on the roof surface

Two measuring configurations, a non-interference configuration and an interference configuration, were considered during the experiments (see Fig. 6). In the first configuration, the measurements were conducted without any influence from the stadium neighbourhood. Subsequently, in the second configuration, the existence of the surrounding sports-event hall was taken into consideration during the tunnel test. Additionally, wind directions analysed during the experiments are presented in Fig. 6.

a) b)

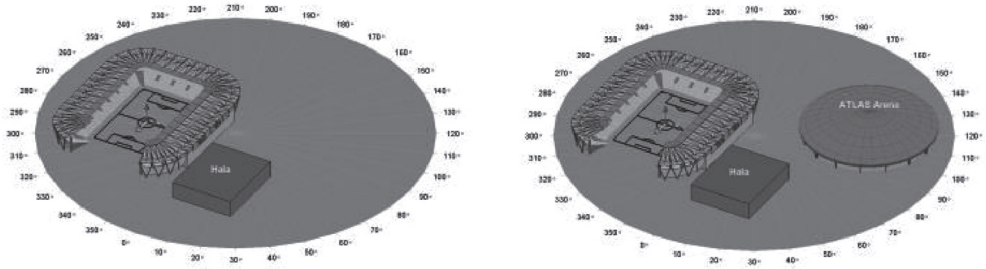

Fig. 6. Measuring configurations: a) a non-interference configuration, b) an interference configuration

The comparison of the results, namely the values of the wind pressure coefficients and the components of the global wind forces acting on each of the 39 roof segments, was accomplished on the basis of the test results for the two analysed configurations.

3. Results of the wind tunnel tests

The results of the values of the $C_{p,net}$ coefficient were determined in the non-interference and the interference configurations according to the formula (1):

$$C_{p,net}\left(x,y,z,dir\right)=\frac{\overline{p}_{net}\left(x,y,z,dir\right)}{q_{ref}\left(z_{ref}\right)} \tag{1}$$

The reference level z_{ref} was at a height of the top level of the stadium model roof (equivalent to 25 m above ground in full scale). Negative values of wind pressure lift the roof membrane up. Below, in Fig. 7, exemplary distributions of $C_{p,net}$ coefficient in the interference configuration for the chosen wind directions are presented.

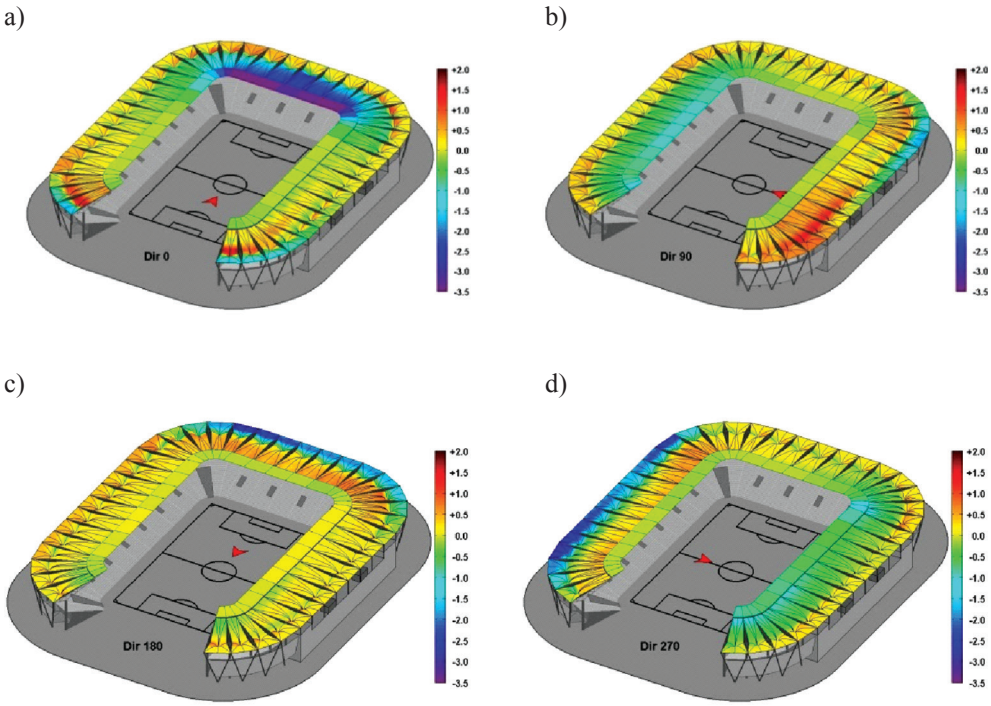

Fig. 7. Distributions of $C_{p,net}$ coefficient in the interference configuration for the chosen wind directions (a red arrow indicates the wind direction)

The values of the wind differential pressure coefficients are between +2.0 (positive pressure) and –3.5 (negative pressure). It is observed that the open geometry of the stadium roof caused an unfavourable aerodynamic effect, which consists of the occurrence of a huge uplift wind load for the fragment of the roof located in the opposite side to the open region of the stadium. This effect is strongly observed for the wind directions described by the angle values near 0°. In this roof region, the wind differential pressure coefficient reached the value

of –3.5 (see Fig. 7a)). The funnel shape of the stadium roof membrane caused significant variation of wind pressure distribution on the analysed surfaces. The positive differential wind pressure was applied over the leeward membrane area placed behind the funnel, which pressed this roof region down. This was as a result of the funnel wake existence at the below side of the stadium membrane. The windward region was lifted where the considerable negative net wind pressure occurred. This is observed very clearly in Fig. 7d).

In full scale, the global aerodynamic forces for the inner ring and the funnel area of the stadium roof were separately calculated by using distributions of the $C_{p,net}$ coefficient obtained from the measurements according to the formula (2):

$$F_k(dir, seg, area) = \\ = q_{ref}^{p}\left(z_{ref}\right) \sum_{A_{seg,area}} C_{p,net}\left(x, y, z, dir\right) \cdot \Delta A_{seg,area}\left(x, y, z\right) \cdot n_k\left(x, y, z\right) \tag{2}$$

where:

- dir – wind direction,
- k – coordinates x, y, z,
- seg – the segment region (total number of segments was equal to 39),
- $area$ – the inner ring area or the funnel area,
- ΔA – a part of the area of the roof surface,
- n_k – a coordinate of the unit vector, perpendicular to the roof surface.

Coordinate systems of the global aerodynamic forces for the inner ring and the funnel area of the stadium roof are presented in Fig. 8.

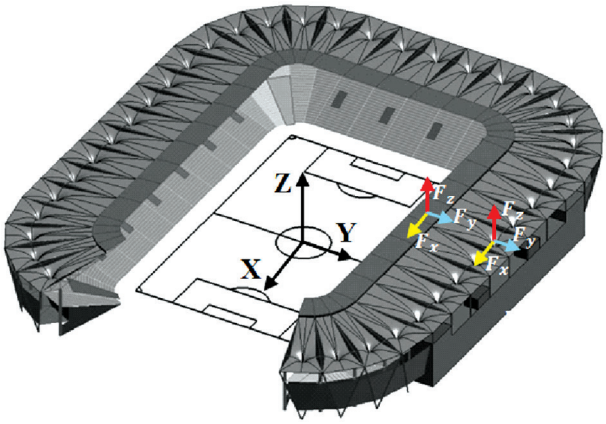

Fig. 8. Coordinate systems of the global aerodynamic forces for the inner ring and the funnel area of the stadium roof

The chosen distributions of the global aerodynamic forces for the inner ring and the funnel area, in relation to the force envelopes in the interference configuration, are presented in Fig. 9.

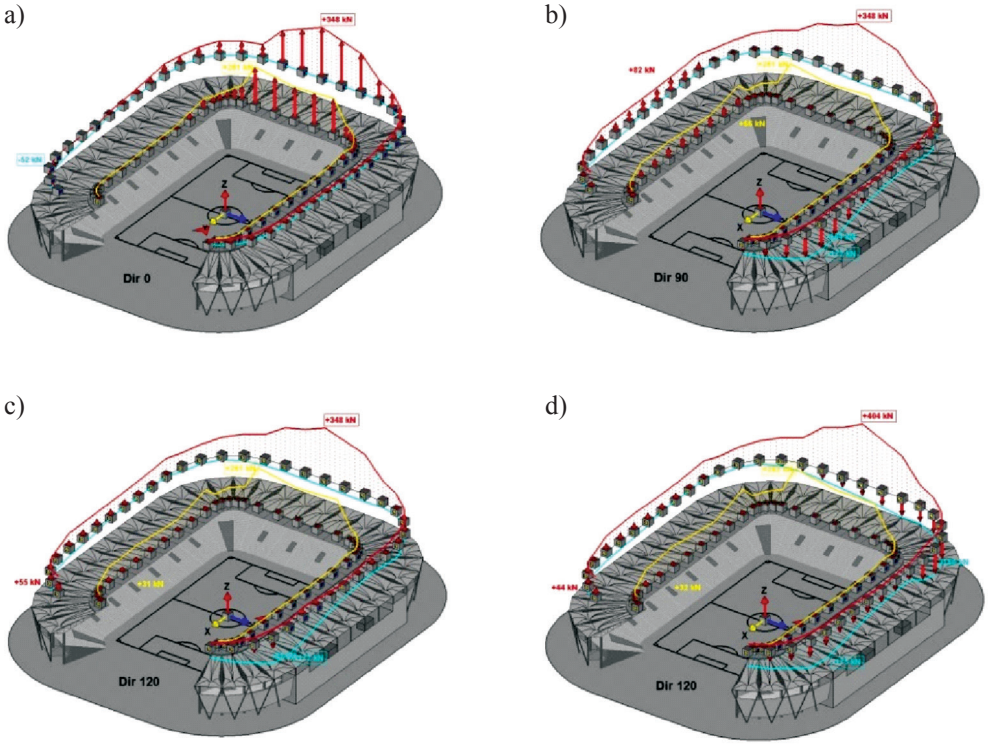

Fig. 9. Distributions of the global aerodynamic forces for the inner ring and the funnel area in relation to the force envelopes in the interference configuration

In Figs. 10 and 11, the envelopes of the global aerodynamic forces for the funnel area and the inner ring in the non-interference and interference configurations are presented. Wind directions, referring to the values of the wind force envelopes for any of 39 segments of the stadium roof, were introduced in the figures presented below.

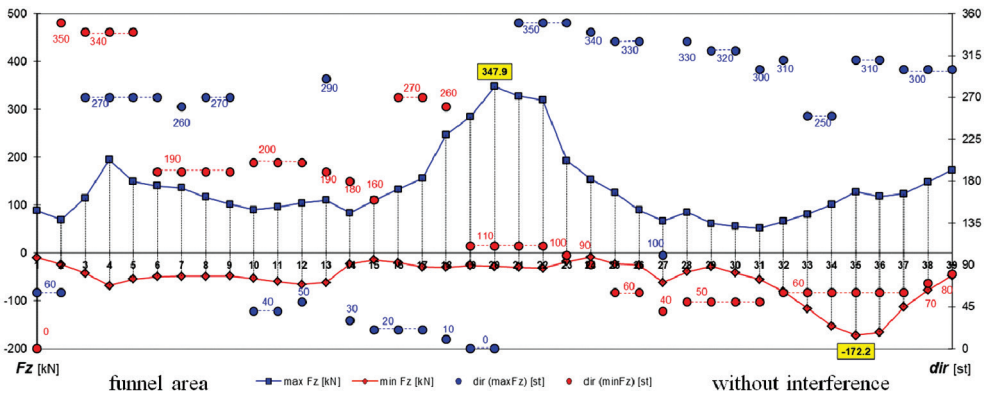

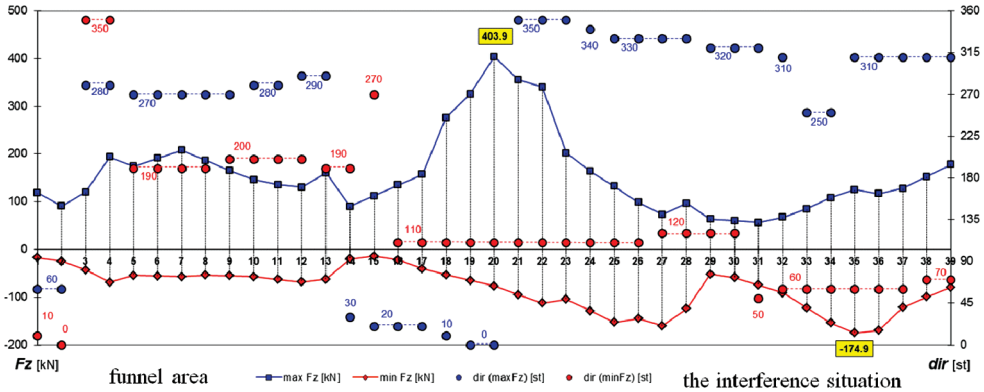

Fig. 10. Envelopes of the global aerodynamic forces for the funnel area in the non-interference and interference configurations

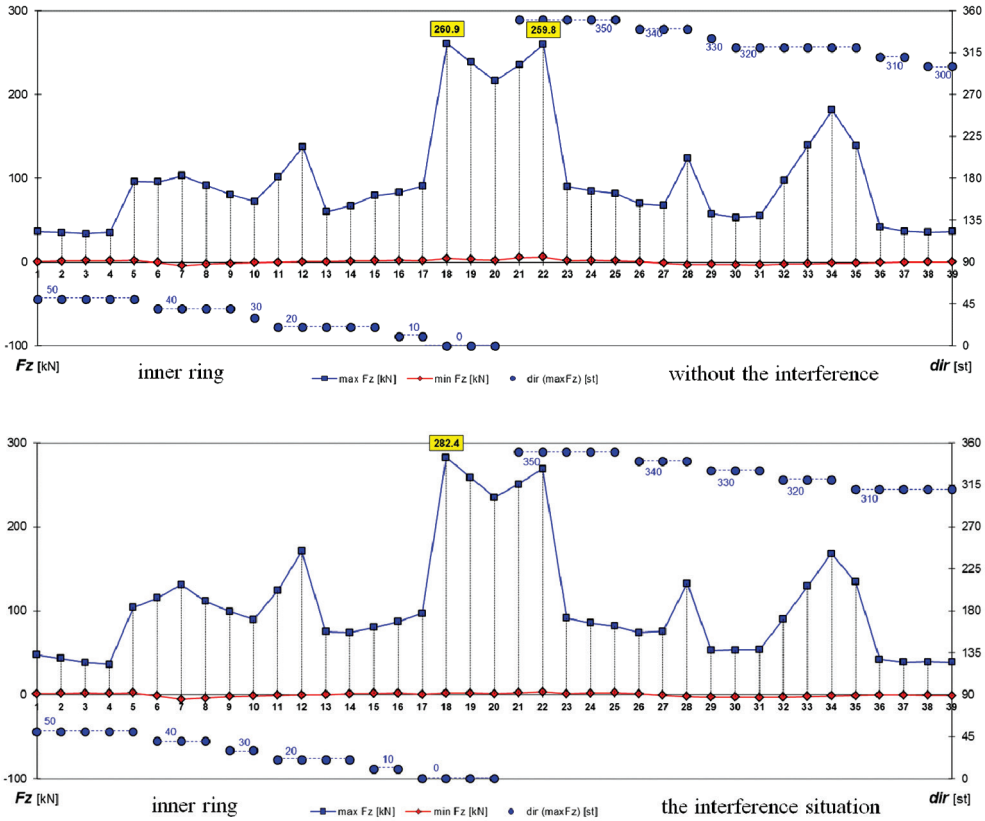

Fig. 11. Envelopes of the global aerodynamic forces for the inner ring in the non-interference and interference configurations

A importance of the aerodynamic interference for the changing of the wind pressure on the roof surface was determined by the interference coefficient I_c^p [2] obtained according to formula (3):

$$I_c^p\left(x,y,z,dir,type,area\right)=\frac{\left|\left[C_{p,net}^{I}\left(x,y,z,dir\right)-C_{p,net}^{S}\left(x,y,z,dir\right)\right]_{type}\right|}{\max\left|C_{p,net}^{S}\left(x,y,z,dir\right)\right|_{area}} \tag{3}$$

where:

dir – wind direction,
x, *y*, *z* – point coordinates,
I – interference configuration,
S – non-interference configuration,
type – the type of wind pressure variation on the roof surfaces according to Tab. 1,
area – the inner ring area or the funnel area.

Table 1

Types of wind pressure coefficients changing on the roof surface

Type	Change type	Colour mark	$C_p^I(x,y,z,dir)$	$C_p^I(x,y,z,dir)$	$C_p^I(x,y,z,dir)-C_p^S(x,y,z,dir)$
6	*pos* ↑		$C_p^I>0$	$C_p^S\geq 0$	$C_p^I-C_p^S>0$
5	*pos* ↓		$C_p^I\geq 0$	$C_p^S\geq 0$	$C_p^I-C_p^S\leq 0$
4	*neg* ↑ *pos*		$C_p^I\geq 0$	$C_p^S<0$	$C_p^I-C_p^S>0$
3	*pos* ↓ *neg*		$C_p^I\leq 0$	$C_p^S>0$	$C_p^I-C_p^S<0$
2	*neg* ↑		$C_p^I\leq 0$	$C_p^S<0$	$C_p^I-C_p^S\geq 0$
1	*neg* ↓		$C_p^I<0$	$C_p^S\leq 0$	$C_p^I-C_p^S<0$

The most significant influence of the aerodynamic interference between the stadium and the oval sports-event hall was observed for the wind direction of 120°. This situation is presented in Fig. 12, where the stadium structure was sheltered by the oval sports event hall (to be located on the leeward side of the oval sports-event hall – see Fig. 6b)).

The maximum values of the pressure interference coefficient with division into six types of wind pressure change are presented in Tab. 2. According to the wind tunnel tests, the largest influence of the aerodynamic interference, connected with the existence of the neighbouring sports event hall, was observed for a limited area of stadium roof situated near the neighbouring structure. Mostly, the effect of aerodynamic interference consisted of pressing the roof membrane down (see the area of wind pressure change of types 2, 4, 6 in Fig. 12). No noticeable influence was observed for the inner ring area of the roof.

To compare the global vertical aerodynamic force component acting on each of 39 roof segments, an interference coefficient $I_c^{F_z}$ was calculated using the formula (4):

Table 2

Maximum values of I_c^p

Type	Funnel area	Inner ring area
6	0.92	0.03
5	0.23	0.01
4	0.98	0.03
3	0.30	0.01
2	0.93	0.26
1	0.51	0.31

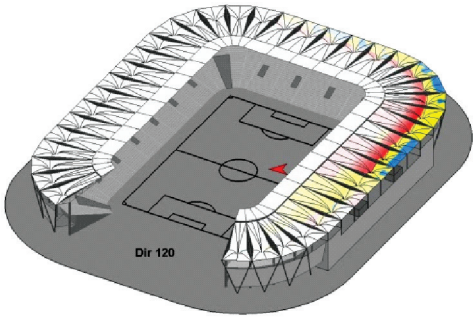

Fig. 12. Distribution of I_c^p coefficient for 120° wind direction in the interference configuration

$$I_c^{F_z}\left(dir, area\right) = \frac{\left|F_z^I\left(dir, area\right)\right| - \left|F_z^S\left(dir, area\right)\right|}{\max\left|F_z^S\left(dir\right)\right|_{area}} \cdot 100\% \tag{4}$$

where:

- F_z – vertical component of the aerodynamic force acting on the particular segment of the inner area or the funnel area,
- *dir* – wind direction,
- *I* – interference configuration,
- *S* – non-interference configuration,
- *area* – the inner ring area, the funnel area.

The distributions of I_c^F coefficient values are presented in Fig. 13. The largest influence of the aerodynamic interference was observed for the funnel area of 27th segment (see Tab. 3). In this case, the wind direction angle was equal to 120°. The stadium roof regions of the significant aerodynamic interference effects were placed over the funnel area located near the sports event hall. The interference influence from the neighbouring structure consisted largely in pressing the stadium roof down in cases where the roof funnel area of the stadium was placed into the aerodynamic wake of the sports-event hall.

Table 3

Extreme values of I_c^F coefficient

Area	Funnel region		Inner ring region	
Extreme	Max	Min	Max	Min
Value of I_c^F [%]	+190%	–56%	+31%	–26%
Segment	27	29	7	31
Wind direction	120°	90°	30°	290°

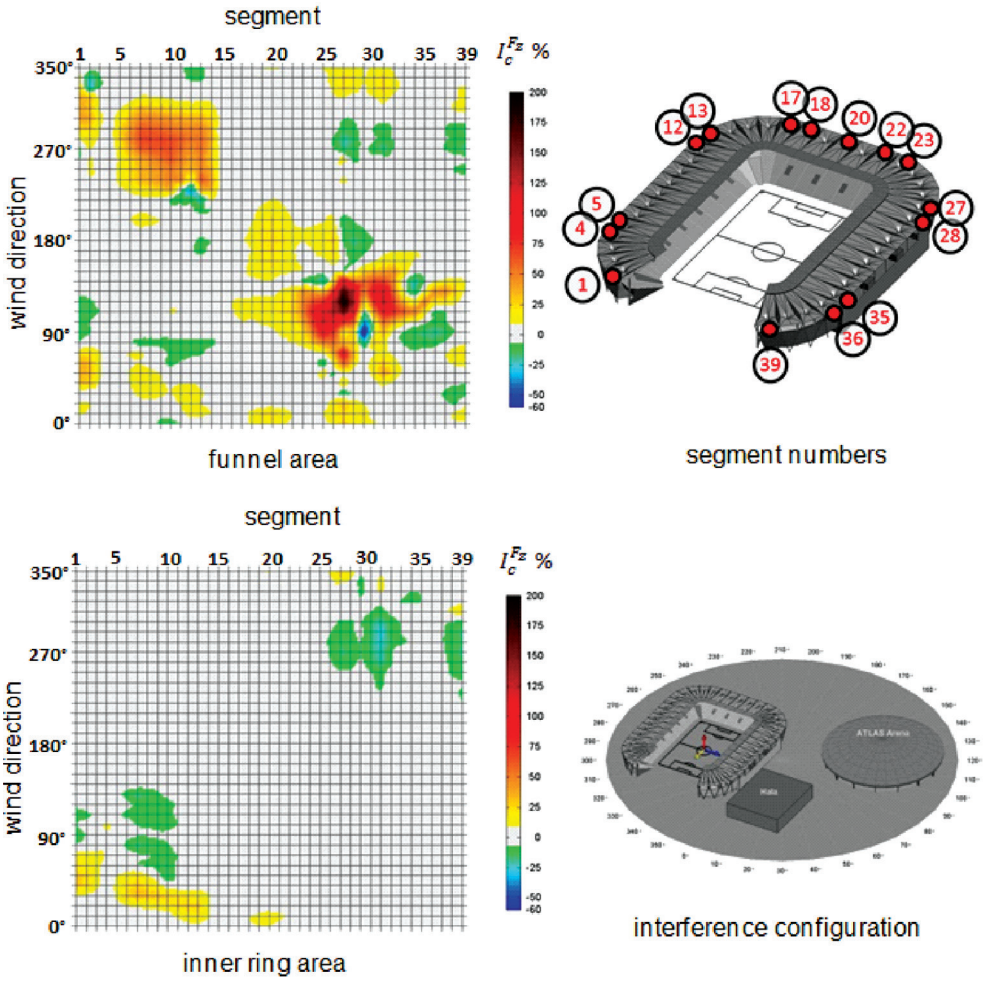

Fig. 13. Distributions of I_c^F coefficient in the interference configuration

4. Conclusions

The results of the measurements which were carried out in the wind tunnel allow for the formulation of the following conclusions:

– The open geometry of the stadium roof caused unfavourable aerodynamic effects. A significant uplift wind load for the part of the roof located on the opposite side to the open region of the stadium was observed for wind directions described by the near angles equaled to 0°.
– The funnel shape of the stadium roof membrane caused significant variation of wind pressure distribution on the analysed surfaces. The leeward membrane area behind the roof funnel was exposed to a positive net wind pressure which pressed this roof region down. This

was a result of the appearance of the funnel wake at the bottom of the stadium membrane. The windward region was lifted where the significant negative net wind pressure occurred.

– The wind tunnel tests showed the significant influence of aerodynamic interference as a result of the proximity of the training hall and the sports-event hall with the stadium structure but the effect was limited to the confined stadium roof area situated near the neighbouring structure. The effect of aerodynamic interference consisted largely of pressing the roof membrane down in part of the funnel area, whereas for the inner ring area, this kind of wind load change is not observed.
– The measurements of the wind velocity absolute value, accomplished over the playing field of the stadium, showed an existence of an air flow ram effect. The nature of the effect, similar to the Venturi tube phenomenon, significantly increased the enormous lifting wind load on the part of the stadium roof located on the opposite side to the open region.

References

[1] Jóźwiak R., Kasprzyk J., Żurański J.A., *Wind tunnel tests of a cable supported roof of a stadium*, Proc. of 10th ICWE, Copenhagen 1999, 1511–1517.
[2] Bosak G., *Wind tunnel tests of aerodynamic interference of double-shell tanks*, Czasopismo Techniczne, 3B/2012, 3–19.
[3] Borri C., Biagini P., *Structural response of large stadium roofs due to dynamic wind actions*, Stahlbau 74, Heft 3, 2005, 197–206.
[4] Zhu L.D., Chen W., Shi Z.C., Zhang F., *Wind pressure distribution on a stadium roof by wind tunnel model test*, Proc. of 10th ICWE, Copenhagen 1999, 1583–1590.

TECHNICAL TRANSACTIONS | CZASOPISMO TECHNICZNE
CIVIL ENGINEERING | BUDOWNICTWO
6-B/2014

PIOTR GWOŹDZIEWICZ, MARCIN MIDRO*

DURABILITY EVALUATION OF BRIDGE STRUCTURE: COMPARISON BETWEEN ANALITICAL APPROACH AND EXPERIMENTAL INVESTIGATIONS

OSZACOWANIE TRWAŁOŚCI KONSTRUKCJI MOSTU: PORÓWNANIE PODEJŚCIA ANALITYCZNEGO Z BADANIAMI NA OBIEKCIE

A b s t r a c t

The paper is focused on the problem of durability of RC structure exposed to typical ambient conditions for bridges. The causes and degradation processes of the structures, mechanisms of concrete carbonation and chloride penetration are described. The theoretical model which allows for the prognosis of all changes affecting construction safety in time is presented. The findings of the theoretical analysis are compared with the results of the experimental research of a viaduct in a state of an advanced degradation as well as the material samples taken from it.

Keywords: *carbonation*, *corrosion*, *maintenance*, *service life*

S t r e s z c z e n i e

Niniejszy artykuł poświęcony jest zagadnieniu trwałości konstrukcji. Opisano w nim przyczyny i procesy degradacji obiektu, mechanizmy karbonatyzacji betonu i penetracji chlorkowej. Przedstawiono model teoretyczny pozwalający prognozować przebieg zmian bezpieczeństwa konstrukcji w czasie. Wyniki analizy teoretycznej porównano z rezultatami badań doświadczalnych obiektu mostowego w zaawansowanym stadium degradacji i pobranego materiału.

Słowa kluczowe: *karbonatyzacja*, *korozja*, *konserwacja*, *czas użytkowania konstrukcji*

* Ph.D. Eng. Piotr Gwoździewicz, M.Sc. Eng. Marcin Midro, Cracow University of Technology, Faculty of Civil Engineering, Cracow, Poland.

1. Introduction

Knowledge of materials degradation mechanisms and their influence on structural properties enables predictions regarding the duration of a given RC member's service period. Several processes lead to shortening of the structural durability assumed in design by provoking degradation of concrete and corrosion of reinforcement. In any environment, one should account for the presence and diffusion of carbon dioxide, causing concrete carbonation and further corrosion of non-protected steel. Some structures are placed in aggressive atmospheres provoking an accelerated degradation and corrosion process, as for instance in chemical production plants or bridges subjected to winter de-icing treatment. The issue of the cyclic freezing-thawing effect is not addressed in this paper.

An awareness of the importance of the design and construction decisions on durability is continuously increasing among engineers. Many structures built in the past, today show damages resulting from corrosion. Today, standard provisions require fulfilling several requirements and recommendations referring to cross-section layout and the selection of materials which should result in improving the durability of a given member. Additionally, the need to predict the optimal time of repairs of existing structures remains important. Models for the evaluation of the theoretical degradation process of concrete members are helpful for such purposes. The aim of this work is to present the application of such a model to the evaluation of a structure exposed to environmental and chloride actions.

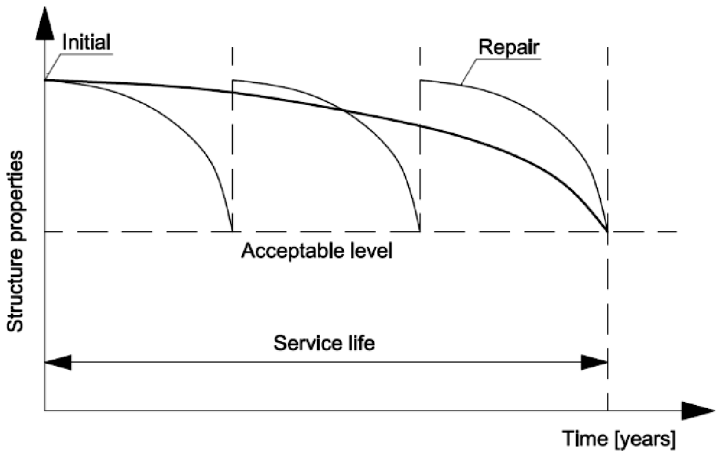

Fig. 1. Decrease of structure properties on service life

2. Theoretical model of degradation

The degradation process in concrete structures is generally divided into two main phases:

- incubation – when concrete passivates the embedded reinforcement and its deterioration is yet to start but the carbonation progress is continuously penetrating the cross-section,
- propagation – when reinforcement corrosion has started and the decreasing diameters of the reinforcing bars provokes a simultaneous decrease in the load-bearing capacity.

The presence of chloride ions in concrete during either phase, propagation or incubation, provokes pitting corrosion which is several times faster than the standard uniform corrosion of depassivated steel. The composition of the model presented below follows this two-fold approach.

2.1. Period of incubation

The goal of calculation for this period is limited to the evaluation of the time needed for carbonation of the whole cover thickness. The incubation time t_i is obtained from the expression:

$$t_i = \left(\frac{c}{K}\right)^2 \text{ [in years]} \tag{1}$$

where (details in [5]):

c – thickness of the concrete cover layer [mm],

K – carbonation rate factor depending on the set of parameters: the relative ambient humidity, the concrete compressive strength and the environment conditions, factor in [mm/years$^{0.5}$]:

$$K = \gamma \cdot k \cdot f_{(HR)} \tag{2}$$

where:

$f_{(HR)}$ – coefficient related to the relative ambient humidity HR:

$$f_{(HR)} = -3.5833 \cdot HR^2 + 3.4833 \cdot HR + 0.2 \tag{3}$$

k – transport coefficient, depending on concrete compressive strength:

$$k = \sqrt{365} \cdot \left(\frac{1}{2.1\sqrt{f_{ck}}} - 0.06\right) \tag{4}$$

γ – exposition coefficient established on the base of experiments [5] depending on the environment conditions at a value equal to one from the following: 1.5, 1.2, 0.9.

In concrete exposed to chloride action, the concentration of chlorides at a given depth from surface depending on time may be evaluated from the formula involving the Gauss error function $erf(\ldots)$:

$$C_x(t) = C_0\left[1 - erf\,\frac{x}{2\cdot(D\cdot t)^{1/2}}\right] \tag{5}$$

where:

$C_0(t)$ – chloride concentration in the surface layer of concrete at time t,
C_x – chloride concentration at distance x from the surface layer of concrete,
D – diffusion coefficient assumed for the overall chloride concentration in concrete,
x – depth from the surface penetrated by chlorides.

2.2. Period of propagation

In the propagation period, corrosion of the steel bars progresses. An important structural safety consequence of this reduction is the reduction of the bar diameter. The expression discussed in [11] has the following form derived from Faraday's law; this gives the thickness of corroded steel over the course of time

$$\delta(t) = \alpha \cdot \lambda \cdot i_{cor} \cdot (t - t_i) \tag{6}$$

where:

$\lambda = \dfrac{M}{\rho n F}$ – uniform penetration rate per current unit density, $\lambda = 0.01163$ for Fe; for iron: $M = 55.85$ g/mole (molar mass), $\rho = 7.85$ g/cm^3 (density), $n = 2$ (valency for Fe^{2+}), $F = 96{,}485$ C/mole (Faraday's constant),
α – acceleration coefficient, equal to (1) for uniform corrosion, equal to (4) to (5) in the case of pitting corrosion provoked by chlorides,
t, t_i – time, incubation time, years,
i_{cor} – corrosion current density [μA/cm^2]:
$i_{cor,\max} = 1.0$ μA/cm^2 (aggressive atmosphere),
$i_{cor,\mathrm{med}} = 0.5$ μA/cm^2 (medium aggressive atmosphere),
$i_{cor,\min} = 0.2$ μA/cm^2 (low aggressive atmosphere).

3. Presentation of the investigated structure

The above described expressions for the depth of carbonation, chloride ion concentration, and for evaluation of the propagation periods will be adopted for the assessment of material degradations and structural serviceability life. This analysis is focused on a viaduct located in the south of Poland. The structure, which was built in the late 70ies, is a 22-span bridge over a river, its total length equals 408.30 m (Fig. 2). The bridge deck is composed of six prestressed concrete precast I-girders connected by a concrete slab which was cast in situ (see Figs. 3 to 5). The superstructure is supported by RC column piers crowned with reinforced concrete beams.

The prestressed concrete precast girders each have a cross-section area of $A_{cp} = 0.32$ m^2, and a cross-section depth of $h = 0.9$ m. Their standard lengths reach 16.0 m and 18.0 m, but their real lengths are larger – the distance between the support axes is between 16.72 m and 16.89 m for the "16.0 m" girders and 18.59 m to 18.93 m for the "18.0 m" girders. According to the design, the girders were cast of concrete with an average compressive strength equal

to 40 MPa. Pier cross-heads are symmetrical with an overall length of 8.40 m. Their cross--section is rectangular and varies between 600 mm × 700 mm and 1,000 mm × 700 mm (depth × width). Piers and crossheads were cast of concrete with average compressive strength equal to 30 MPa. Reinforcement average yield strength of crossheads was measured at 410 MPa.

Fig. 2. View of viaduct before repair

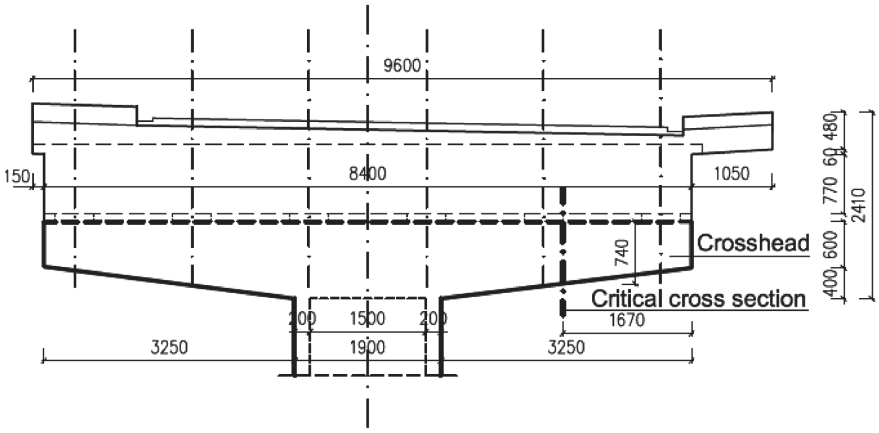

Fig. 3. Geometry of the crosshead on a RC pier

The bridge is built in an area of Poland that has the longest winter climatic conditions. Starting from the beginning of its work, the structure was subjected to the action of unfavorable ambient conditions, such as: air temperature variations (yearly and daily cycles including freezing), variable humidity as well as the appearance of chloride ions as a result of winter road maintenance (planned de-icing of roads). The main attention is put on both concrete members: girders and crossheads. These were in a location particularly susceptible to chloride corrosion since water from the viaduct surface had been leaking for a prolonged period through expansion joint gaps and out of a non-tight collector (Fig. 6). After preliminary

studies, prestressed concrete girders of the bridge load carrying structure were found to be in good condition. The crossheads are the most damaged parts of this viaduct and they serve as the research subject. The structural safety assessment is related to the bending moment born by a cantilever cross-section. Although from a static point of view, the most critical section may be that which is at the cross-beam connection to the column, the observed corrosion state influenced the selection of another cross-section, located at 1,670 mm from the free end of the cantilever (shown in Fig. 3).

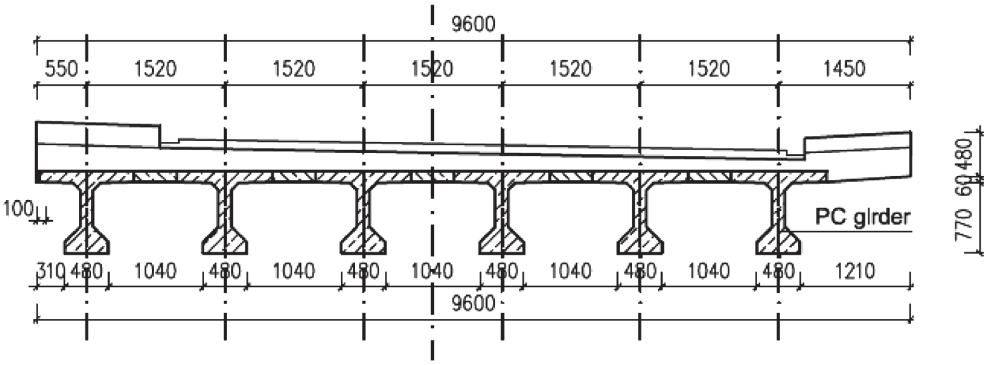

Fig. 4. Cross-section of bridge at one of the spans

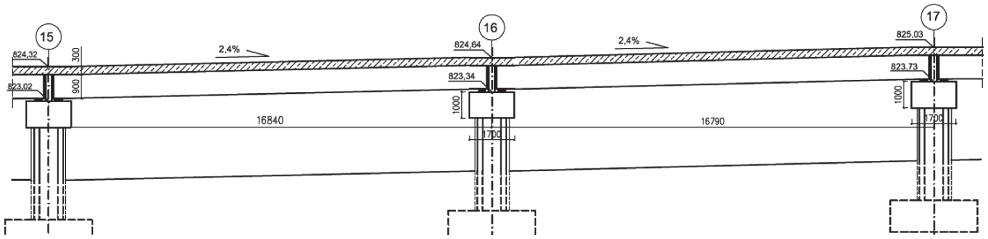

Fig. 5. Part of longitudinal section of the bridge

a) b)

Fig. 6. Bridge before repair: a) view of the investigated crosshead in the axis no. 15, b) non-tight collector above the pier cross-beam of bridge

Following the renovation project provisions which assumed an increasing structure capacity to the highest load class, the present viaduct was subjected to an advanced reconstruction. Pillars and crossheads were cleaned and stiffened by an additional concrete layer (0.2 m). Girders were sandblasted and covered with a protective layer.

4. Chemical analysis of concrete samples collected from structure

Results of laboratory tests on selected specimens collected from the viaduct are presented in this section. The aim is to determine the technical state of the structures, in particular, the advancement of the corrosion process. As already mentioned, concrete samples were taken from locations particularly exposed to corrosion, i.e. from crosshead numbers 15 and 16, including the zone situated directly below the expansion joint. The samples were obtained by crushing pieces of concrete cover or were taken in the form of drillings from 0–50 mm deep holes, separately for every 10 mm. Seven core drilled specimens and drillings at 16 locations were collected. Six drilling locations were located on the less corroded crosshead no. 16 and ten on the more corroded crosshead no. 15 (Fig. 7).

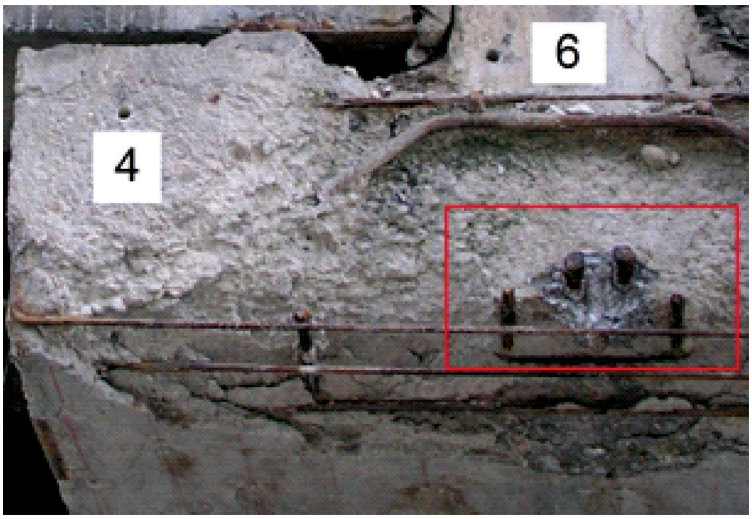

Fig. 7. Drilling locations on the more corroded crosshead no. 15

The samples were subjected to chemical analysis in accordance with test standards given in codes [7–8]. The analysis included the determination of pH for water extract from the specimens and the percentage of chloride ions in the cement gel. For all drillings and core drillings, the results show similar pH factor values for all locations but varied mean quantities of chloride ions. The pH for all the drillings are in the range 9.55–11.73, below the threshold value of 11.80 [2] which represents safe conditions for the reinforcement passive state. The pH factor variation with depth of drilling for both crossheads is similar. Selected results are shown in Tab. 1.

Table 1

Chemical analysis results for the material obtained through the drilling of crossheads (average)

No.	Location of sample	Depth of concrete cover [cm]	pH value	Cl^- [% weight of cement]
1	Crosshead no. 15	0.0–1.0	9.55	1.46
		1.0–2.0	10.40	1.70
		2.0–3.0	11.24	2.06
		3.0–4.0	11.11	1.62
		4.0–5.0	11.49	1.20
2	Crosshead no. 16	0.0–1.0	9.77	0.63
		1.0–2.0	10.24	0.66
		2.0–3.0	11.34	1.30
		3.0–4.0	11.73	1.10
		4.0–5.0	11.63	0.80

The viaduct displayed visibly more advanced corrosion development than other similar structures. Reinforcement corrosion was observed mainly at locations where water from the bridge surface leaked through the expansion joints and collectors – this is where splitting of the concrete cover was also observed. A higher amount of chloride ions was also observed in crosshead no. 15 compared to crosshead no. 16. This proves a popular opinion that the presence of chloride ions Cl^- in concrete provokes highly accelerated reinforcement corrosion progress compared to instances of carbonation alone [10]. Chemical analysis allowed the determination of the percentage of chloride ions in relation to concrete depth and also the determination of the depth of chloride ion penetration. A slightly higher concentration for crosshead no. 15 was observed. The average saturation of chloride ions for all the tested specimens to a depth of 80 mm is above the limit value, which for concrete structures equals 0.4% of the cement weight [2]. Values obtained for the depths of 2.0–3.0 cm reach over 2–5 times more than the limit. This limit value is exceeded three times in surface layers of the concrete cover due to "washout" of chloride ions.

5. Comparison of experimental results with theoretical calculations

The model described in this paper is used to analyze the durability of the structure subjected to progressive degradation, in order to estimate its service life. Firstly, the incubation time t_i, is determined based on concrete carbonation and chloride ingress, taking into consideration the environmental conditions (relative ambient humidity, chloride concentration). Secondly, the propagation period is analyzed based on the corrosion rate derived from Faraday's law, when progressive reinforcement corrosion develops. For viaduct members, corrosion provokes a continuous reduction of load-bearing capacity

in critical sections. Parameters of the corrosion process measured in the laboratory tests are used to build a relationship between the analysis and the observed condition of the structures.

The incubation time is calculated according to Eq. (1). In Table 2, theoretical values of the incubation times in years are presented for the relevant concrete cover thickness for reinforcing bars and for various levels of the relative humidity of the ambient air. Results obtained for the most adequate values of the relative humidity of the ambient air, 50%, 60% and 70%, are shown on greyed rows. For further analysis, the incubation time for reinforcement was assumed at 8 years as a representative value for the usual relative humidity level of the ambient air.

Table 2

Incubation time for the given thickness of concrete cover and various relative humidity levels: crossheads (c = 40 mm)

RH	Incubation time [years] for c = 40 mm
40%	7.26
50%	6.91
60%	7.55
70%	9.70
80%	15.72

Evaluation of the carbonation depth for the 35-years old RC crossheads was carried out using the same analytical approach and accounting for an available boundary values. This revealed that for concrete at this age, for relative humidity assumed in the range 50% to 70%, the pH factor of concrete is lower than the threshold value of 11.80 at a concrete depth of 69–82 mm (see results in Tab. 3). It may be noticed that the carbonation depth evaluated is in agreement with results obtained in the chemical test program. Both theoretical and measured pH factor values at a depth of 50 mm from the concrete surface are lower than 11.80 (see Tab. 1).

Table 3

Depth of carbonized concrete layer for 35 years (crosshead)

RH	Depth of concrete layer [mm]
40%	79
50%	82
60%	78
70%	69
80%	54

As this structure was exposed to chloride action, another calculation based on Eq. (2) was performed in order to evaluate the penetration of chloride ions in the concrete depth. The average concentration of chloride ions at the concrete surface for the material obtained from crosshead no. 15 was found at 1.46%. For the analysis, Byfors diffusion coefficient $D = 1.75 \times 10^{-12}$ m^2/s was estimated in relation to concrete properties according to [9, 11]. It is thus determined that the limit amount of chloride ions (0.4%) is exceeded to a depth of 74 mm. The comparison shows the convergence of the results obtained from analysis and measurements. An important observation is that the steel reinforcement state demonstrates advanced corrosion provoked by a high chloride concentration in spite of the alkalinity of the surrounding concrete, but below the safety limit of 11.80.

In situ observations of the structure had confirmed an advanced corrosion level of longitudinal reinforcement in crossheads, especially crosshead no. 15 (Fig. 4). Cracking and splitting of the concrete cover was observed as an effect of the increased volume of corrosion products – most of the surface cracks were located directly above and parallel to the reinforcing steel bars and the splitting of the concrete cover exposed steel for intensified corrosion. Along excessive cracks, reinforcement pitting corrosion was also found (below a leaking expansion joint). The corrosion of bars results in a decrease in their cross-sectional size. The nominal diameter of the main bar of #20 mm was found to have decreased locally to even to 17.6 mm. This decrease causes the simultaneous reduction of the load-bearing capacity – this is investigated in the next part of this paper.

6. Prediction of the durability of the investigated structure

In a reinforced concrete member in which the initiation process of corrosion is theoretically finished the continuous decrease of its load bearing capacity should be considered. The previously described model provides a basis for the prediction of the service life of a given member.

For theoretical evaluation, it is assumed that the service life ends at the time when the estimated load-bearing capacity falls below the extreme value of generalized stress resulting from the predicted load combinations. This approach is used for the safety assessment of a viaduct pier. The reinforced concrete crosshead of the pier is subjected to the analysis regarding both the time of the design and of the investigation. In conclusion, evaluation of its potential durability is carried out.

In order to evaluate the initial safety margin for crosshead no. 15, the bending moment resulting from loads is compared to the evaluation of the load-bearing capacity at a critical cross-section located below a leaking expansion joint (Figs. 3 and 6). The geometry of the cross-section is as follows: $d = 0.69$ m, $A_s = 31.3$ cm^2. The initial safety margin (15%) results from the difference between the initial load-bearing capacity of $M_{Rd} = 773$ kNm and the maximal bending moment in the cross-section at $M_{Ed} = 672$ kNm (Fig. 8). This margin is constant until the corrosion propagation period begins. To establish the relationship between the bar corrosion process and the decrease of structural load-bearing capacity, Eq. (6) based on Faraday's law is used. Thus, with the assumption of an aggressive environment ($i_{cor} = 1.0$ μA/cm^2), the diameter decrease of a steel bar over the course of time can be expressed as:

$$\Delta\phi_i(t) = 0.0232\left(t - t_i\right) \text{ [mm/year]} \tag{7}$$

In result of the theoretical analysis diameter of the corroded bar in the critical section of the crosshead no. 15 was estimated at 17.49 mm. The diameter is determined for the following data: i_{cor} = 1.0 μA/cm^2; α = 4.0; main bar #20 mm; analysis for 27 years of propagation, analysis for 8 years of incubation. The comparison shows the convergence of the results obtained from the analysis (17.49 mm) and measurements (17.6 mm).

For the point in time when renovation started (2013), the residual load bearing capacity in bending was determined at $M_{Rd(35\text{years})}$ = 701.4 kNm. Theoretically, the decreasing load bearing capacity in the analyzed cross-beam would be exceeded after ca. 42 years since the beginning of viaduct life (i.e. 7 years from when the repair was undertaken).

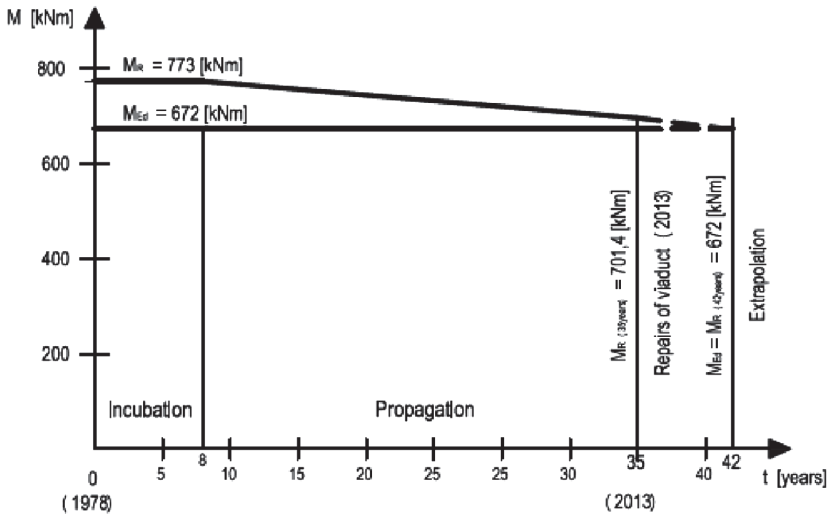

Fig. 8. Bending moment and load-bearing capacity in bending for RC element in critical cross-section

Renovation works will definitely will improve this lifetime – concrete cover is to be rebuilt and a protective layer will be sprayed on the concrete surface. An important issue is that winter treatment of road surfaces may result in accelerated corrosion. For this reason, it is important to ensure permanent water tightness of the water drainage system.

7. Conclusions

The model applied to the considered structure shows a good agreement for the specific case of chloride ingress – the theoretical penetration of chlorides was confirmed by laboratory tests.

Reinforcement corrosion is accelerated by the concentration of chloride ions. In non--carbonated concrete, corrosion of reinforcement is progresses steadily. Higher concentrations of chlorides accelerate the corrosion process.

The influence of corrosion on the decrease of the reinforcement diameter is in good agreement with site observations.

The concentration of chloride ions in one of the investigated members is five times higher than the limit amount which is assumed equal to 0.4% of the weight of cement. Such high value shows the importance of protecting concrete structures from the attack of chlorides used for de-icing road infrastructure.

References

[1] EN 1992-1-1: 2004 + AC:2010, Eurocode 2: Design of concrete structures, General rules and rules for buildings.

[2] Wieczorek G., *Korozja zbrojenia inicjowana przez chlorki lub karbonatyzację otuliny*, Dolnośląskie Wydawnictwo Edukacyjne, Wrocław 2002.

[3] Ajdukiewicz A., *Konstrukcje betonowe projektowane na okres użytkowania – badania a nowe ujęcie normatywne: Problemy naukowo-badawcze budownictwa*, Wydawnictwo Politechniki Białostockiej, Białystok 2007, v. II, 15–38.

[4] Alonso C., Andrade C., Rodriguez J., Diez J.M., *Factors Controlling Cracking of Concrete Affected by Reinforcement Corrosion*, Materials and Structures, Nr 31, 1998, 435–441.

[5] Association Française de Génie Civil, *Conception des bétons pour une durée de vie donnée des ouvrages. Maîtrise de la durabilité vis-à-vis de la corrosion desarmatures et de l'alcali réaction*, Documents scientifiques et techniques, 2004.

[6] Ahmad S., *Reinforcement corrosion in concrete structures, its monitoring and service life prediction-a review*, Cement & Concrete Composites, Vol. 25, 2003, 459–471.

[7] BS 1881: Part 124 Methods for analysis of hardened concrete.

[8] PN-EN 196-2: 2006 Metody badania cementu: Analiza chemiczna cementu.

[9] Neville A.M., *Właściwości betonu*, Polski Cement, wyd. 4, Kraków 2000.

[10] Ściślewski Z., *Trwałość konstrukcji żelbetowych*, Wydawnictwa Instytutu Techniki Budowlanej, Warszawa 1995.

[11] Destrebecq J.-F., Gwoździewicz P., Midro M., *Durability estimation of a reinforced concrete structure with regard to corrosion processes*, 6th International Conference AMCM, Łódź 2008.

[12] Poulsen E., Mejlbro L., *Diffusion of chloride in concrete: Theory and application*, Taylor & Francis, 2006, 442.

TECHNICAL TRANSACTIONS | CZASOPISMO TECHNICZNE
CIVIL ENGINEERING | BUDOWNICTWO
6-B/2014

MARIUSZ MAŚLAK*, ANNA TKACZYK**

A SEMI-GRAPHIC APPROACH TO THE FIRE RESISTANCE ASSESSMENT OF A GABLE STEEL FRAME

CZĘŚCIOWO GRAFICZNA OCENA ODPORNOŚCI OGNIOWEJ STALOWEJ RAMY PORTALOWEJ Z RYGLEM DWUSPADOWYM

A b s t r a c t

An alternative design approach, helpful in the critical temperature evaluation for a gable steel frame exposed to fire, is proposed and discussed in this article. This approach is based on the specification of a system of equilibrium formulae, generalized to the case of fire. All these equations result from the graphical identification of the redundant bending moment distribution in the frame members relating to the particular collapse mechanisms being kinematically admissible. Only such a mechanism which corresponds to the activation of a suitable sequence of the appropriate number of plastic hinges while maintaining the requirements of the classical bending moment redistribution is recognized as conclusive for the considered frame structure.

Keywords: *gable frame*, *fire*, *critical temperature*, *fire resistance*, *static approach*

S t r e s z c z e n i e

W artykule zaproponowano alternatywne podejście do oceny temperatury krytycznej ramy stalowej z ryglem dwuspadowym, eksponowanej ogniowo w warunkach pożaru. Proponowana metodyka obliczeń opiera się na specyfikacji układu równań równowagi, uogólnionych na przypadek pożaru, z których każde wynika z graficznej identyfikacji rozkładu momentów nadliczbowych towarzyszącego analizowanemu kinematycznie dopuszczalnemu mechanizmowi ruchu. Miarodajny dla rozważanej ramy jest mechanizm kojarzony z uruchomieniem sekwencji odpowiedniej liczby przegubów plastycznych przy równoczesnym zachowaniu zasad klasycznej redystrybucji momentów zginających.

Słowa kluczowe: *rama z ryglem dwuspadowym*, *pożar*, *temperatura krytyczna*, *odporność ogniowa*, *podejście statyczne*

* D.Sc. Eng., prof. CUT, Mariusz Maślak, Institute of Building Materials and Structures, Faculty of Civil Engineering, Cracow University of Technology.

** M.Sc. Eng. Anna Tkaczyk, BAUKO Design Company, Kielce, Poland.

1. Introduction

It is common knowledge that the ultimate resistance of the considered load-bearing frame can be easily evaluated due to the succeeding analysis of all collapse mechanisms which may potentially occur in such a structure. The type and the number of the mechanisms required for detailed consideration depend on the support conditions previously assumed. The application of such a well justified approach allows us to quantify the plastic reserve of a structure which is a consequence of the inevitable bending moment redistribution in structural members. However, it is essential to underline the fact that the solution obtained in this way cannot be interpreted as the conclusive value of the frame's plastic resistance, but only as its estimated upper limit. Such an evaluation should be considered as an equivalent to the actual plastic resistance only in cases where it can be verified by an independent study based on the application of the classical static approach to the analysis.

The basis of the applied methodology adopted for the persistent design situation when the structure remains at room temperature is the virtual work equation written as follows:

$$\lambda \sum_i P_i \delta_i = \sum_j M_{pl,j} \varphi_j \tag{1}$$

and specified separately for each mechanism previously identified. In such a formula, index i is the number of the load P_i which performs work at the displacement δ_i being generated by this external force; whereas, index j denotes the location of the plastic hinge being a component of the considered collapse mechanism. The successively formed plastic hinges are characterized by the cross-section resistance $M_{pl,j}$ (i.e. $M^c_{pl,j}$ for the frame columns and $M^b_{pl,j}$ for the frame beam, respectively). Moreover, each of these hinges located in section j is associated with the rotation φ_j which will occur when the analysed potential failure mechanism is activated. Factor λ is the load multiplier, in accordance with the assumption that all external loads applied to the frame grow in time proportionally to the one common parameter. Consequently, the load P_i can increase only up to the point in time when $P_i = P_{i,ult}$. This ultimate value may be defined by the multiplier $\lambda_{\min} = \min_k \lambda_k$ (because $P_{i,ult} = \lambda_{\min} P_i$) which is quantified as a minimum of all the multipliers λ_k resulting from the analysis of each kinematically admissible collapse mechanism (numbered by the index $k = 1, \ldots, m$) [1].

The aim of the presented paper is to generalize this evaluation procedure in order for it to be accurate for calculations regarding situations of a structurally significant fire. It is important that in relation to such exceptional events, the formal assumptions have to be quite different from those previously mentioned. On the one hand, it is necessary to accept that all external loads applied to the structure remain constant during the whole duration of the fire, but on the other hand, it is essential to assume that the member temperature Θ is, at the same time, monotonically increasing. Conclusively, the temperature Θ_{cr}, relating to the frame collapse, is generally interpreted as the critical temperature both for the analysed structure and for the assumed level and arrangement of its external load. Let us note that in the situation of a fire, thermal influences induce the self-equilibrating field of the internal forces in the structure, generated as a result of thermal strain constraints. However, such forces have no influence on the critical temperature evaluation for the considered frame because in Eq. (1), only values of a cross-section plastic resistance $M_{pl,j}$ are taken into account.

The generalization of a classical design procedure to the study of cases of fire is not very difficult if the location of all possible plastic hinges is known in advance and explicitly determined. This means that the conclusive frame collapse mechanism is then possible for identification without significant doubt. The appropriate design algorithm, which is helpful in assessing the critical temperature of a steel frame when exposed to fire, was proposed and discussed in detail by the authors in [2], and afterwards in [3], with further examples and conclusions. However, it seems to be suitable for use only if the input data related to the frame geometry, as well as to the external load arrangement, are not very complex and, moreover, if these are not causing computational inconveniences. In this study, the case of a gable (pitched-roof) steel frame is analysed in detail. All external loads applied to the structure are assumed to be concentrated. In fact, if they are vertical, then they can be transferred into the load-bearing frame by existing purlins. Complementarily, in the case of the horizontal loads, such a transfer is realized by wall beams. Let us note that in the presented study, the potential plastic hinges can occur only in those places where the concentrated loads are applied. This means that for each collapse mechanism which can be activated in the frame, the possible location of all hinges can be determined a priori. However, it is not quite so easy to identify the configuration of the conclusive collapse mechanism, i.e. the one that will be generated first, and, as a consequence, will be characterized by the lowest value of the frame critical temperature. To do this in practice, the previous detailed analysis of each mechanism being kinematically admissible have to be performed separately. To make the process of the evaluation of critical temperature for the whole structure more illustrative, as well as to improve it to be simpler and faster for the designer, an alternative semi-graphical design technique is recommended by the authors in this article. The proposed methodology is based on the specification of the appropriate equilibrium conditions and the number of necessary formulae of this type depends on the redundancy of the considered gable frame. The application of such an approach leads to the evaluation of the frame critical temperature which should be treated only as the lower limitation of its actual value, not as the upper one as was mentioned above when the classical design approach was presented. This fundamental difference results from the fact that the proposed equilibrium formulae can be interpreted as a suitable generalization of those which are typical of the classical static approach to evaluate the ultimate resistance of a structure. Let us note that the assessment obtained in this way is always safe. This is in contrast with evaluations resulting from the application of the typical kinematic approach which are frequently too optimistic and over-estimated.

2. Cross-section plastic resistance under fire conditions

The cross-section plastic resistance $M_{pl,j}$ depends on the value of the yield point f_y specified for the steel which the considered frame is made of. It is a well-known fact that under fire conditions, such a material yield point is considerably reduced because of the high temperature Θ influence. According to the recommendation given in the standard PN-EN 1993-1-2 [4], one can adopt the reduction ratio designated for the characteristic value $f_{y,20}$ and equal to $k_{y,\Theta} = f_{y,\Theta}/f_{y,20}$. Detailed values of this factor, relating to the constructional mild steel and associated with the particular member temperature, are presented in Tab. 1. As is shown, the room temperature Θ = 20°C is interpreted here as the reference temperature.

Consequently, it is easy to note that $f_{y,\Theta} = k_{y,\Theta} f_{y,20}$. Moreover, it is necessary to underline that the same values of the factor $k_{y,\Theta}$ can also be used for the assessment of the reduction ratio of the design value of the steel yield point, because the suitable partial safety factors γ_M are usually adopted to be quantitatively the same both for the persistent design situation and for the accidental situation of a fully developed fire. This means that $\gamma_M = \gamma_{M,fi} = 1.0$ where the lower index "*fi*" is related to the case of a fire.

Table 1

Reduction factors $k_{y,\Theta}$ relating to the characteristic value of material yield point and designated for constructional mild steel exposed to fire, according to PN-EN 1993-1-2 [4]

Θ_a [°C]	≤100	200	300	400	500	600	700	800	900	1,000	1,100	1,200
$k_{y,\Theta}$	1.000	1.000	1.000	1.000	0.780	0.470	0.230	0.110	0.060	0.040	0.020	0.000

Conclusively, if it is assumed that the temperature distribution across the member cross--section is uniform, which means that such a member is uniformly heated and the bending modulus W_{pl} remains constant during the whole duration of the fire, then the reduction of the cross-section plastic resistance at temperature Θ, in relation to the corresponding resistance specified for the room steel temperature, may be evaluated as follows:

$$\frac{M_{pl,j,\Theta}}{M_{pl,j,20}} = \frac{\gamma_M k_{y,\Theta} W_{pl} f_{y,20}}{\gamma_{M,fi} W_{pl} f_{y,20}} = k_{y,\Theta} \tag{2}$$

3. Description of the frame analysed in the example

In the example presented in this article, two kinds of gable steel frame are examined in detail. Both of them have the same dimensions – a height equal to 10 m and a span equal to 30 m; however, they differ from each other in their supporting conditions. The first is simply supported, whereas the second is fully fixed in its foundations (see Fig. 1 in which L = 2 m and h = 3 m). It is also assumed that in both cases, the frame columns are designed from the IPE 500 (for which W^c_{pl} = 2,194 mm^3) and the frame beams from the IPE 360 (for which W^b_{pl} = 1,019 mm^3) steel sections. Moreover, all frame members are made of the S235 grade mild steel, with the characteristic value of its yield point equal to f_y = 235 MPa. Referring to such accepted input data, it is easy to calculate the plastic resistance of the particular member cross-sections, i.e. $M^c_{pl} = W^c_{pl} f_y$ = 515.6 kNm in the case of the frame columns and $M^b_{pl} = W^b_{pl} f_y$ = 239.5 kNm in relation to the frame beams. This gives a ratio of proportionality equal to $\alpha = M^b_{pl}/M^c_{pl}$ = 0.465. Let us note that the value of this ratio remains constant during the whole duration of the fire because the values of the bending modulus, both of W^c_{pl} and of W^b_{pl}, are

independent of the material temperature. Such a conclusion is fully adequate if the fully developed fire is modelled as the reliable fire scenario and the considered frame is exposed to this type of fire. According to this model, the member temperature distribution is uniform, both across the member cross-sections and along the whole of the members length; however, the value of this temperature is increasing together with the fire's intensity. The load arrangement dealing with the external loads applied to the frame is shown in detail in Fig. 1. As is shown, this is the same for both frame types considered in the example.

In Fig. 2, selected possible frame collapse mechanisms are presented. These are kinematically admissible in the case of the frame with fully fixed supports. It is noteworthy that the semi--graphic design technique, recommended by the authors in this article, provides the sought--after solution much faster and, furthermore, it seems to be more illustrative and easier for interpretation than that obtained through the application of the typical calculation methodology.

4. Results obtained for the simply supported frame exposed to fire

Let us start with the analysis of a simply supported frame exposed to fire. The first step is to find the values of redundant internal forces. To do this, the auxiliary, statically determinate frame static scheme should be previously specified. Let such a scheme in this example is the one presented in Fig. 3, with the internal horizontal force H interpreted as an external action applied to the right frame support. This force generates the redundant bending moment distribution with the values, from M_1^0 up to M_{19}^0, presented in Tab. 2.

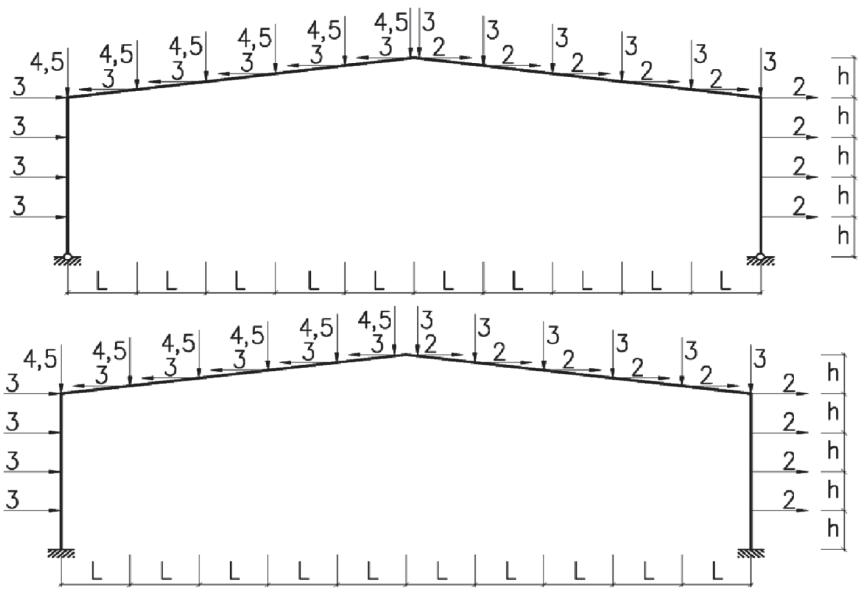

Fig. 1. Analytical schemes and load arrangement specified for the frames considered in the example. Above – the frame being simply supported. Below – the frame being fully fixed in its foundations, $L = 3$ m, $h = 2$ m

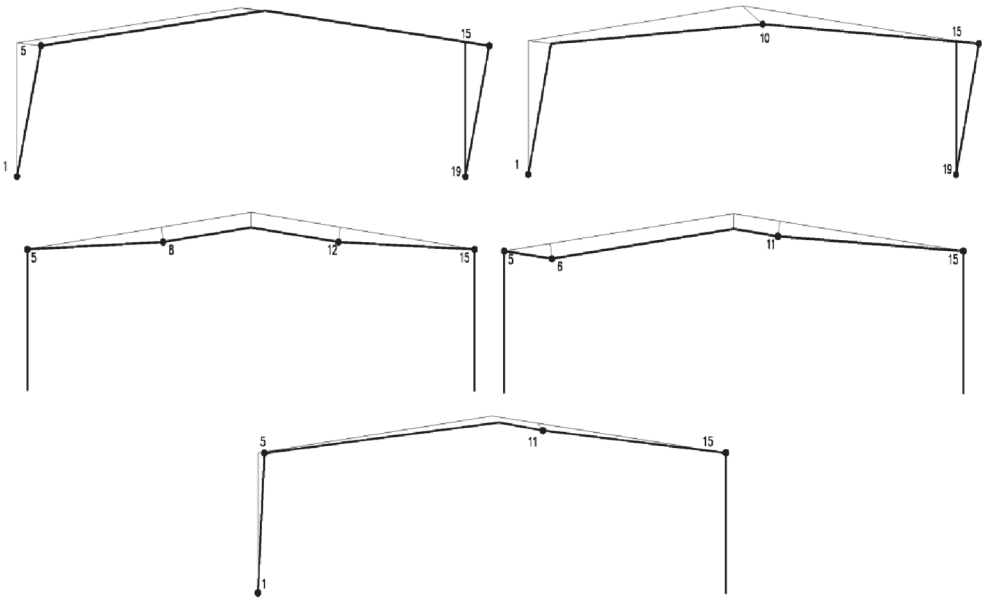

Fig. 2. Selected potential collapse mechanisms, kinematically admissible for the frame being fully fixed in its foundations: 1-5-15-19, 1-10-15-19, 5-8-12-15, 5-6-11-15 and 1-5-11-15, respectively

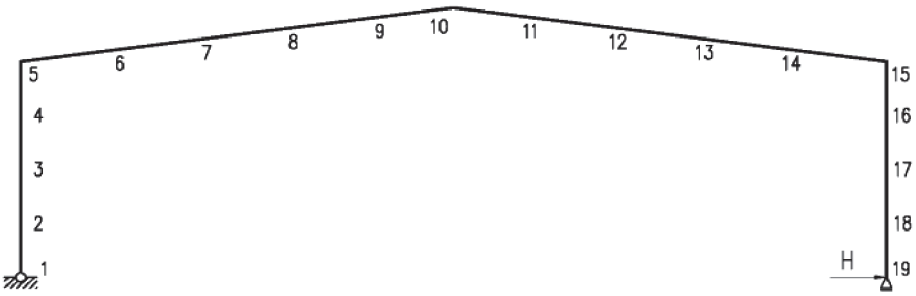

Fig. 3. Statically determinate frame static scheme, adopted to identify the distribution of the redundant internal forces

As a consequence of the application of external forces with the arrangement shown in Fig. 1 to the considered frame characterized by the auxiliary statically determinate static scheme the bending moment distribution is induced in such a structure, presented in Fig. 4.

Next, the primary task is to determine the values of the force H as well as values of the reduction factor $k_{y,\Theta}$ that fulfil the equilibrium conditions specified for the case of fire and for the considered collapse mechanism. Detailed analysis of the diagram presented in Fig. 4 leads to the conclusion that the collapse mechanism, according to which the plastic hinges occur in sections numbered as 10 and 15, is reliable for the conditions adopted in the example. Let us note that in this case, the redundant bending moment diagram is symmetrical (see Fig. 6) then the greater value of a qualitative difference, $M_{10} - M_{15}$ in comparison with the difference $M_{10} - M_5$ being characteristic for the mechanism 5–10 which is also possible to

occur, determines the choice of the first of the compared mechanism as conclusive. However, two different possible cases should be examined separately. The first refers to a situation when the plastic hinge generated in the frame section denoted as 15 occurs in the frame column, whereas the second, in the frame beam. Let us start from the analysis of the first case, presented in Fig. 5.

Table 2

Values of the bending moment generated in the simply supported frame by redundant horizontal force *H* (see Fig. 3)

$M_1^0 = M_{19}^0 = 0$	$M_2^0 = M_{18}^0 = Hh$	$M_3^0 = M_{17}^0 = 2Hh$
$M_4^0 = M_{16}^0 = 3Hh$	$M_5^0 = M_{15}^0 = 4Hh$	$M_6^0 = M_{14}^0 = H\left(4H + \frac{1}{5}h\right)$
$M_7^0 = M_{13}^0 = H\left(4H + \frac{2}{5}h\right)$	$M_8^0 = M_{12}^0 = H\left(4H + \frac{3}{5}h\right)$	$M_9^0 = M_{11}^0 = H\left(4H + \frac{4}{5}h\right)$
$M_{10}^0 = 5Hh$		

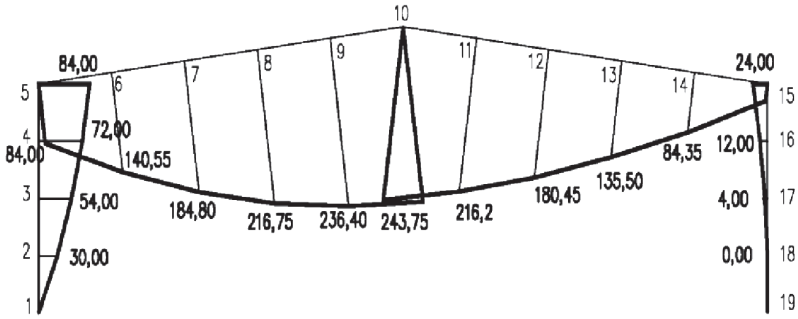

Fig. 4. Bending moment distribution generated by the external load arrangement applied to the frame with a statically determinate static scheme, assumed previously

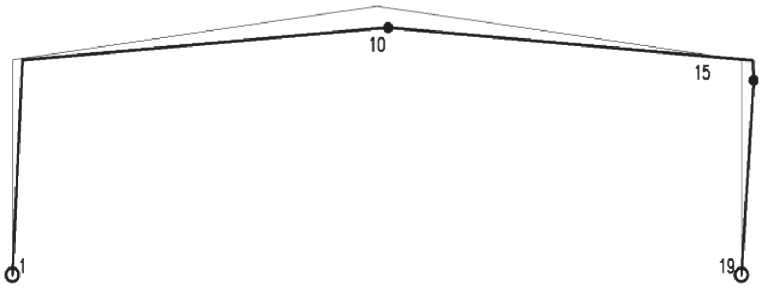

Fig. 5. Collapse mechanism 10-15 specified for the case when the plastic hinge generated in section 15 is activated in the frame column

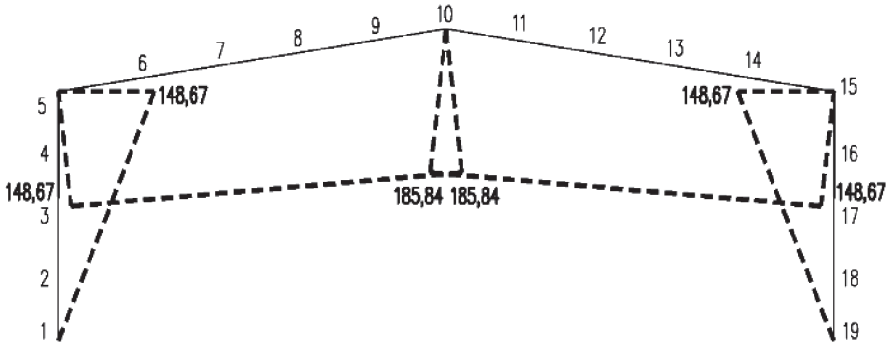

Fig. 6. Redundant bending moment M_i^0 diagram obtained for the force H previously calculated according to Eq. (3)

In such circumstances, the system of two equilibrium formulae can be expressed as follows (see Fig. 7):

$$\begin{cases} M_{10} - M_{10}^0 = k_{y,\Theta} M_{pl}^b = k_{y,\Theta} \alpha M_{pl}^c \\ M_{15} - M_{15}^0 = -k_{y,\Theta} M_{pl}^c \end{cases} \tag{3}$$

Substitution to Eq. (3) of the values M_{10} = 243.75 kNm and M_{15} = 24.00 kNm taken from Fig. 4, as well as the adoption to these formulae of the values M_{10}^0 and M_{15}^0 compiled previously in Tab. 2, lead to the following solutions: H = 18.584 kN and $k_{y,\Theta}$ = 0.242, which means that the critical temperature specified for the whole frame is equal to Θ_{cr} = 666°C (see Tab. 1). In fact, the force H calibrated in this way generates the redundant bending moment M_i^0 diagram shown in detail in Fig. 6. Consequently, the redistribution of the bending moments is performed in the frame members as is shown in Fig. 7. It is easy to see the occurrence of the equilibrium:

$$M_{10}^* = 243.75 - 185.84 = \left|\alpha M_{15}^*\right| = \left|0.465 \cdot \left(24.00 - 148.67\right)\right| = 57.9 \ \text{kNm} \tag{4}$$

and also the conclusive equivalence:

$$M_{pl,\Theta}^b = M_{pl}^b\left(\Theta_{cr}\right) = k_{y,\Theta} M_{pl}^b = 0.242 \cdot 239.5 = 57.9 \ \text{kNm} \tag{5}$$

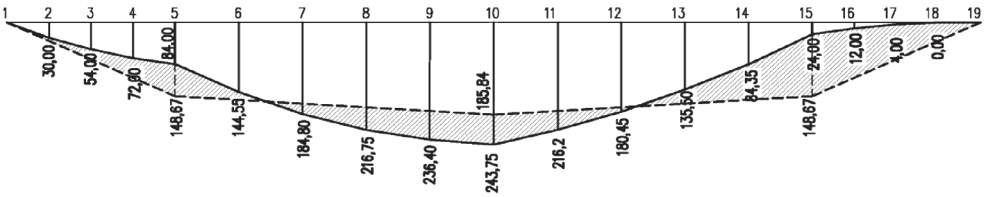

Fig. 7. Bending moment redistribution obtained for the redundant bending moment diagram presented in Fig. 6

However, it is important to underline the fact that such evaluation, i.e. Θ_{cr} = 666°C, cannot be recognized as a correct assessment of the frame critical temperature because it is possible to identify in Fig. 7 some sections, located in the considered frame beam, in which the limitation $M_i^* < M_{i,pl,\Theta}$ is not satisfied. Let us note that the detailed calculation of the value M_5^* and also of the value M_{15}^* is sufficient to reject the solution obtained in the proposed manner. This conclusion means that the analysed collapse mechanism cannot be treated as the reliable one in the presented example.

Quantitatively different evaluation of critical temperature Θ_{cr} is obtained when the second possible collapse mechanism is analysed in detail, according to which, both plastic hinges are generated in the frame beam (see Fig. 8). In this case, Eq. (3) has the form:

$$\begin{cases} M_{10} - M_{10}^0 = k_{y,\Theta} M_{pl}^b \\ M_{15} - M_{15}^0 = -k_{y,\Theta} M_{pl}^b \end{cases} \tag{6}$$

which gives: H = 14.875 kN and $k_{y,\Theta}$ = 0.397 being an equivalent of the assessment Θ_{cr} = 592°C.

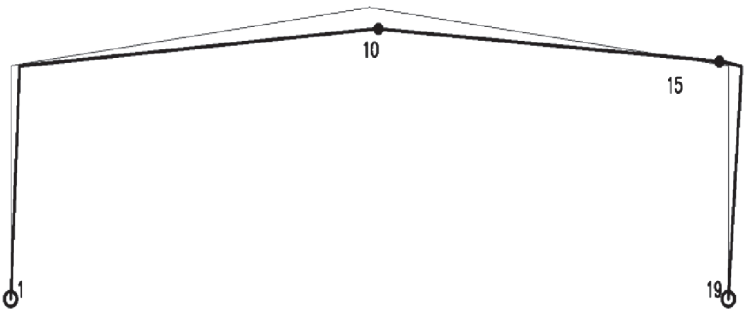

Fig. 8. Collapse mechanism 10-15 specified for the case when the plastic hinge generated in section 15 is activated in the frame beam

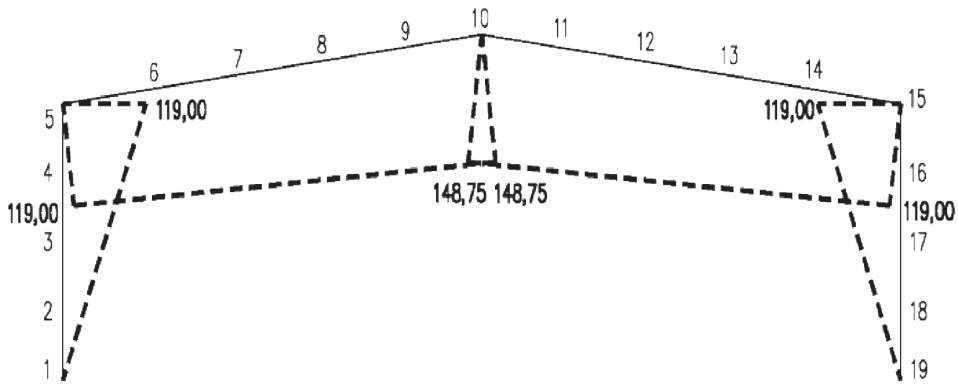

Fig. 9. Redundant bending moment M_i^0 diagram obtained for the force H previously calculated according to Eq. (6)

Such a solution can be easily confirmed by the suitable moment redistribution presented in Figs. 9 and 10. The adequate equilibrium condition is now formulated as follows:

$$M_{10}^{*} = 243.75 - 148.75 = \left|M_{15}^{*}\right| = \left|24.00 - 119.00\right| = 95.0 \text{ kNm} \tag{7}$$

and also the conclusive equivalence:

$$M_{pl,\Theta}^{b} = M_{pl}^{b}\left(\Theta_{cr}\right) = k_{y,\Theta} M_{pl}^{b} = 0.397 \cdot 239.5 = 95.0 \text{ kNm} \tag{8}$$

It is important to note that in this case, the limitation $M_i^* < M_{i,pl,\Theta}$ is satisfied in all sections located in the frame members (obviously, except for the sections denoted as 10 and 15 for which the equivalence $M_{10}^* = M_{15}^* = M_{pl,\Theta}^b$ occurs). As a conclusion, the evaluation $\Theta_{cr} = 592°C$ can be understood as the reliable frame critical temperature value being sought by the fire safety expert.

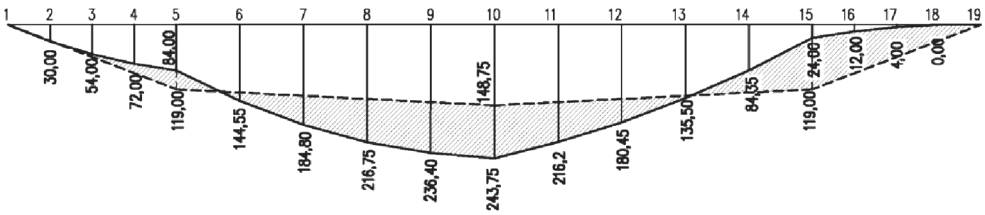

Fig. 10. Bending moment redistribution obtained for the redundant bending moment diagram presented in Fig. 9

5. Example of the frame with fully fixed supports

When the examined frame has all supports designed to be fully fixed (see Fig. 1), then the number of redundant forces necessary to calculate by the specification of the system of the appropriate equilibrium conditions is much greater. Let the auxiliary statically determinate static scheme, helpful in the specification of all redundant forces previously identified, be assumed as shown in Fig. 11.

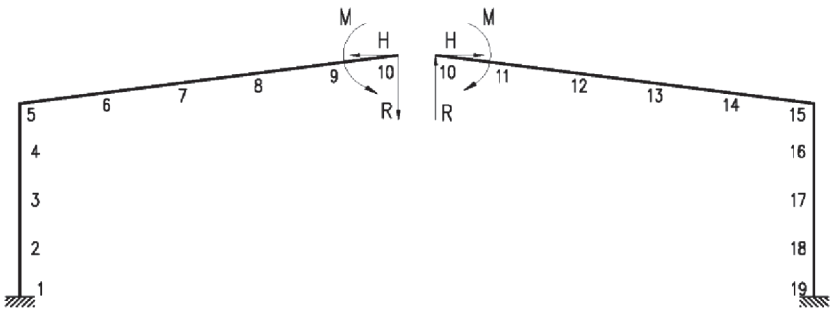

Fig. 11. Statically determinate frame static scheme adopted to identify the distribution of the redundant internal forces

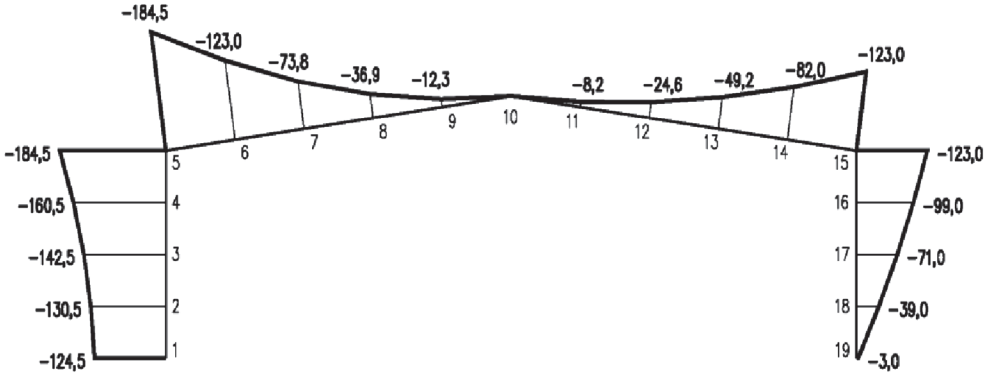

Fig. 12. Bending moment distribution generated by external load arrangement applied to the frame with a statically determinate analytical scheme previously assumed

Table 3

Values of the bending moment generated in the frame with fully fixed supports by redundant forces *M*, *H*, *R* (see Fig. 11)

$M_1^0 = M + 5Hh - 5RL$	$M_2^0 = M + 4Hh - 5RL$
$M_3^0 = M + 3Hh - 5RL$	$M_4^0 = M + 2Hh - 5RL$
$M_5^0 = M + Hh - 5RL$	$M_6^0 = M + \frac{4}{5}Hh - 4RL$
$M_7^0 = M + \frac{3}{5}Hh - 3RL$	$M_8^0 = M + \frac{2}{5}Hh - 2RL$
$M_9^0 = M + \frac{1}{5}Hh - RL$	$M_{10}^0 = M$
$M_{11}^0 = M + \frac{1}{5}Hh + RL$	$M_{12}^0 = M + \frac{2}{5}Hh + 2RL$
$M_{13}^0 = M + \frac{3}{5}Hh + 3RL$	$M_{14}^0 = M + \frac{4}{5}Hh + 4RL$
$M_{15}^0 = M + Hh + 5RL$	$M_{16}^0 = M + 2Hh + 5RL$
$M_{17}^0 = M + 3Hh + 5RL$	$M_{18}^0 = M + 4Hh + 5RL$
$M_{19}^0 = M + 5Hh + 5RL$	

As is shown, the values of three kinds of redundant forces (M, H and R) have to be calculated at the beginning of the analysis directly from the suitable equilibrium formulae. Subsequently, the distribution of the redundant bending moments M_i^0 should be specified, taking into account the equations presented in Tab. 3. The distribution of the bending moments generated as a result of the application of the external load arrangement presented in Fig. 1 to the frame structure with the static scheme being statically determinate is shown in detail in Fig. 12 (let us note that such moments are now negative both in the frame beam and in the frame columns).

The detailed analysis of a bending moment distribution shown in Fig. 12 leads to the conclusion that the reliable collapse mechanism can be only this one according to which three plastic hinges are activated in the frame beam, whereas the fourth one in a frame column. Furthermore, such "beam" hinges have to induce in sections denoted as 5, 10 and 15, while the "column" one – in one from the frame supports, for example in section 1 or in section 19. Let us start from the analysis of the mechanism 1-5-10-15. This is presented in detail in Fig. 13.

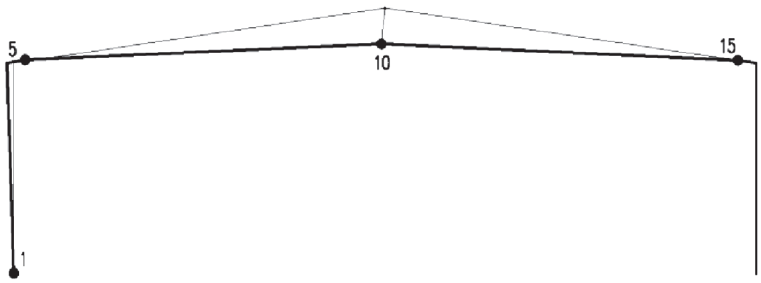

Fig. 13. Collapse mechanism 1-5-10-15 specified for the case when the plastic hinges generated in sections 5 and 15 are activated in the frame beam

For such a case, the suitable system of four equilibrium formulae is expressed as follows:

$$\begin{cases} M_1 + M_1^0 = k_{y,\Theta} M_{pl}^c = k_{y,\Theta} \dfrac{M_{pl}^b}{\alpha} \\ M_5 + M_5^0 = -k_{y,\Theta} M_{pl}^b \\ M_{10} + M_{10}^0 = k_{y,\Theta} M_{pl}^b \\ M_{15} + M_{15}^0 = -k_{y,\Theta} M_{pl}^b \end{cases} \tag{9}$$

This gives the following solutions: M = 60.52 kNm; R = –2.05 kNm; $k_{y,\Theta}$ = 0.253. Such an evaluation of $k_{y,\Theta}$ is the equivalent of the assessment of the frame critical temperature being equal to Θ_{cr} = 660°C (see Tab. 1). However, before accepting this temperature value as the conclusive critical temperature of the considered load-bearing structure, it is necessary to perform the semi-graphic procedure of moment redistribution in the frame members. The basic objective of this is to verify whether the limitation $M_i^* < M_{i,pl,\Theta}$ is satisfied in all sections located outside plastic hinges. In fact, in this example, the redundant forces calculated from Eq. (9) give the redundant moment diagram presented in Fig. 14.

As a result of such an evaluation, the conclusive bending moment redistribution has the form shown in detail in Fig. 15.

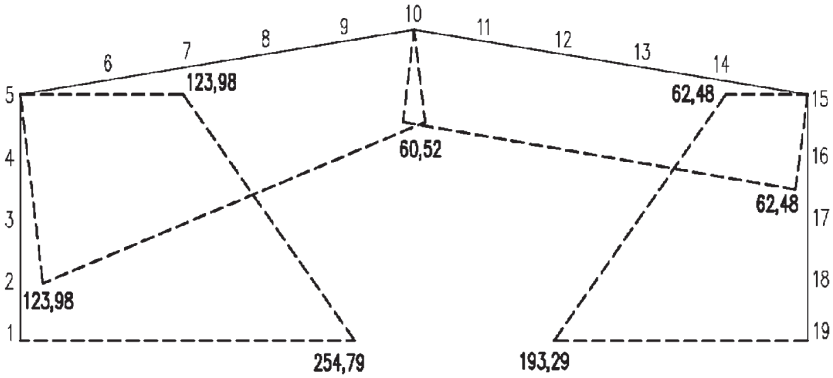

Fig. 14. Redundant bending moment M_i^0 diagram obtained for the forces M, H, R previously calculated according to Eq. (9)

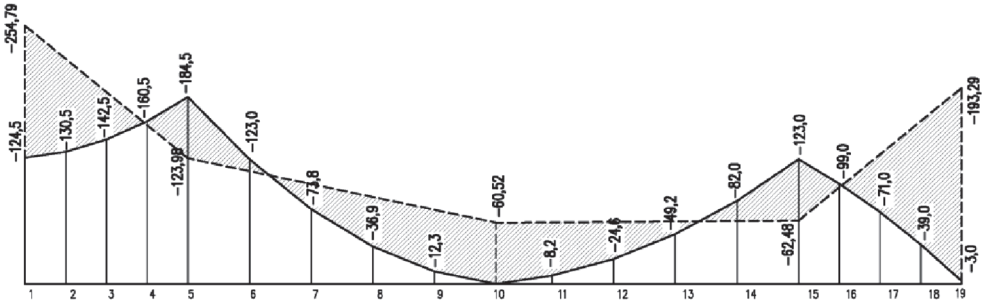

Fig. 15. Bending moment redistribution obtained for the redundant bending moment diagram presented in Fig. 14

As is shown, the equivalences previously assumed are fully satisfied because the following occurs:

$$\begin{aligned} M_1^* &= 0.465\cdot\left(-124.50+254.79\right)=\left|M_5^*\right|=\left|-184.50+123.98\right|=M_{10}^*=0+60.52= \\ &=\left|M_{15}^*\right|=\left|-123.00+62.48\right|=60.52\ \text{kNm} \end{aligned} \tag{10}$$

and also it is true that:

$$M_{pl,\Theta}^b=M_{pl}^b\left(\Theta_{cr}\right)=k_{y,\Theta}M_{pl}^b=0.253\cdot 239.5=60.52\ \text{kNm} \tag{11}$$

Nevertheless, the temperature value Θ = 660°C calculated from Eq. (9) cannot be interpreted as the critical one for the considered frame structure because it is easy to conclude that in section 19 (see Fig. 15), the following inequality occurs

$M_{19}^{*} = -3.00 + 193.29 = 190.29$ kNm $> M_{pl,\Theta}^{c} = 0.253 \cdot 515.6 = 130.45$ kNm. This means that the considered collapse mechanism is not reliable for the initial conditions previously assumed.

Let us analyse the collapse mechanism 5-10-15-19 presented in Fig. 16. The system of the suitable equilibrium formulae now has the form:

$$\begin{cases} M_{19} + M_{19}^{0} = k_{y,\Theta} M_{pl}^{c} = k_{y,\Theta} \dfrac{M_{pl}^{b}}{\alpha} \\ M_{5} + M_{5}^{0} = -k_{y,\Theta} M_{pl}^{b} \\ M_{10} + M_{10}^{0} = k_{y,\Theta} M_{pl}^{b} \\ M_{15} + M_{15}^{0} = -k_{y,\Theta} M_{pl}^{b} \end{cases} \tag{12}$$

which gives the solutions: $M = 65.90$ kNm; $H = 10.97$ kN; $R = -2.05$ kN; $k_{y,\Theta} = 0.275$ being an equivalent of the assessment $\Theta_{cr} = 647°C$ (see Tab. 1).

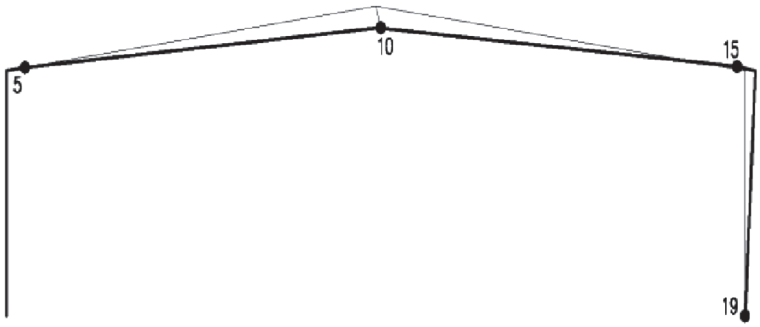

Fig. 16. Collapse mechanism 5-10-15-19 specified for the case when the plastic hinges generated in sections 5 and 15 are activated in the frame beam

The redundant forces, calculated from Eq. (12), lead to the diagram of the redundant bending moments shown in Fig. 17.

Finally, the suitable bending moment redistribution is presented in detail in Fig. 18. It is graphically made to verify the assessment of the frame critical temperature obtained from Eq. (12). It can be seen that the following occurs:

$$\begin{aligned} &\left|M_{5}^{*}\right| = \left|-184.50 + 118.60\right| = M_{10}^{*} = 0 + 65.90 = \left|M_{15}^{*}\right| = \left|-123.00 + 57.10\right| = \\ &= M_{19}^{*} = 0.453 \cdot \left(-3.00 + 144.88\right) = 65.90 \text{ kNm} \end{aligned} \tag{13}$$

and also that:

$$M_{pl,\Theta}^{b} = M_{pl}^{b}\left(\Theta_{cr}\right) = k_{y,\Theta} M_{pl}^{b} = 0.275 \cdot 239.5 = 65.90 \text{ kNm} \tag{14}$$

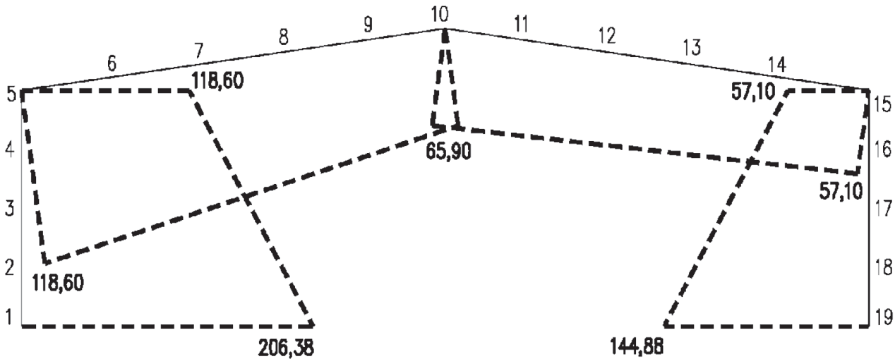

Fig. 17. Redundant bending moment M_i^0 diagram obtained for the forces M, H, R previously calculated according to Eq. (12)

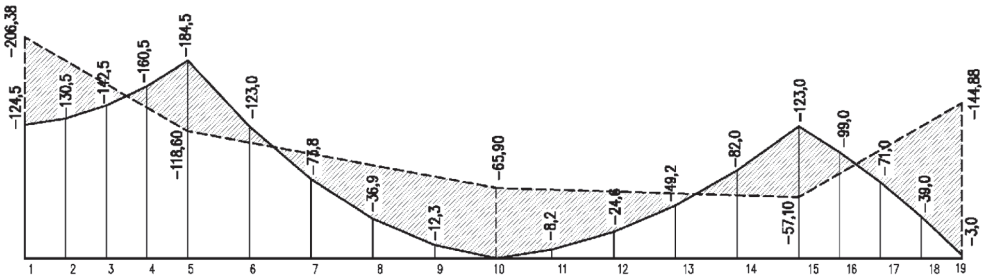

Fig. 18. Bending moment redistribution obtained for the redundant bending moment diagram presented in Fig. 17

The visual observation of the redistribution diagram shown in Fig. 18 leads to the conclusion that the temperature Θ_{cr} = 647°C can be treated as its critical value for the considered frame structure because in all member sections (outside those connected to the activated plastic hinges), the limitation $M_i^* < M_{i,pl,\Theta}$ is fully satisfied.

6. Concluding remarks

An alternative calculation procedure proposed by the authors in this article seems to be simpler and more effective in relation to the classical kinematic approach usually used in the evaluation of the critical temperature of a frame structure exposed to fire. The choice of a conclusive and reliable collapse mechanism, from among those being kinematically admissible, is intuitive and generally unmistakable because it is based on the precise observation of the scheme illustrating the moment redistribution phenomenon. It is essential that the temperature value calculated from the system of the suitable equilibrium formulae can be treated as a sought frame critical temperature only in case when it is possible to prove that the plastic section resistance, reduced because of the high temperature influence, is not reached in any section apart from those in which the plastic hinges are activated. To verify

the fulfillment of this requirement in practice, the visual examination of the redistribution scheme, obtained from the computational algorithm described in detail in this article, is recommended. Such a scheme is generated graphically, so the proposed methodology is partly analytical (equilibrium formulae) and partly graphical. The presented design algorithm is the generalization of the traditional static approach to estimate the ultimate fire resistance of the considered frame. Such finding means that the frame critical temperature estimate calculated in this way is not the exact assessment of such a temperature but only the lower limits of its actual value, relating to the potential perfectly plastic frame failure mode. To evaluate this critical temperature more precisely, a separate analysis, based on the application of the classical kinematic approach, should be performed for comparative purposes [5].

The critical temperature values calculated in the examples presented in this article confirm the rule well known in engineering practice that under fire conditions greater structural redundancy is always connected with a higher level of structural safety. Let us note that the temperature Θ_{cr} = 592°C which is the sought solution obtained for a simply supported frame, is much lower in relation to the temperature Θ_{cr} = 647°C being critical if the frame supports are designed to be fully fixed. However, on the other hand, attaining of sufficient ductility of such a frame is sometimes necessary to ensure the required safety level during fire. In fact, the greater structural redundancy is in general associated with the stronger thermal strains constraints. This can lead to the generation of the higher level of internal forces in the frame members when exposed to fire.

References

[1] Chen W.F., Sohal I., *Plastic design and second-order analysis of steel frames*, Springer Verlag, 1994.

[2] Maślak M., Tkaczyk A., *Fire resistance of simple steel frame – kinematic approach to evaluation*, Proceedings of 6th European Conference on Steel and Composite Structures "Eurosteel 2011", Budapest, Hungary, August 31–September 2, 2011, Vol. B, 1497–1502.

[3] Maślak M., Tkaczyk A., *Oszacowanie nośności granicznej ramy stalowej w pożarze rozwiniętym*, Inżynieria i Budownictwo, 3/2012, 160–163.

[4] EN 1993-1-2, Eurocode 3: Design of Steel Structures, Part 1–2: General Rules – Structural Fire Design.

[5] Maślak M., Tkaczyk A., *Szacowanie temperatury krytycznej ogarniętej pożarem stalowej ramy portalowej z wykorzystaniem chwilowego środka obrotu*, Materiały II Międzynarodowej Polsko-Ukraińskiej Konferencji Naukowo-Technicznej „Aktualne Problemy Konstrukcji Metalowych APKM 2014", Gdańsk, 27–28.11.2014, ISBN: 978-83-931174-3-7, 163–166.

TECHNICAL TRANSACTIONS | CZASOPISMO TECHNICZNE
CIVIL ENGINEERING | BUDOWNICTWO
6-B/2014

MICHAŁ PAZDANOWSKI*

RESIDUAL STRESS DEVELOPMENT IN RAILROAD RAILS – A PARAMETRIC STUDY

STUDIUM PARAMETRYCZNE NAPRĘŻEŃ RESZTKOWYCH W SZYNIE KOLEJOWEJ

A b s t r a c t

This paper presents the results of a parametric study undertaken to analyse the influence that changes in the material model and contact zone parameters may have on residual stress levels. A simplified shakedown based mechanical model is used to estimate the residual stress distributions due to simulated contact loads. An information on final shakedown state of the rail subjected to given loading program is obtained at a substantially reduced computational cost compared to the standard incremental analysis. A 50% increase in peak contact pressure may increase the longitudinal residual stress level by over 700%. The dependence of peak residual stresses on changes in the hardening ratio is almost linear, while the dependence of peak residual stresses on changes in the yield limit indicates a quadratic relationship. The research indicates that in future applications, a simplified treatment of the rail/wheel interface is justified, as long as the peak pressure in the contact zone is estimated correctly. The residual stresses in rails induced by service conditions may reach very high values, on a par with the material yield limit. This effect is aggravated by the operating procedure of increasing wheel axle loads.

Keywords: *residual stresses*, *numerical techniques*, *material properties*

S t r e s z c z e n i e

W niniejszym opracowaniu przedstawiono wyniki studium parametrycznego przeprowadzonego w celu zbadania wpływu zmian modelu materiału i parametrów strefy kontaktu na poziom naprężeń resztkowych w szynie kolejowej. Uproszczony model mechaniczny, oparty na teorii plastycznego przystosowania, został zastosowany do oszacowania rozkładu naprężeń resztkowych wywołanych symulowanymi obciążeniami kontaktowymi. Stwierdzono, że 50% wzrost maksymalnego ciśnienia w strefie kontaktu skutkuje wzrostem maksymalnych naprężeń resztkowych o około 700%, przy czym zależność maksymalnych naprężeń resztkowych od zmian współczynnika wzmocnienia materiału szyny ma charakter liniowy, podczas gdy zależność tych samych naprężeń od wartości granicy plastyczności ma charakter kwadratowy. Przeprowadzone obliczenia wskazują, że uproszczone traktowanie strefy kontaktu koło/szyna jest uzasadnione, jak długo maksymalne wartości ciśnienia w tej strefie są oszacowane poprawnie. Naprężenia resztkowe w szynie kolejowej, wywołane przez obciążenia eksploatacyjne kołami taboru, mogą osiągnąć bardzo duże wartości, porównywalne z wartością granicy plastyczności materiału. Efekt ten pogłębia się na skutek zwiększania obciążeń na oś taboru.

Słowa kluczowe: *analiza i modelowanie*, *naprężenia resztkowe*, *metody numeryczne*, *własności materiału*

* Ph.D. Michał Pazdanowski, Institute for Computational Civil Engineering, Faculty of Civil Engineering, Cracow University of Technology.

1. Introduction

Rail breakages may be counted among the important factors negatively affecting the safety of railroad operations. Although this does not usually lead to extreme consequences, unfavourable conditions may result in the catastrophic failure of a section of rail, followed by derailment, loss of life and substantial damage to property [25, 27]. Research [24] shows, that there is a long term growing trend behind this phenomenon, due to heavier axial loads, increased volumes of traffic and longitudinal tensile stresses in low temperatures in continuously welded rails. The economic costs of rail fracture in European Union alone are estimated at €200 million [1].

Research [11] indicates that the rail failure is at least in part to blame on excessive residual stress levels in rails [6, 9, 23] attained during manufacture and service life. Therefore, an effort has been undertaken to estimate the residual stress levels induced in the railroad rail during manufacturing (heat treatment and subsequent straightening) as well as service using both experimental [10, 11, 28] and numerical [20, 22] approaches. Since a traditional elastic-plastic incremental analysis of multiple rolling contacts during service is very time consuming [4], a simplified model of residual stress calculation based on shake-down and Melan's [12] theorem was proposed, first for elastic-perfectly plastic material model [14], and later on, extended for elastic-plastic material exhibiting hardening [2, 17].

The research reported in this paper deals with the application of these basic and extended material models to estimate the changes in residual stress levels in railroad rails due to variations in certain parameters of the rail/wheel contact interface as well as material properties (yield limit and hardening ratio). The results of calculations may yield valuable insights regarding the influence that the deterioration of rail material properties exerts on residual stresses in the rail head.

2. Mechanical model

The mechanical model developed to deal with residual stresses emerging as a result of repetitive contact loads in elastic-plastic material exhibiting kinematic hardening may be presented as the following two step:

I compute the correlation matrix A_{ijkl}:

$$\sigma_{ij}^{r} = A_{ijkl}\ \varepsilon_{kl}^{p} \tag{1}$$

solving the following nonlinear constrained optimization problem for self-equilibrated stresses σ_{ij}^{r} as a function of plastic distortions ε_{ij}^{p}:

$$\min_{\varepsilon_{ij}^{p}} \Theta\left(\sigma_{ij}^{r}\right),\ \ \Theta\left(\sigma_{ij}^{r}\right) = \int_{V} \sigma_{ij}^{r}\ C_{ijkl}\ \sigma_{kl}^{r}\ dV - \int_{V} \varepsilon_{ij}^{p}\ \sigma_{ij}^{r}\ dV \tag{2}$$

at:

$$\sigma^{r}_{ij,j} = 0, \qquad \text{in } V \text{ – internal equilibrium conditions,} \tag{3}$$

$$\sigma^{r}_{ij}\ n_j = 0, \qquad \text{on } \partial V \text{ – static boundary conditions,} \tag{4}$$

II find plastic distortions ε^{p}_{ij}, minimizing the total complementary energy functional:

$$\min_{\varepsilon^{p}_{ij}} \Psi\left(\varepsilon^{p}_{ij}\right),\ \ \Psi\left(\varepsilon^{p}_{ij}\right) = \int_V \varepsilon^{p}_{gh}\ A^{T}_{ghij}\ C_{ijkl}\ A_{klmn}\ \varepsilon^{p}_{mn}\ dV \tag{5}$$

at:

$$\Phi\left(A_{ijkl}\ \varepsilon^{p}_{kl} + c\ \varepsilon^{pc}_{ij} + \sigma^{E}_{ij} + \sigma^{t}_{ij}\right) - 1 \le 0, \text{ in } V \text{ – yield conditions,} \tag{6}$$

where:

$$c = \frac{E \cdot H}{E - H} \quad \text{– kinematic hardening parameter.}$$

The following denotations hold in formulas (1) through to (6):

σ^{r}_{ij} – residual stresses induced in the body by the applied cyclic loading program,

ε^{p}_{ij} – plastic distortions,

ε^{pc}_{ij} – plastic distortions assumed to have constant spatial distribution during iteration,

σ^{E}_{ij} – elastic stresses (calculated as if the body deformed purely elastically during the considered cyclic loading program),

σ^{t}_{ij} – thermal stresses (calculated as if the body deformed purely elastically during the service induced heating),

A_{ghij} – correlation matrix linking plastic distortions and residual stresses,

C_{ijkl} – elastic compliance matrix,

E – Young modulus,

H – elastic plastic tangent modulus.

In order to ensure the convergence of computer routines, plastic distortions have to be determined using the iterative approach:

$$^{n}\varepsilon^{pc}_{ij} = \lambda\ {}^{n-1}\varepsilon^{pc}_{ij} + (1-\lambda)\ {}^{n-2}\varepsilon^{pc}_{ij},\ \ \lambda \in (0,1), \tag{7}$$

where, during iteration 1 initial plastic distortions ${}^{0}\varepsilon^{pc}_{ij} = 0$, and during subsequent iterations the above formula (7) is used to determine the current levels of plastic distortions. Numerical tests have shown [18] that such an iterative procedure is convergent, and while any value of λ belonging to the interval (0, 1) may be used, $\lambda = 0.5$ led to the final, stable spatial distribution of plastic distortions in the lowest number of iterations. This number of iterations never exceeded 19, though numerical solutions of sufficient quality have been obtained in as few as 7 iterations [18].

3. Numerical procedure

The mechanical problem delineated in (2)–(6) may be analyzed using any discrete method (such as Boundary Element [29], Finite Element [3], or Finite Difference [5]). For the purpose of this research, the Finite Difference Method (FDM) generalized for arbitrary irregular grids [7, 8, 13] has been used to solve the problem on a set of nodes distributed in a cross-section. In order to develop the necessary approximation formulas for functions and their first derivatives at discrete locations, a local coordinate system is introduced at such points of interest (Fig. 1). Then the unknown function is expanded into a Taylor series with respect to neighbouring nodes:

$$f_j = f_0 + h_j \cdot \frac{\partial f_0}{\partial x} + k_j \cdot \frac{\partial f_0}{\partial y} + \frac{h_j^2}{2} \cdot \frac{\partial^2 f_0}{\partial x^2} + h_j \cdot k_j \cdot \frac{\partial^2 f_0}{\partial x \partial y} + \frac{k_j^2}{2} \cdot \frac{\partial^2 f_0}{\partial y^2} + O\left(r^3\right) = \tilde{f}_j + O\left(r^3\right) \quad (8)$$

where:

$$h_j = x_j - x_0, \quad k_j = y_j - y_0, \quad (9)$$

$$r_j = \sqrt{h_j^2 + k_j^2} \quad (10)$$

f_j – value of the function $f = f(x, y)$ at the node j adjacent to the point of interest,
f_0 – value of the function f at the point of interest, i.e. $f_0 = f(x_0, y_0)$.

A weighted minimization method is subsequently applied in order to find a local approximation of the unknown function $f(x, y)$ by a surface of the requested order. In the case of the second order surface, the following weighted error functional is built:

$$B = \sum_{j=1}^{n} \left[\left(-f_j + f_0 + h_j \cdot \frac{\partial f_0}{\partial x} + k_j \cdot \frac{\partial f_0}{\partial y} + \frac{h_j^2}{2} \cdot \frac{\partial^2 f_0}{\partial x^2} + h_j \cdot k_j \cdot \frac{\partial^2 f_0}{\partial x \partial y} + \frac{k_j^2}{2} \cdot \frac{\partial^2 f_0}{\partial y^2} \right) \cdot \frac{1}{r^{p+1}} \right]^2 \quad (11)$$

where j enumerates all the nodes adjacent to the point of interest, p denotes the truncation level of the Taylor series, and at the same time order of the approximating surface. B is minimized with respect to the unknown function f and its derivatives at the point of interest (x_0, y_0). In this manner, a set of linear equations is generated which is later solved for the unknown finite difference coefficients of function and its derivatives at the point of interest.

This weighted minimization method may be used to compute approximate value of function f or to determine coefficients of finite difference operators. Thus, the function or its derivatives may be approximated at any point, like Gauss stations or equilibrium equations, and yield conditions application points (Fig. 2).

Finally, a variant of the Feasible Directions Method [15], tailored to the quadratic objective function (5) and constraints (6) has been applied to solve the optimization problem (5), (6) for plastic distortions.

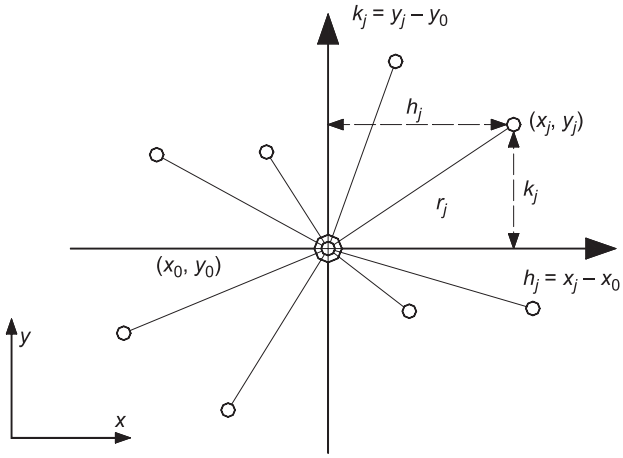

Fig. 1. Irregular set of nodes for finite difference operator

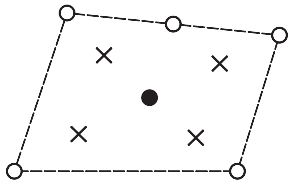

Fig. 2. Approximation and integration between nodes: ○ – nodes j, ✕ – Gauss stations, ● – equilibrium equations and yield condition application point

4. Parametric studies

The following material data have been used for comparative calculations:

Rail	132RE
Young modulus	E = 206 GPa
Yield limit	Y = 480 MPa
Poisson's ratio	v = 0,3
Track foundation modulus	kv = 20.6 MPa
Static wheel load	P = 120, 134, 147, 160, 178 kN

These have been chosen to realistically represent the conditions existing on heavy haul revenue railroads [23]. The following studies have been undertaken to examine the dependence of residual stresses in the railroad rail on certain parameters of the contact interface: pressure distribution in the contact zone, changes in the yield limit, changes in the hardening ratio.

The standard approach of the operating procedure used to determine pressure distribution in the wheel/rail interface on North American railroads [16] is to calculate the contact area

using standard elastic Hertz formulae for two curved bodies in contact, then to find a rectangle of an equivalent area and having a ratio of $c_z/c_x = 1.6$ (c_z is aligned with the longitudinal axis of rail). A biparabolic pressure distribution over such a rectangle has been assumed to be correctly approximating the real one, while the peak pressure p_0 has been computed via the static equivalence requirement of the applied wheel load P and the pressure distribution assumed, leading to the formula:

$$p_0 = \frac{9}{4} \cdot \frac{P}{c_x \cdot c_z} \tag{12}$$

The real rail/wheel interface differs substantially from the standard Hertz contact problem (elastic-plastic rolling contact vs. static elastic contact). This includes the shape of the contact zone as well as the pressure distribution within the contact area [26]. Since no reliable experimental data is available, the parametric study presented here was intended to investigate the influence these two parameters of rail/wheel contact (patch shape and size, peak contact pressure) have on levels of residual stresses in the rail. Four separate pressure distributions spanned over a rectangle (Fig. 3a)–c)) and a diamond (Fig. 3d)) were selected as simplified geometrical forms corresponding to the computer simulations of pressure distribution in rail/wheel interface in both elastic [30] and elastic-plastic rolling contact [19]. The analysis was accomplished during three separate tests, applying the loads listed above.

In the first test, a static wheel load of 147 kN was applied to the rail, spanned over the areas depicted in Fig. 3. Based on the results of this test, for the remaining tests a pressure distribution, depicted in Fig. 3a), was used. In the second test, a constant patch size was kept irrespective of the load level, while peak pressure was adjusted to satisfy the equilibrium condition; in the third test, the opposite was true. In all cases, the load was applied at the rail axis of symmetry. Some of the test results are presented in Figs. 4 and 5.

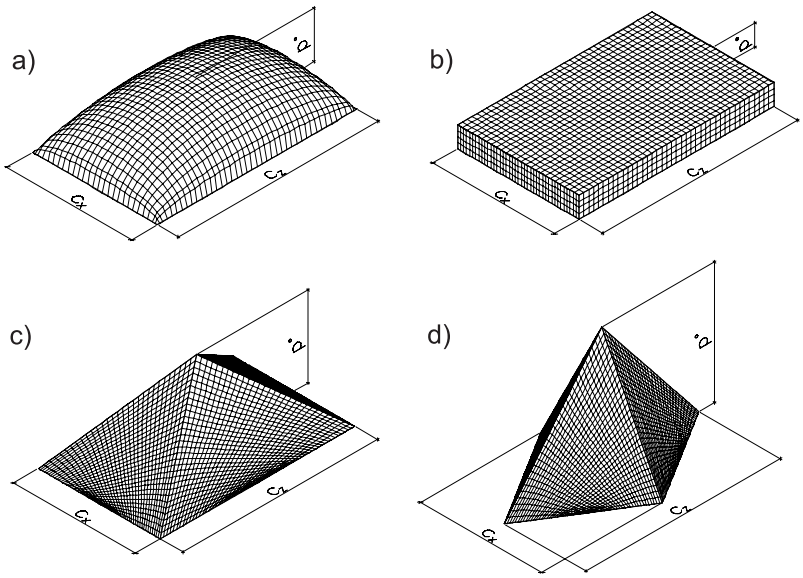

Fig. 3. Pressure distributions used in parametric study

As Figs. 4 and 5 indicate, an increase in peak contact pressure does not affect the location of peak compressive σ_{zz} residual stress, while it does substantially affect the depth of peak tensile σ_{zz} residual stress location, pushing it downwards by about 7 mm. However, if the peak contact pressure is kept constant, both values and locations of peak tensile and compressive σ_{zz} residual stresses remain fairly stable as may be observed in Figs. 5 and 6.

In the following group of tests, the combined effect that the changing yield limit and hardening ratio may exert on the level of residual stresses in the railroad rail has been investigated. The 147 kN load was again applied at the rail crown. The residual stresses have been determined fifteen times, in three groups of five tests in order to cover all possible yield limit/hardening ratio combinations while assuming predetermined ±5% and ±10% fluctuations of the 480 MPa yield limit value and ±10% fluctuations of the assumed hardening ratio $c = 1/9$ (Figs. 7 and 8).

The results obtained during these calculations seem to indicate that the service induced peak residual stresses exhibit quadratic dependence on the yield limit, irrespective of the hardening ratio assumed, at least within the bounds considered in this study. At the same time, the influence of changes in the hardening ratio on peak residual stresses seems to be negligible within the considered bounds, as may be observed in Fig. 7, where the peak stress evolution curves corresponding to the considered hardening ratios follow each other closely.

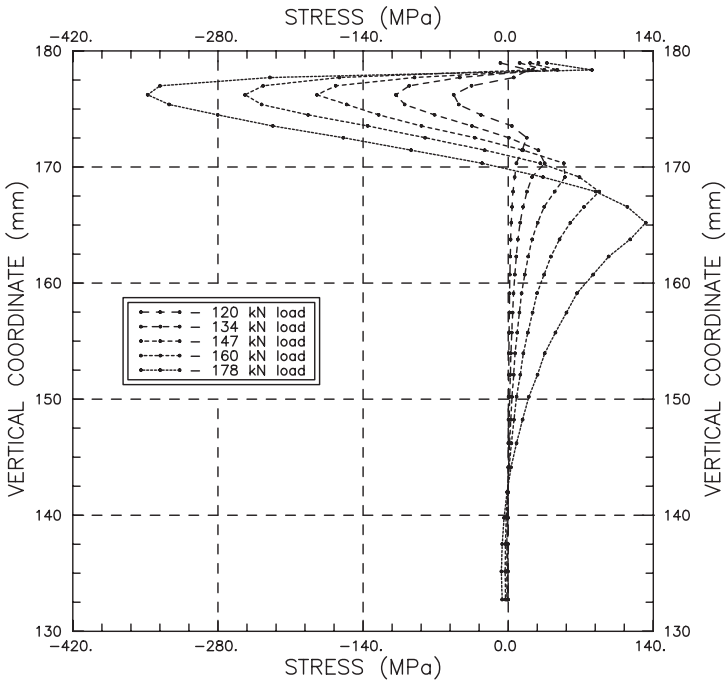

Fig. 4. Longitudinal residual stress along the rail's vertical axis of symmetry vs. the distance from rail foot, constant patch case

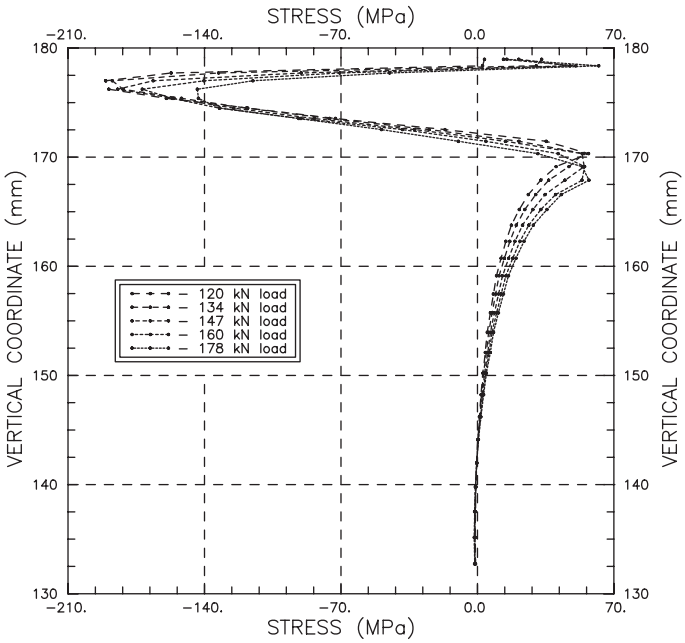

Fig. 5. Longitudinal residual stress along the rail's vertical axis of symmetry vs. the distance from the rail foot, constant peak pressure case

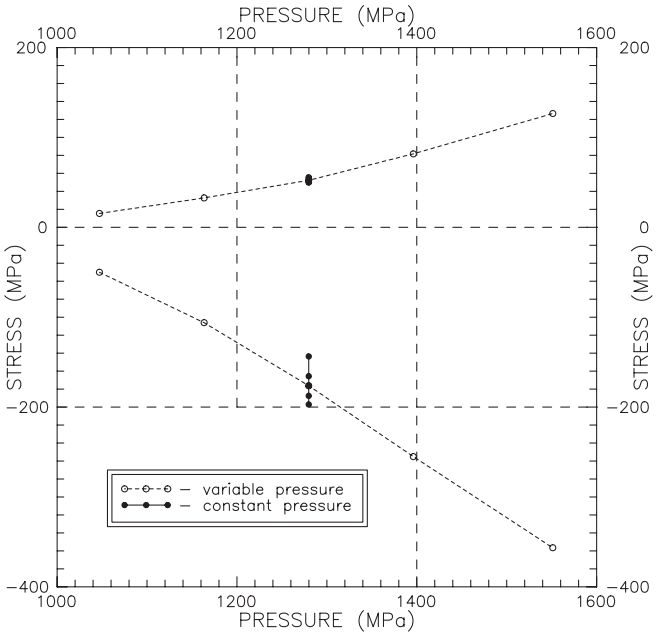

Fig. 6. Peak longitudinal residual stress values in the cross-section vs. peak contact pressure (positive value denotes tension)

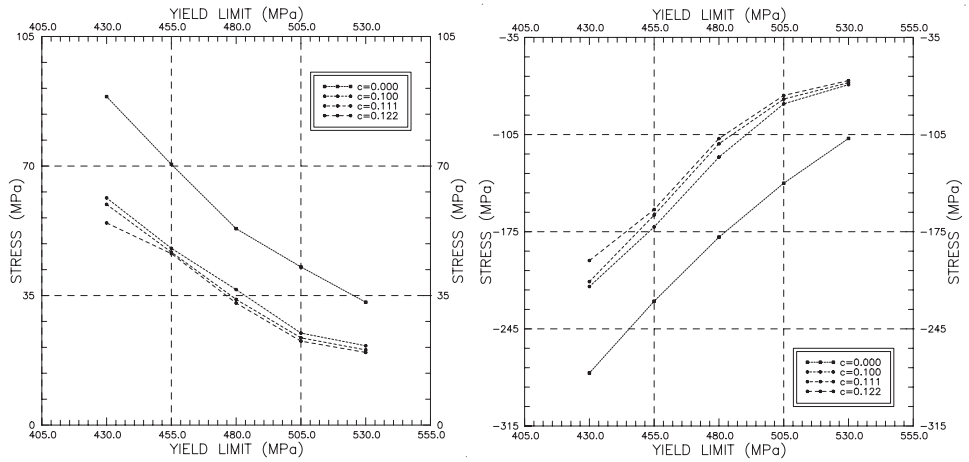

Fig. 7. Peak longitudinal residual stress, vs. yield limit, tension (left) and compression (right); $c = 0.0$ – perfect plasticity

The near-horizontal lines depicting dependence of peak residual stresses on the hardening ratio in Fig. 8 for all analyzed yield limit values corroborate this observation.

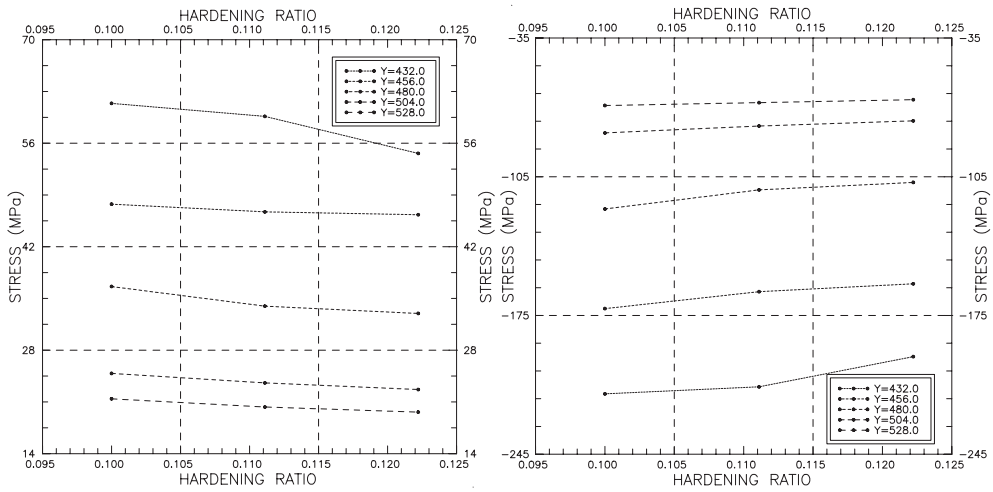

Fig. 8. Peak longitudinal residual stress versus hardening ratio, tension (left) and compression (right); Y – yield limit

Results obtained for all the considered yield limit fluctuations around the reference value of 480 MPa at the hardening ratio of $c = 1/9$, but representative for all the considered yield limit/hardening ratio scenarios, are presented in the Tab. 1. These results indicate that

a 10% decrease in material yield limit results in an approximately 80% increase in peak values of residual stresses with an exception of σ_{yy}, for which this ratio is substantially lower (approximately 30% in compression and 60% in tension), while a 10% increase in material yield limit results in an approximately 40% decrease in respective stress values, again, with an exception of σ_{yy}, for which this ratio is closer to 25%.

Table 1

Relative changes in peak values of residual stress components in rail

LOADING CASE (change in yield limit)	STRESS CHANGE [%]							
	σ_{xx}		σ_{yy}		σ_{zz}		σ_{xy}	
	min.[2)]	max.[2)]	min.[2)]	max.[2)]	min.[2)]	max.[2)]	min.[2)]	max.[2)]
1 (–10%)	74.26	82.29	26.77	62.43	89.03	75.61	72.20	72.20
2 (–5%)	37.60	41.29	13.13	26.93	46.02	37.58	39.14	39.14
3 (0%)[1)]	0.00	0.00	0.00	0.00	0.00	0.00	0.00	0.00
4 (+5%)	–41.48	–32.65	–15.63	–23.23	–28.86	–30.57	–23.77	–23.77
5 (+10%)	–35.98	–41.69	–23.43	–29.31	–39.43	–40.18	–35.69	–35.69

[1)] – a reference solution;
[2)] – min. – compression, max. – tension.

5. Conclusions

The following conclusions have been drawn with respect to the residual stress distributions in railroad rails and peak levels of these stresses based on the test results:

a) the residual stresses are not very sensitive to the shape of the contact zone and the shape of pressure distribution, but peak contact pressure matters;
b) the general distribution of residual stresses (location of compressive and tensile zones and points of peak pressure) is practically immune to changes in the way in which the contact load is applied, as long as the peak pressure remains unchanged;
c) a 50% increase in peak contact pressure may increase the longitudinal residual stress level by over 700% (see Figs. 4 and 6);
d) dependence of peak residual stresses on changes in the hardening ratio is almost linear (with the one exception being the weakest material) within the bounds considered, this dependence is negligible;
e) dependence of peak residual stresses on changes in the yield limit indicates a quadratic relationship, weakening at the highest yield limits; moderate changes in the yield limit result in very substantial changes to peak stress values (an up to 9:1 ratio of the relative stress change to the relative yield limit change is observed for the longitudinal residual stress) (see Tab. 1).

The following further actions are proposed to enhance and improve the presented mechanical/numerical model in order to better approximate the residual stress distributions in the railroad rail subject to service conditions:

a) modelling of wear due to contact phenomena on the rail/wheel interface, or due to maintenance procedures (grinding);
b) inclusion of the residual stress state introduced by the manufacturing process (quenching and roller straightening) in the analysis of residual stresses due to live loads;
c) application of a fuzzy sets theory to estimate the effect that fluctuations in material constants' values and parameters of contact may have on the residual stresses.

Ultimately, knowledge of the full evolution of residual stress state is sought as a prerequisite for accurate life prediction of railroad rail affected by fatigue failure. This evolution includes manufacturing process (quenching and roller straightening), with inherent variations in material properties, track laying (neutral temperature and buckling risk), application of live loads (wheel wandering and wear), and maintenance (grinding).

References

[1] Cannon D.F., Edel K.-O., Grassie S.L., Sawley K., *Rail defects: an overview*, Fatigue Fract. Engng Mater. Struct., 2003, Vol. 26, 865–887.

[2] Cecot W., Orkisz J., *Prediction of Actual Residual Stresses Resulting from Cyclic Loading in Kinematic Hardening Material*, Proc. of the International Conference COMPLAS V, Barcelona 1997, 1879–1891.

[3] Crisfield M.A., *Non-linear Finite Element Analysis of Solids and Structures*, Wiley&Sons, 1994.

[4] Dang Van K., Maitournam M.H., Prasil B., *Elastoplastic analysis of repeated moving contact. Application to railways damage phenomena*, Wear, 1996, Vol. 196, 77–81.

[5] Forsythe G.E., Wasow W.R., *Finite Difference Methods for Partial Differential Equations*, Wiley, New York 1960.

[6] Groom J.J., *Determination of Residual Stresses in Rails, Batelle Columbus Laboratories*, Rpt. no. DOT/FRA/ORD-83-05, Columbus 1983.

[7] Jensen P.S., *Finite Difference techniques for variable grids*, Computers and Structures, 1972, Vol. 2, 17–29.

[8] Liszka T., Orkisz J., *The finite Difference at Arbitrary Irregular grids and its applications in applied mechanics*, Computers and Structures, 1980, Vol. 11, 109–121.

[9] Lo K.H., Mummery P., Buttle D.J., *Characterisation of residual principal stresses and their implications on failure of railway wheels*, Engng Failure Analysis, 2010, Vol. 17, 1273–1284.

[10] Magiera J., Orkisz J., Karmowski W., *Reconstruction of residual stresses in railroad rails from measurements made on vertical and oblique slices*, Wear, 1996, Vol. 191, 78–89.

[11] Marchenko H.P., *Influence of residual stresses on the stress intensity factors for a surface cracking the rail head*, Materials Science, 2010, Vol. 46, 64–69.

[12] Martin J.B., *Plasticity – fundamentals and general results*, The MIT Press Publ., 1975.

[13] Milewski S., Orkisz J., *Improvements in the global a-posteriori error estimation of the FEM and MFDM solutions*, Computing and Informatics, 2011, Vol. 30, 639–653.
[14] Orkisz J., Orringer O., Hołowiński M., Pazdanowski M., Cecot W., *Discrete Analysis of Actual Residual Stresses Resulting from Cyclic Loadings*, Computer and Structures, 1990, Vol. 35, 397–412.
[15] Orkisz J., Pazdanowski M., *On a new Feasible Directions solution approach in constrained optimization*, [in:] *The Finite Element Method in the 1990s*, Springer Verlag, 1991, 621–632.
[16] Orringer O., Tang Y.H., Gordon J.E., Morris J.M., Perlman A.B., *Crack propagation life of detail fractures in rail*, US DOT Final Rpt., DOT-TSC-FRA-88-1, Cambridge, MA 1988.
[17] Pazdanowski M., *On estimation of residual stresses in rails using shake-down based method, Archives of Transport*, 2010, Vol. 22, 319–336.
[18] Pazdanowski M., *Prediction of Residual Stresses in Railroad Rails by the Constrained Complementary Energy Minimization Shake-Down Method*, Final Rpt. to the US DOT, FRA, Washington DC, to be published.
[19] Ringsberg J.W., Josefson B.L., *Finite element analyses of rolling contact fatigue crack initiation in railheads*, J. Rail Rapid Transit, 2001, Vol. 215, 243–259.
[20] Ringsberg J.W., Lindback T., *Rolling contact fatigue analysis of rails including numerical simulations of the rail manufacturing process and repeated wheel-rail contact loads*, Int. J. of Fatigue, 2003, Vol. 25, 547–558.
[21] Sasaki T. et al., *Measurement of residual stresses in rails by neutron diffraction*, Wear, 2008, Vol. 265, 1402–1407.
[22] Schlenzer G., Fischer F.D., *Residual stress formation during the roller straightening of railway rails*, Int. J. of Mechanical Sciences, 2001, Vol. 43, 2281–2295.
[23] Skyttebol A., Josefson B.L., Rinsberg J.W., *Fatigue crack growth in a welded rail under the influence of residual stresses*, Engng Fracture Mechanics, 2005, Vol. 72, 271–285.
[24] Smith R.A., *Fatigue in transport. Problems, solutions and future threats*, Trans. IChemE: Part B, 1998, Vol. 76, 217–23.
[25] Steel R.K. et al., *Catastrophic Web Cracking of Railroad Rail: A Discussion of the Unanswered Questions*, Association of American Railroads, 1990.
[26] Telliskivi T., Olofsson U., *Wheel-rail wear simulation*, Wear, 2004, Vol. 257, 1145–1153.
[27] *The Derailment at Hatfield: A Final Report by the Independent Investigation Board (July 2006)*, UK. Office of Rail Regulation (ORR).
[28] Wang Y.Y., Chiang F.P., *Experimental study of three-dimensional residual stresses in rails by Moire interferometry and dissecting methods*, Optics and Lasers in Engng, 1996, Vol. 27, 89–100.
[29] Wrobel L.C., Aliabadi M.H., *The Boundary Element Method*, Wiley&Sons, 2002.
[30] Zerbst U., Lunden R., Edel K.-O., Smith R.A., *Introduction to the damage tolerance behavior of railway rails – a review*, Engng Fracture Mechanics, 2009, Vol. 76, 2563–2601.

TECHNICAL TRANSACTIONS | CZASOPISMO TECHNICZNE
CIVIL ENGINEERING | BUDOWNICTWO
6-B/2014

MAREK PIERCHAŁA*

PRACTICAL USES OF SOUND AURALIZATION IN CONFINED SPACES

PRAKTYCZNE ZASTOSOWANIA AURALIZACJI DŹWIĘKU W PRZESTRZENIACH ZAMKNIĘTYCH

A b s t r a c t

Practical aspects of testing confined spaces, especially for the purpose of acoustic adaptations, are presented. The tests were carried out with use of prediction models, showing the possibilities of models that are used at present. Sound auralization, which is a reliable method for the assessment of sound signal quality and the acoustic conditions of tested rooms, is described. The basic criteria for the assessment of acoustic conditions in confined spaces are briefly discussed.

Keywords: *acoustics*, *confined spaces*, *acoustic conditions*, *auralization*, *assessment indices*, *speech clarity*, *reverberation time*

S t r e s z c z e n i e

W artykule przedstawiono praktyczne aspekty badań przestrzeni zamkniętych, zwłaszcza na potrzeby realizacji adaptacji akustycznych. Badania te prowadzono z użyciem modeli predykcji, obrazując jednocześnie możliwości stosowanych obecnie modeli. Opisano auralizację dźwięku, która jest wiarygodną metodą oceny jakości sygnału dźwiękowego, a co za tym idzie, także i warunków akustycznych badanych pomieszczeń. Skrótowo omówiono podstawowe wskaźniki oceny warunków akustycznych w przestrzeniach zamkniętych.

Słowa kluczowe: *akustyka*, *przestrzenie zamknięte*, *warunki akustyczne*, *auralizacja*, *wskaźniki oceny*, *zrozumiałość mowy*, *czas pogłosu*

* Ph.D. Eng. Marek Pierchała, KOMAG Institute of Mining Technology.

1. Introduction

Sound auralization in a confined space is a term relating to the visualization of the distribution of sound intensity in a given testing area, which is frequently used in acoustic tests [8–10, 12, 13]. Auralization enables the audio monitoring of sound generated in a virtual room with the use of calculated methods for the prediction of impulse responses. Thus, it is possible to assess the acoustic conditions of closed rooms, which is especially important in tests carried out for the purposes of acoustic adaptation [12]. Acoustic adaptations enable changing audio conditions and most frequently, they aim to reduce reverberation times (RT) as well as improving speech transmission parameters and speech intelligibility parameters. However, auralization provides a subjective assessment of acoustic conditions, unlike the objective method based on the analysis of parameters [1–3, 8], which is discussed in detail in paragraph 2. Auralization, despite being subjective, enables speeding up the analyses and the additional verification of assessment with use of indicators. For the experienced listener, this method provides a variety of important information, giving the possibility of a reliable assessment of sound signal quality, and in many cases, it is more valuable than an assessment of parameters, because, for example, speech intelligibility is not a physical parameter, but only a measure of how the listeners understand the spoken words. The same applies with assessments of music transmission, assessments of music coding and assessments of audio equipment quality [8].

2. Sound auralization in a confined space – the recreation of acoustic conditions

Predictive tests were carried out in a virtual room for the purposes of acoustic adaptation aimed at improving acoustic conditions through limiting the RT. This room is presented in Fig. 1. This is a precise recreation of the material and geometrical design features of a real sports and entertainment hall. During the initial stage of testing, most frequent and periodically accepted functions of the analysed room were described in detail. This stage is very important from a testing point of view because it directly determines directions of procedures [6, 7]. Different guidelines regarding designing and tests are used for rooms only intended and for sport activities. Other guidelines are used for rooms where music is played as well as where celebrations, performances or training sessions take place [6, 7]. The functions of the rooms can be combined, however, this requires a different approach.

For almost 80% of the time, the tested room is used as a place for sport activities, while for the rest of the time, music is played there during rhythmic classes for children as well as verbal communiqués that are announced during different performances and celebrations. The method of announcing the verbal communiqués as well as the method of playing music is also important. The rooms in which the sound is emitted through audio system are designed without major difficulties. It is more difficult to cover with sound a large room, which is voiced only by a man. However, for some rooms it is necessary to take into account both forms of sound emission, i.e. audio systems and the human voice. The model presented in Fig. 1 was developed in a vector version with use of the standard Computer Aided Design (CAD) software program to an accuracy of 10 cm, and positions of all doors and window niches were recreated in this model as they are important with regard to the propagation of

audio waves [4]. The model was transformed to the Odeon acoustic software program and then completed with the material construction features. Acoustic calculations indicate that the tested room has a reverberation time that is too long with regard to the functions that were planned for this room. Such conditions are detrimental to health, people in this room get tired quickly and their concentration ability is reduced.

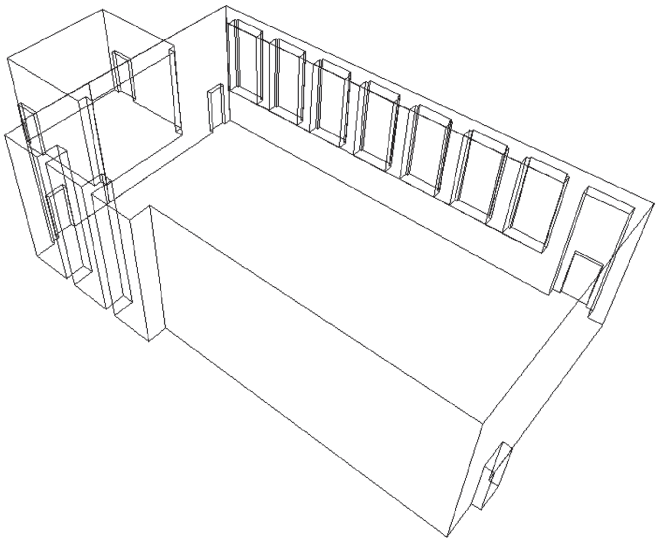

Fig. 1. Model of the geometry of the tested room [9]

Frequency	63	125	250	500	1000	2000	4000	8000
T Sabine	6,93	6,84	6,97	5,57	5,62	4,77	2,91	1,24
T Sabine (modified)	6,76	6,67	6,83	5,41	5,50	4,69	2,88	1,23
T Eyring	6,83	6,74	6,88	5,48	5,55	4,72	2,89	1,24
T Eyring (modified)	6,66	6,57	6,73	5,33	5,43	4,63	2,85	1,23
T Arau-Puchades	6,87	6,78	6,92	5,77	5,75	4,86	2,98	1,25
T Arau-Puchades (modifed)	6,72	6,64	6,81	5,71	5,71	4,84	2,97	1,25

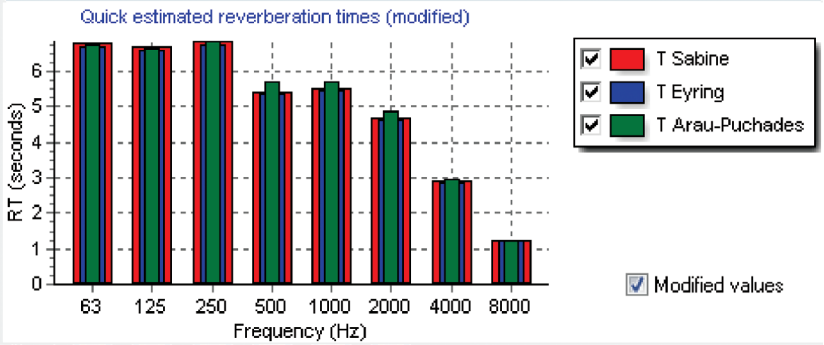

Fig. 2. Reverberation time in the room for the selected frequencies of middle octave bands [9]

Additionally, all parameters describing acoustic conditions of the room were analysed. Some of these parameters are indicated as follows [1, 3, 6–8, 12, 13]:

- reverberation parameters:
  - RT – reverberation time [s],
  - EDT – early decay time [s],
  - T15 – time of sound decay by 15 dB [s],
  - T20 – time of sound decay by 20 dB [s],
  - T30 – time of sound decay by 30 dB [s],
- speech intelligibility parameters:
  - STI – speech transmission index [–],
  - RASTI – rapid speech transmission index [–],
  - Al_{cons} – articulation loss of consonants [%],
- parameters associated with energy ratio:
  - D50 – distinctness index for 50 ms [dB],
  - C50 – clarity index for 50 ms (for speech) [dB],
  - C80 – clarity index for 80 ms (for music) [dB],
- spatial parameters:
  - LF80 – lateral flexion coefficient for 80 ms [–],
  - IACC – interaural cross-correlation coefficient [–],
- parameters determining the sound level:
  - SNR – signal to noise ratio [dB],
  - SPL – sound pressure level [dB].

Based on detailed assessment of the above parameters, the acoustic conditions inside the tested building were classified as either bad or very bad, depending on the type of assessment criterion. Unacceptable values of RT and EDT were the basic problem. These resulted from both the room geometry and from its layout (including material characteristics). The relatively low ceiling with its low absorption of acoustic wave energy was the reason for multiple unwanted wave reflections. As a consequence, speech intelligibility in almost all points of the room was abnormally low, while the STI did not exceed 0.1. Such difficult acoustic conditions required the development of assumptions for the improvement of these conditions through the adaptation of the most significant components of the interior decoration.

After the stage of objective assessment based on the parameters described above, the conclusions were additionally verified through the auralization of sound in the tested sports and entertainment hall. Sample audio material was listened to, and subjective impressions associated with listening to this material fully corresponded with the objective assessment based on the assessment criteria. Among other findings, it was found that the long reverberation time makes correct reception of voice messages impossible and the messages merge into a sequence of unintelligible sounds. This observation is reflected in the objective assessment of the RT, EDT and mainly STI, RASTI and Al_{cons} indices. A set of impulse responses for the receiving point P1 located at the centre of the hall at an appropriate height for signal reception in a sitting position, is given in Fig. 3 to image the auralization process.

Binaural Room Impulse Response (BRIR) – a set of two impulse responses determined for left and right auditory channels can be seen in the above figure. This method is very sensitive as it refers to sound pressure levels for a wide range of frequencies. Thus, changes

of acoustic pressure almost undetectable to human ears can be seen in the BRIR and seem to be significant [12, 13]. It should be emphasized that prediction models used at present are not ideal and even in the case of symmetry in the system: closed room, sound source, receiver, can give differences in BRIR for left and right auditory channel, what makes analyses difficult.

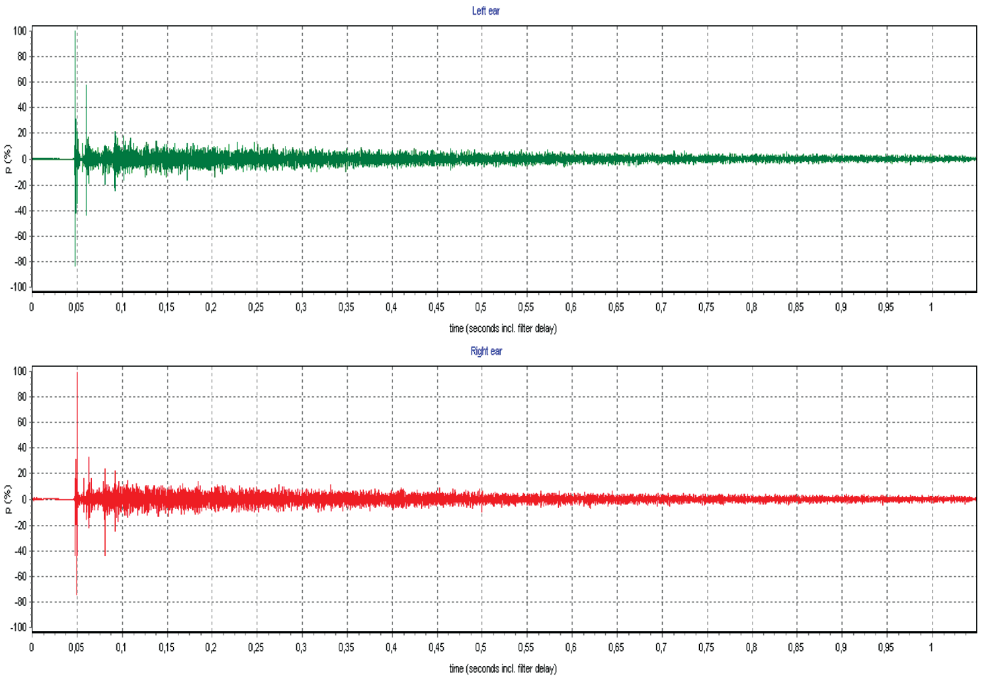

Fig. 3. Impulse response for left and right auditory channels determined in point P1 of the tested hall [9]

3. Acoustic adaptation and prediction of its results

Acoustic adaptation is understood as a series of activities undertaken to change acoustic conditions (mainly investments), to adapt them to the planned function of the room. The increase of acoustic absorption of the room by use of sound-absorbing materials is a typical acoustic adaptation procedure [9, 10]. Most frequently, these materials are placed below the ceiling, due to its dominating role in shaping the acoustic conditions of large rooms. Thus, material having the reverberant sound absorption coefficients described in Tab. 1 was used to improve the acoustic conditions of the analysed room (Fig. 1).

Table 1

Reverberant sound absorption coefficient of material used in acoustic adaptation

f [Hz]	63	125	250	500	1,000	2,000	4,000	8,000
α*p* [–]	0.10	0.55	0.90	1.00	0.90	0.95	0.75	0.10

The impact of adaptation on RT is presented in below figure (Fig. 4). It was found that after increasing the acoustic absorption, this time significantly decreased for almost all frequencies, excluding 63 Hz and 8 kHz for which the time decreased slightly.

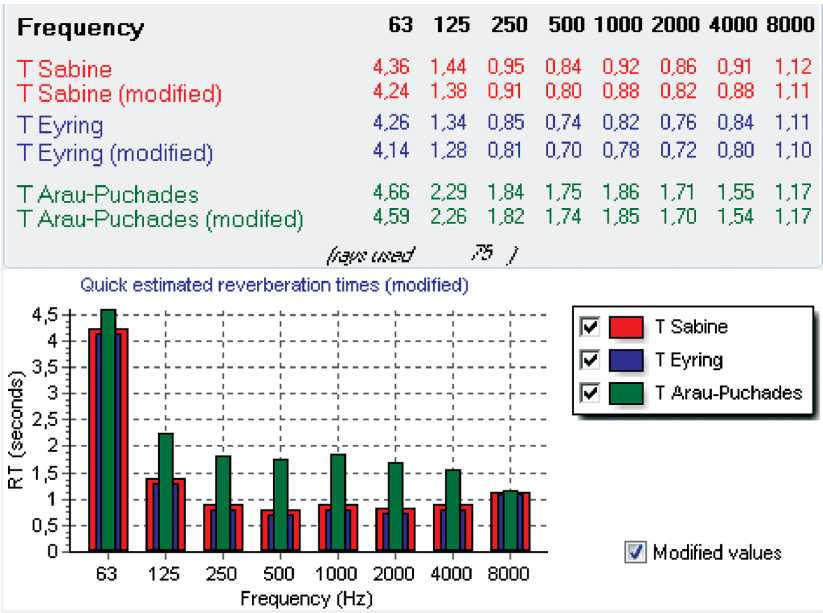

Frequency	63	125	250	500	1000	2000	4000	8000
T Sabine	4,36	1,44	0,95	0,84	0,92	0,86	0,91	1,12
T Sabine (modified)	4,24	1,38	0,91	0,80	0,88	0,82	0,88	1,11
T Eyring	4,26	1,34	0,85	0,74	0,82	0,76	0,84	1,11
T Eyring (modified)	4,14	1,28	0,81	0,70	0,78	0,72	0,80	1,10
T Arau-Puchades	4,66	2,29	1,84	1,75	1,86	1,71	1,55	1,17
T Arau-Puchades (modifed)	4,59	2,26	1,82	1,74	1,85	1,70	1,54	1,17

Fig. 4. Reverberation time of the tested room for selected frequencies of middle octave bands after acoustic adaptation [9]

EDT also significantly decreased as a result of adaptation. General STI increased to 0.61 for the speaker (audio system based only on human voice), including:

– 0.63 for speaking woman,
– 0.62 for speaking man.

Use of an adequate audio system would enable STI to increase to 0.68. It would improve the speech intelligibility in almost each point of the tested hall. It should be emphasized that STI at a level exceeding 0.6 refers to good acoustic conditions in the room regarding speech intelligibility. Al_{cons} also significantly increased to 6.98% – conditions classified as good according to the Peutz scale. As in the assessment of present state, also in the prognostic studies on acoustic adaptation, the sound auralization was made through a virtual listening to the sample sound material. It was found that speech intelligibility was significantly improved. Before acoustic adaptation, it was difficult to understand the sentences spoken by the lecturer and most of the words were unintelligible. However, after increasing the acoustic absorption of the room, and thus limiting the number of unwanted reflections of acoustic waves, the repeated speech became intelligible. Sound auralization enables the listener to use the percentage assessment of speech intelligibility [5, 11]:

$$Z = P/Q \cdot 100\%$$

where:

Z – speech intelligibility,
P – number of understandable words,
Q – number of all spoken words.

For such tests, it was assumed, according to the PN-EN ISO 9921:2005 Standard [11], that speech intelligibility is perfect when Z > 98 %, and it is sufficient when Z is in the range of 80% to 93%. Speech intelligibility is assessed as bad when 40% of all spoken words are not understood by the listener. For the analyzed example, the speech intelligibility is assessed as good. The impact of acoustic adaptation on hearing ability is also presented in a form of BRIR impulse responses in Fig. 5.

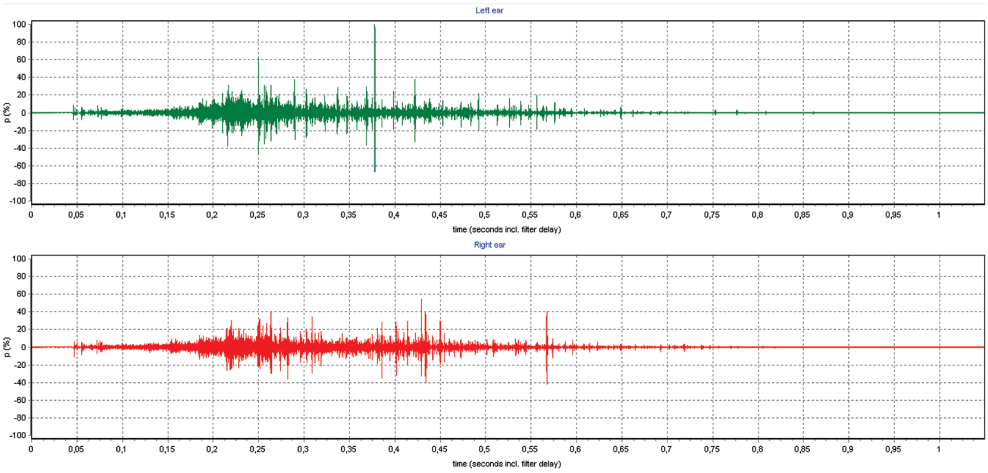

Fig. 5. Impulse response for left and right auditory channels determined at point P1 of the tested hall [9]

This response significantly differs from the response presented in Fig. 3 describing the condition before acoustic adaptation. The acoustic field was also identified during the tests regarding the acoustic system in the tested hall based on the human voice alone as well as on the human voice accompanied by an audio system. It was noticed that the use of an audio system ensures excellent sound coverage of the whole reception area with almost the same SPL indicator. Also on the stage, where speakers and vocal groups present themselves, the sound reception is correct and consistent with expectations. Much worse sound coverage occurs in situations, where in the tested hall the human voice is the only sound source. However, even in this case, acoustic conditions are acceptable.

The sequence of animation frames of acoustic wave propagation in the tested hall is presented in the figure below to show the possibilities of prediction models. The most representative images showing distribution of acoustic wave, only in the horizontal plane, were selected.

In Fig. 7, the acoustic wave coming directly from the source of sound was marked with ‘0’, while reflections of this acoustic wave were marked from ‘1’ to ‘12’ with colours according to

the figure legend. The animation shows the scale of the impact of changes to the room shape, caused by window and door niches and similar elements, on the distribution of acoustic waves. Reflections of acoustic waves generated by these elements have a significant impact on the acoustic field.

a)

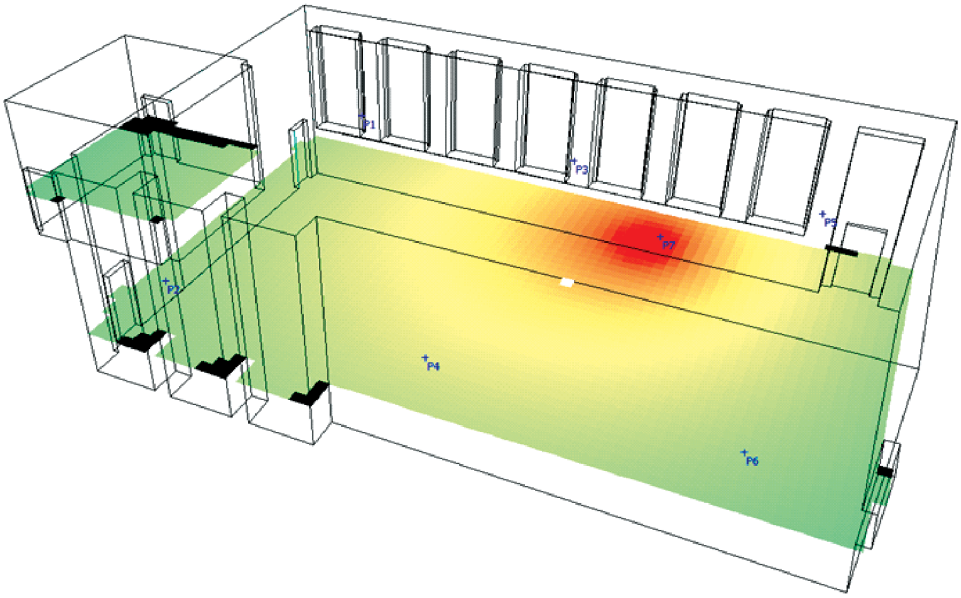

b)

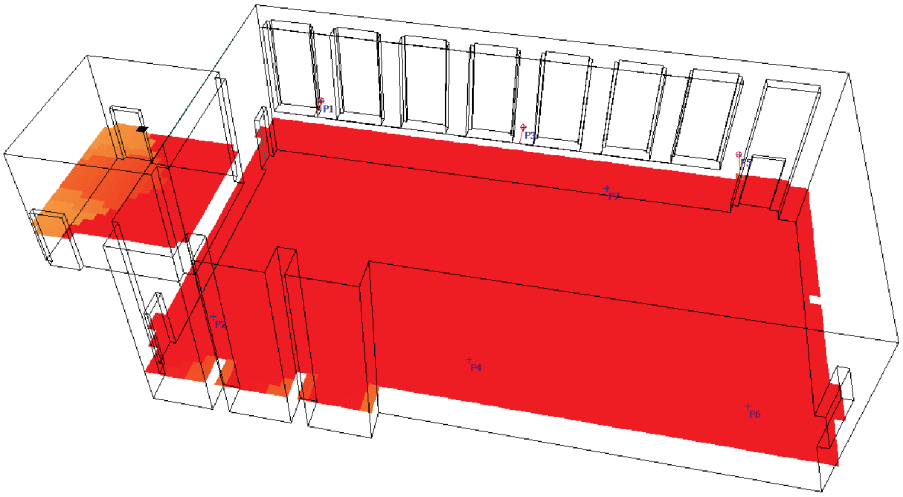

Fig. 6. Distribution of the acoustic field in the tested hall on the reception plane for the following acoustic system variants [9]: a) human voice, b) audio system

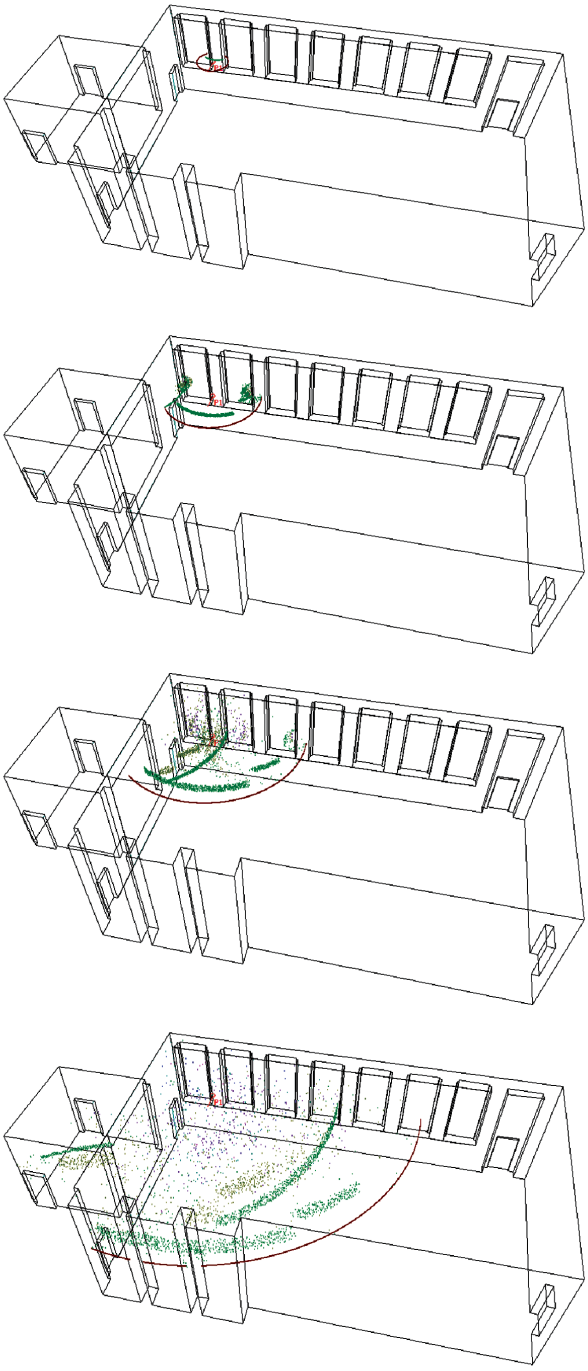

[0] [1] [2] [3] [4] [5] [6] [7] [8] [9] [10] [11] [>=12]

Fig. 7. Animation of acoustic wave distribution from one of the loudspeakers [9]

4. Summary

The tests of confined spaces are much more complex than other tests and analyses in acoustics. Such tests require a broad knowledge of room acoustics, and especially the ability to assess acoustic parameters. Sound auralization is an alternative method for such assessment. This method, despite its subjectivity, is highly valuable due to its assessment reliability. However, the development of numerical methods still introduces new tools enabling, among other things, the virtual tracking of propagation routes of single radius vectors of propagating waves, analyses of impulse responses (BRIR), and even animations of the propagation of acoustic waves. All these tools enable the precise assessment of the impact of changes in the room shape or material features of acoustic conditions of the tested rooms, enabling the design of more and more perfect interiors (i.e. interiors that fully realize their planned functions). The presented example shows that it is possible to change the acoustic conditions even for rooms with extremely unfavourable acoustic parameters regarding the functions planned for these rooms. The tests can be carried out not only to adapt the room for the planned functions, but also to analyse, for example, the listening conditions for the variant where human voice is the only sound source and for the variant where the audio system is used.

References

[1] Cremer L., Müller H.A., *Principles and Applications of Room Acoustics. Applied Science*, London 1982.

[2] Crocker M., *Handbook of noise and vibration control*, John Wiley & Sons Inc., New Jersey 2007.

[3] Engel Z., Engel J., Kosała K., Sadowski J., *Podstawy akustyki obiektów sakralnych*, ITE-PIB, Radom 2007.

[4] Gołaś A., *Metody komputerowe w akustyce wnętrz i środowisku*, AGH, Kraków 1995.

[5] Kotarbińska E., Kozłowski E., *Prognozowanie zrozumiałości mowy w hałasie podczas stosowania ochronników słuchu*, Bezpieczeństwo Pracy, 2004, nr 7–8, 16–20.

[6] Kulowski A., *Akustyka sal*, Wydawnictwo Politechniki Gdańskiej, Gdańsk 2007.

[7] Kulowski A., *Akustyka sal: zalecenia projektowe dla architektów*, Wydawnictwo Politechniki Gdańskiej, Gdańsk 2011.

[8] Long M., *Architectural Acoustics*, Elsevier Academic Press, USA 2006.

[9] Pierchała M., *Charakterystyka i ocena warunków akustycznych. Projekt instalacji systemu nagłośnienia. Analiza akustyczna W53.066LA. KOMAG*, Gliwice 2012 (not published).

[10] Pierchała M., Augustyn A., *Zastosowanie modelowania pól akustycznych w zwalczaniu ponadnormatywnej emisji dźwięku*, Masz. Gór., 2010, nr 3–4, 133–138.

[11] PN-EN ISO 9921:2005. Ergonomia. Ocena porozumiewania się mową.

[12] Rindel J., Christensen C., *Room acoustic simulation and auralization – how close can we get to the real room?*, Melbourne: WESPAC 8, The Eighth Western Pacific Acoustics Conference, 2003, 1–8.

[13] Rindel J., Christensen C., *Odeon, a design tool for noise control in indoor environments*, Lille, France, Solutions for Managing Occupational Noise Risk: Noise at work, 2007, 1–9.

TECHNICAL TRANSACTIONS | CZASOPISMO TECHNICZNE
CIVIL ENGINEERING | BUDOWNICTWO
6-B/2014

RAFAŁ SZYDŁOWSKI*, WOJCIECH KALISZ**

ANALYSIS OF THE FOUNDATIONS OF A FIVE-STOREY BUILDING ON EXTRUDED POLYSTYRENE

ANALIZA POSADOWIENIA PIĘCIOKONDYGNACYJNEGO BUDYNKU NA EKSTRUDOWANYM POLISTYRENIE

A b s t r a c t

This study presents the example of using extruded polystyrene for thermal insulation under the foundation slab of a building. Under the foundation slab of the thickness of 500 mm of a five-storey reinforced concrete building there was applied a layer of XPS of the thickness of 150 mm. The authors monitored the deformation of insulation under the load of the building from the moment of concreting the foundation slab until the completion of its development. Additionally, there were conducted laboratory tests of the σ–ε dependence and of material creeping. On the basis of the results of material properties, for the purpose of conducting the analysis of XPS deformations and effort, there was constructed a numerical model in the FEM system. This work includes the results of the conducted measurements and analyses with proper comments. They became the basis for drawing the conclusions which will be of use for future work.

Keywords: *extruded polystyrene*, *XPS*, *thermal isolation*, *concrete building*

S t r e s z c z e n i e

W pracy przedstawiono przykład zastosowania ekstrudowanego polistyrenu jako izolacji termicznej pod fundamentem budynku. Pod płytą fundamentową grubości 500 mm pięciokondygnacyjnego budynku żelbetowego zastosowano warstwę XPS o grubości 150 mm. Autorzy przeprowadzili monitoring odkształcenia warstwy izolacji pod obciążeniem budynkiem od momentu zabetonowania płyty fundamentowej aż do ukończenia jego realizacji. Dodatkowo przeprowadzono badania laboratoryjne zależności σ–ε oraz pełzania materiału. W oparciu o otrzymane rezultaty właściwości materiałowych w celu wykonania obliczeniowej analizy deformacji i wytężenia warstwy XPS zbudowano model numeryczny w systemie MES. W niniejszej pracy zamieszczono wyniki przeprowadzonych pomiarów i analiz ze stosownymi komentarzami, które mogą być przydatne w przyszłych realizacjach.

Słowa kluczowe: *polistyren ekstrudowany*, *XPS*, *izolacja termiczna*, *budynek żelbetowy*

* Ph.D. Eng. Rafał Szydłowski, IBMS, Faculty of Civil Engineering, Cracow University of Technology.
** M.Sc. Eng. Wojciech Kalisz, ICCE, Faculty of Civil Engineering, Cracow University of Technology.

1. Introduction

Horizontal thermal insulation has been generally used for the floors of the lowest levels of reinforced concrete buildings. It is traditional in the construction industry to place the structure of the building directly on load bearing soil. Then only the space between the highly loaded foundation elements (foundation bases, strip foundations) is thermally insulated from the soil with hard EPS. In modern construction also the foundation elements are insulated from the soil. Then slabs of extruded polystyrene are placed under the non-highly loaded strip foundations and foundation bases of low buildings, sports halls and others. Such a solution improves the heating properties of the building and has a positive effect on its energy balance. Thermal insulation under the foundations is especially significant in passive buildings. The foundation base then accumulates heat and gives it back only to the rooms, not to the soil. Currently the produced insulation material, i.e. XPS (extruded polystyrene) with high resistance to compression and low deformability, allows to develop more effective thermal insulation of a building from the soil than in the past.

For the first time the authors of this work used XPS as thermal insulation under the foundation slab of a five-storey reinforced concrete skeleton building. The XPS producers declare that its compression resistance to be the stress under specific deformation. That resistance is specified as per PN-EN 826 [1] on cubical samples of the side length of 50 mm. However, it is obvious that the size of the sample has effect on the mechanical properties of materials. Therefore, XPS may behave totally differently under a foundation slab than in a small sample. For that reason, there was conducted the monitoring of deformations of the XPS layer under the foundation slab of a designed and constructed building. The measurements were started after concreting the foundation slab and finished after the end of construction (after completing the internal and external finishing layers). Additionally, laboratory tests on XPS were conducted for the purpose of determining the stress-strain dependence under full admissible stress, and short stability of deformations at continuous stress.

2. XPS characteristics

XPS (extruded polystyrene) is a modern material for thermal insulations, formed in the shape of slabs in the process of extrusion and foaming of polystyrene resins. It is a fine-grain foam of low density. The endurance classes of 30, 50 and 70 refer to the guaranteed compressive stresses of 300, 500 and 700 kPa, respectively, under the imposed strain of 10%. The compressive strength at 10% strain is defined by the norm [1]. The suppliers of XPS additionally define the compressive stresses upon the strain of 2 and 5% and the elasticity modulus. The technical specifications also provide information on the creep specified as per PN-EN 1605 [2].

XPS is recommended by producers for insulation of external walls, horizontal insulation of floors, insulation of industrial flooring and parking lots, as insulation of strip foundations and others.

3. Structural description of the building and its insulation

The building of the Energy-Saving Construction Laboratory was developed from August 2013 to May 2014. The five-storey building was constructed of flat reinforced-concrete slabs of the thickness of 0.25 m, supported on columns. The slabs are based on 3 internal columns of the intersection dimensions of 0.35 × 0.35 m, on external columns and 3 stiffening walls (Fig. 1). Along the two external borders of the building, there were applied external columns of the intersection dimensions of 0.2 5× 0.25 m, with the filling of cellular concrete between them. Such walls were covered with the external layer of clinker bricks of the thickness of 0.12 m, based on brackets (Fig. 2a)). Along the two remaining external borders, there were applied the columns of the intersection dimensions of 0.30 × 0.30 m with glass facade.

The building was constructed on a foundation slab of the thickness of 0.50 m. The slab was thickened to 0.60 m in the areas of internal columns (Fig. 1b)). The layer of weak soil under the slab of the thickness of 1.0 m was replaced with load-bearing sand and gravel soil. Moreover, in the layer of the replaced soil there was additionally installed a horizontal heat exchanger. On the replaced substrate there was placed a layer of leca concrete of the thickness of 0.30 m. On the leca concrete, directly under the foundation slab, there was placed the thermal insulation layer of the thickness of 150 mm made of Polish slabs Synthos XPS Prime 70 (Fig. 1b)). The XPS slabs of the highest strength are produced at the thickness of up to 100 mm. For that reason, the layer of the thickness of 150 mm was produced by combining the slabs of the thickness of 50 and 100 mm (Fig. 2b)).

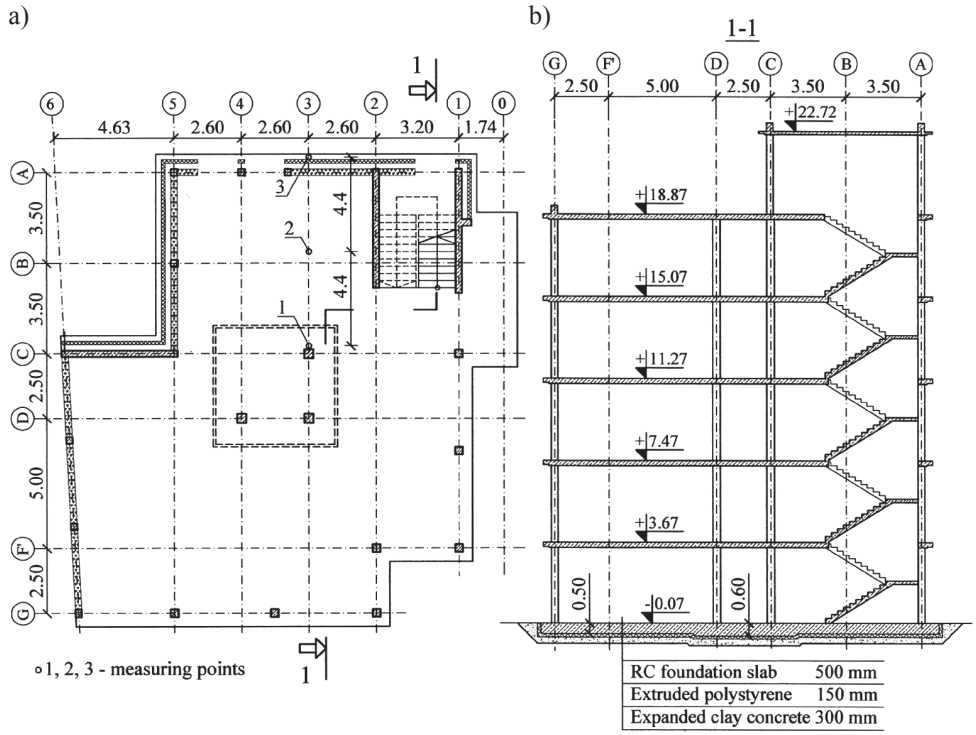

Fig. 1. a) Structural plan of the first floor, b) 1-1 vertical cross-section

a) b)

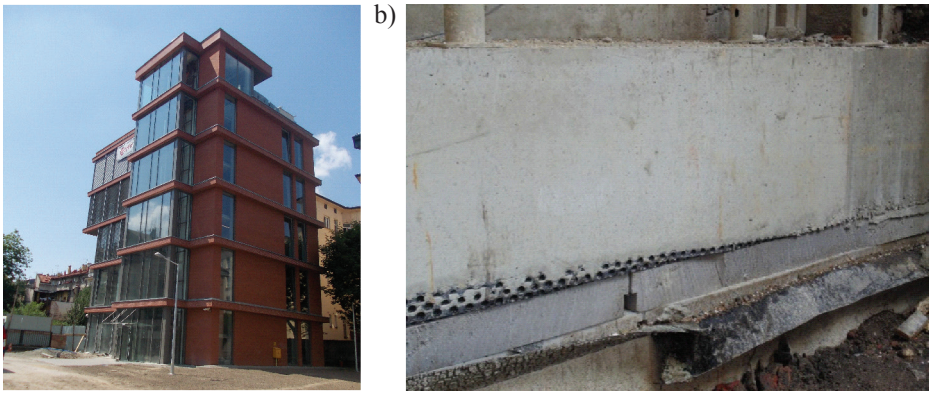

Fig. 2. a) The view of completed building, b) the view of XPS layer under the foundation slab

4. Tests program

The application of XPS under the foundation slab of such a tall building was a prototype solution in the authors' designing activities. For that reason, the decision was made to monitor the insulation material deformations under the load of the building. The purpose was to become familiar with the behavior of XPS at such a high load. Additionally, there were performed the laboratory tests on two samples of extruded polystyrene. The first one was used for determining the σ–ε dependence necessary for calibrating the FEM numerical model of the material. The second was used for determining the level of creep over a short period of time after application of load.

The tests were supplemented with the numerical analysis of the foundation slab together with substrate layers. All the tests were aimed at determining the limit of using XPS under the foundation elements in the buildings constructed in the future.

4.1. In-situ tests

Three measurements points were designated for the purpose of monitoring the insulation deformations (marked as 1, 2 and 3 in Figure 1a)). In those points there were installed ϕ10 mm threaded rods anchored in the substrate leca concrete (Fig. 3a)). The rods were insulated from the foundation slab concrete with a PVC pipe. The deformation of the XPS layer under the load of the building (that layer was situated between the leca concrete and the foundation slab) resulted in the rods moving out from under the foundation slab. That movement was registered with the mechanical sensors installed on the upper surface of the slab (Fig. 3b)). The measurement sensors were lined with steel boxes during the construction process, to protect them against damage. The only holes left were to allow the readouts. The first (zero) readout was performed right after concreting the foundation slab. The subsequent readouts were made no more often than every several days.

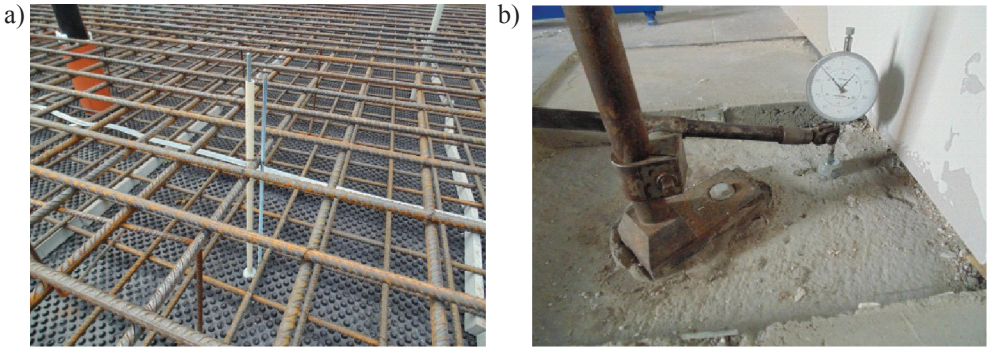

Fig. 3. a) The view of reference rood anchored into expanded clay concrete layer and b) mechanical gauge installed at the foundation slab surface

4.2. Laboratory tests

Two identical XPS samples were subject to tests in a laboratory. Those tests were aimed at improving the modeling of XPS behavior under the foundation slab. For that purpose, there were prepared 2 samples of the dimensions of 0.5 × 0.5 × 0.15 m. In order to limit the horizontal deformation of samples, they were placed in a special steel ring (Figs. 4 and 5). The clearance between XPS and the ring, of the thickness of 7–8 mm, was filled with cement mortar. In order to facilitate the vertical sliding of the material in the steel frame caused by its vertical deformation between the mortar and the XPS sample, there were applied 2 layers of PE foil. The details of the prepared sample were presented in Fig. 4, while its view – in Fig. 5. The steel slab generating the load was 500 × 500 mm in size. It was 4–6 mm smaller than the XPS sample.

The first sample was used to test the σ–ε dependence. The load was applied with continuous increase in the XPS thickness loss of 0.5 mm per minute, until gaining the highest load capacity of the material.

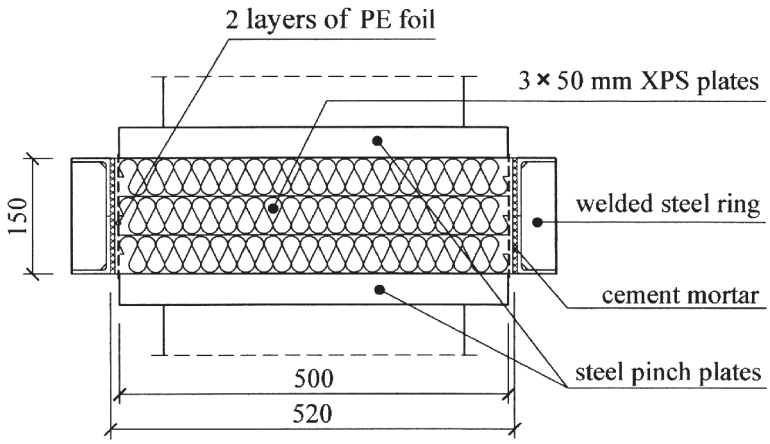

Fig. 4. The samples of Synthos XPS 70 prime inside the steel ring

The second sample was used for testing the stability of deformation (creep) at stable loads (increased gradually). The first load was 200 kPa. During the test, the stress was increased in 100 kPa increments. Each value of the stress was maintained until the moment when the deformations stabilized (stabilization of deformations was assumed to be the loss in thickness over time smaller than 0.01 mm over 5 minutes).

Fig. 5. The view of sample prepared to test

4.3. Numerical analysis

There was constructed a numerical model of the foundation slab together with a polystyrene layer in the FEM system. The ABAQUS software was used for that purpose. The numerical model was constructed based on three-dimensional finite elements. The analysis assumed elastic substrate and friction between the slab and XPS.

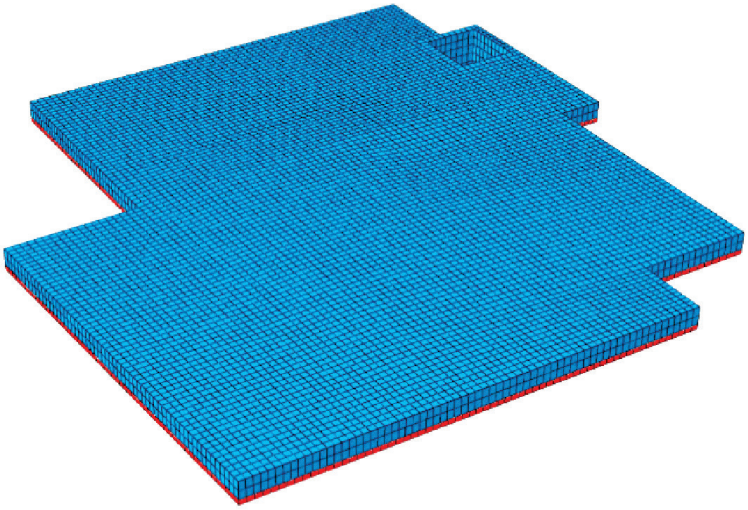

Fig. 6. FEM model of foundation slab and insulation layer

A contact layer was applied in order to provide the physical conditions of contact between the two materials. That meant absence of zero or negative values of substitute forces in contact surface nodes. It is necessary to provide the condition of contact and the geometrical compliance of the adjacent elements (the shape function must be continuous on the contact of those elements). For that reason, the C3D8R finite elements were used for all the parts of the model. These are 8-node elements with linear shape function and reduced contact points. Those elements are available in the ABAQUS/Standard library. The friction coefficient was assumed as $\mu = 0{,}3$. The constructed FEM model was presented in Fig. 6.

The numerical analysis was conducted in 6 steps. Each step was consistent with the suitable stage of the construction of the building. The load was applied in the form of concentrated forces from columns and linear load from the walls. There was assumed the elastic work of the foundation slab with the parameters $E = 32$ GPa and $\nu = 0.3$ consistent with the concrete of class C25/30. XPS was modeled as an elasto-plastic material. The elasto-plastic model in the ABAQUS program required the separation of the elastic and inelastic elements [3]. In the most general form, that compound may be presented as:

$$F = F^{el} \cdot F^{pl} \tag{1}$$

where F is the total deformation gradient, F^{el} is a fully reversible part of deformation in the considered point, and F^{pl} is defined as:

$$F^{pl} = \left[F^{el}\right]^{-1} \cdot F \tag{2}$$

The above division of elements may be directly used in formulating the plastic model. The XPS material model, constructed based on von Mises yield surface, was used for conducting a numerical analysis. The properties of the XPS material were assumed based on the $\sigma-\varepsilon$ dependence received from laboratory tests (Fig. 8). To define the material properties it is necessary to know the Cauchy stresses and the logarithmic deformations. In this case of results of laboratory tests, there were known the dependence between nominal stress and strain. For the purpose of obtaining the actual stresses and logarithmic deformations, there was a simple conversion:

$$\sigma_{true} = \sigma_{nom}\left(1 + \varepsilon_{nom}\right) \tag{3}$$

$$\varepsilon_{\ln}^{pl} = \ln\left(1 + \varepsilon_{nom}\right) - \frac{\sigma_{true}}{E} \tag{4}$$

5. Tests results

Figure 7 presents the results of reducing the thickness of thermal insulation under the foundation slab registered in 3 measurement points marked in Fig. 1a). Two characteristic points were marked on the time axis. These are the time of completing the construction of the reinforced concrete structure (16 November 2013) and the time of completion of the finishing layers, such as the cement leveling, filling walls, glass and clinker lining (5 March 2014) which time was crucial for the load for the foundation slab. What may be observed that the change in insulation thickness is different in different points. The closer we are to the external edge, the higher the value is.

Figure 8 presents the σ–ε dependence obtained in the laboratory tests. A non-linear dependence may be observed in the whole scope of loads. The highest compressive stresses amounted to 664 kPa and were recorded at the strain equal to 4.57%. They were maintained until the deformations reached the level of 5.2%, after which they began to fall.

The stresses were maintained until the strain reached the level of 10%, but the high speed of creep did not allow to record the stresses with required precision.

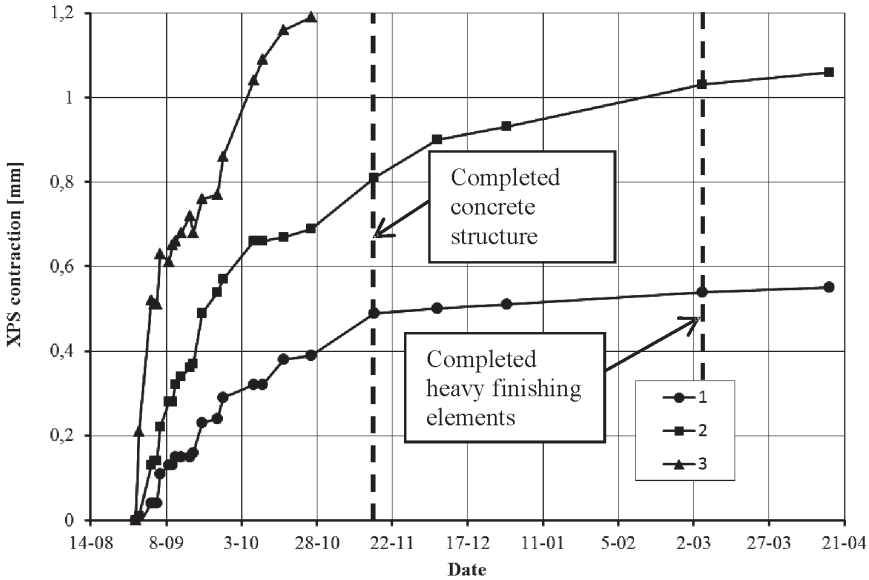

Fig. 7. Results of XPS layer thickness reduction in 3 measurements points marked in Fig. 1a)

The curve in Fig. 8 presents the high value of the secant elastic modulus. It amounted to 62.5 MPa at the stresses equal to 200 kPa; 48.5 MPa at 300 kPa and 40.1 MPa at 400 kPa. It should be noted that the average value of the elastic modulus amounts to 25 MPa in the declaration of the producer of XPS.

Figure 9 presents the results of the laboratory tests of short-term XPS creep. The upper diagram shows the load program, while the lower diagram – the change in strain over time. The horizontal markers on the strain curve signify the end of increasing the stresses in the respective steps (beginning of creep). The assumed criterion for stabilization of deformations over time was described in point 4.2. At the stresses equal to 200 kPa, the deformation stabilization over time lasted about 1 hour. Over that time the deformations increased by 4.4%. The same values amounted respectively to 1 hour and 9.1% at the stresses of 300 kPa and 2.6 hours and 28.7% at 400 kPa. The stresses of the value of 500 kPa were maintained for over 4 hours. The deformations over that time increased from the value of 0.0234 to 0.0364. Therefore, the increase was 37.9%, but it was far from stabilizing the deformations. What should be emphasized is that the deformations were approaching the value of 4.57% fast. It is the value at which the highest load-bearing capacity of XPS was reached in the tests of the σ–ε dependence.

The maps of lowering the insulation thickness obtained from the numerical analysis were presented in Fig. 10. The vertical stresses in the XPS layer are presented in Fig. 11.

The highest value of the stresses under the internal thickened fragment of the foundation slab amounted to 82 kPa. The highest local values of stresses amounted to 180 kPa in the area of the staircase and 196 kPa under the external wall. Figure 12 presents the results of the calculated change in thickness in the measurement points marked in Fig. 1a). Those values were designated in 6 analysis steps, after concreting each floor and after completing the construction of the building. The results were compared with the measured values. It may be noted that only point "1" recorded the satisfactory compliance of less than 20%. It may result from the fact that the loads were not estimated precisely enough and that the creep in the numerical analysis was neglected. The presented comparison between the results shows the necessity to improve the modeling of that issue.

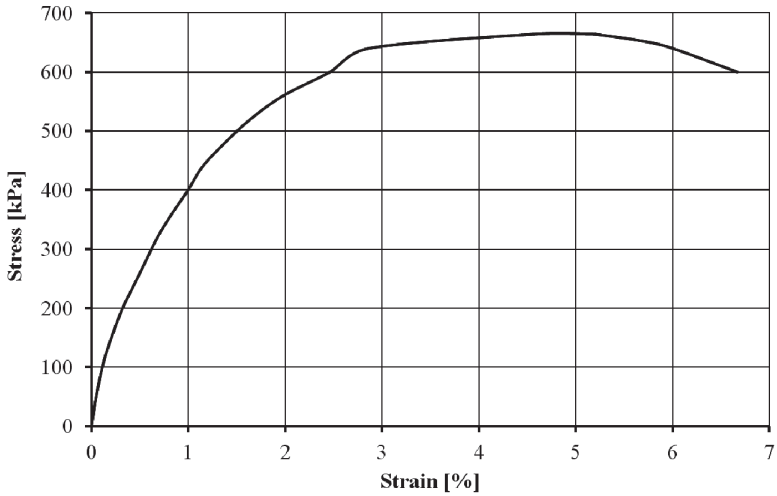

Fig. 8. Stress-strain dependence from laboratory test

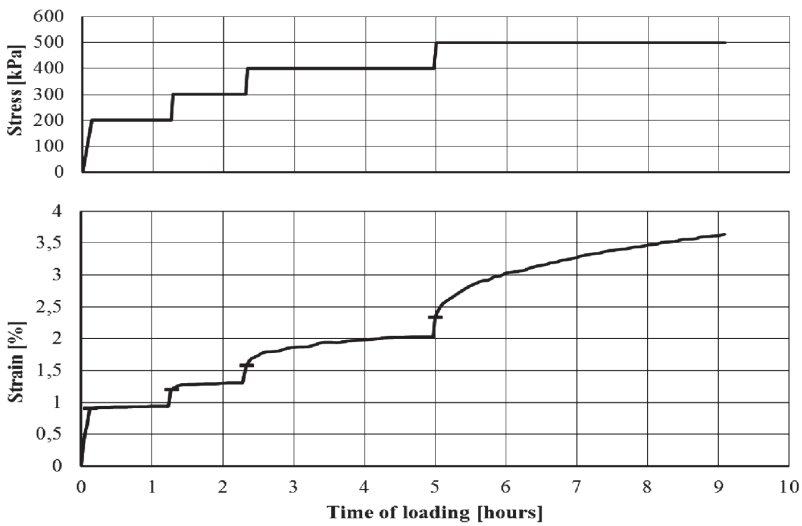

Fig. 9. Short time creep of XPS sample from laboratory test

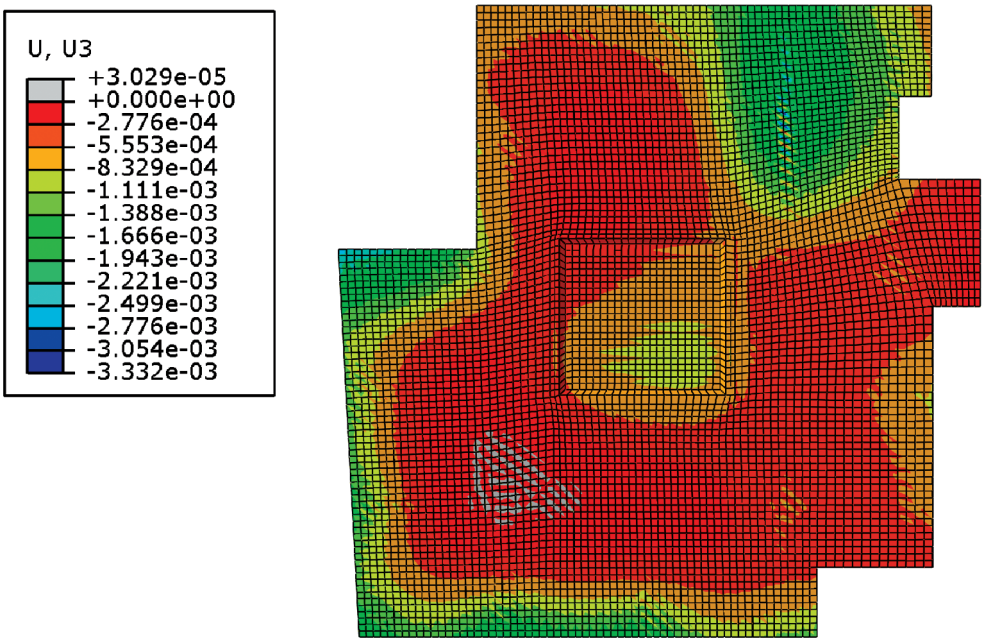

Fig. 10. The map of vertical contraction of XPS layer in final stage [in meter]

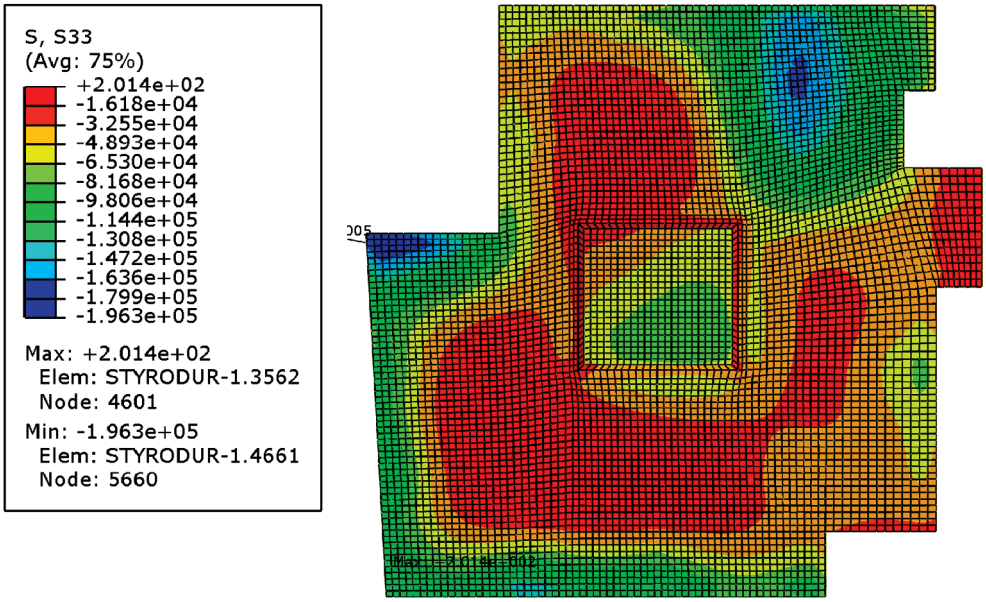

Fig. 11. The map of vertical stresses in XPS [in Pa]

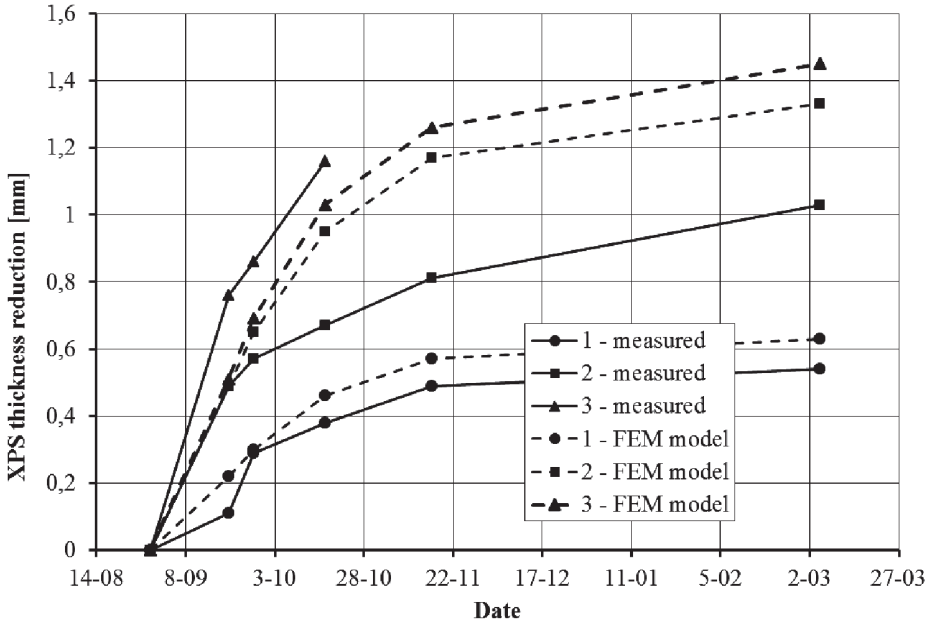

Fig. 12. Results of XPS thickness reduction (calculated and measured)

6. Final conclusions

On the basis of the obtained analysis and measurement results it may be concluded that:

- The change in the thickness of the 150 mm layer of XPS under the foundation slab of the five-storey reinforced concrete building exceeded slightly 1 mm (1.19 mm; $\varepsilon = 0.79\%$ – point "3"). That value was reached at the stresses equal to 115 kPa (value from numerical calculations). Such a small change in insulation thickness is not significant for the total settlement of the building.
- The laboratory tests of creep of XPS indicated that the deformations stabilize at the stresses of 400 kPa. That value seems too high to allow it when applying insulation under a building without additional creep tests over a long period of time. However, it may be determined that the safe level of stresses is the value of 300 kPa.
- The above conclusions indicate that it may be assumed that it would be safe to apply the analyzed XPS material under the foundations of a 10-storey building.
- However, it is certain that the modeling of the issue presented in this work should be improved. For that purpose, a plastic soil model should be applied. Additionally, it is necessary to prepare the model of the whole building in order to take into account the impact of stiffness of the building on the behavior of the foundation slab.

Literature

[1] PN-EN 826: 2013-07 *Thermal insulating products for building applications – Determination of compression behavior*, 30-07-2013.
[2] PN-EN 1605: 2013-07E *Thermal insulating products for building applications – Determination of deformation under a given compressive load under specified temperature* (in Polish), 30-07-2013.
[3] *ABAQUS User's Manual*, 2011.
[4] Synthos XPS Prime 70 (I, L, N), *Technical Manual*, Synthos S.A., July 2013.

TECHNICAL TRANSACTIONS | CZASOPISMO TECHNICZNE
CIVIL ENGINEERING | BUDOWNICTWO
6-B/2014

TERESA ZYCH*

TEST METHODS OF CONCRETE RESISTANCE TO CHLORIDE INGRESS

METODY BADANIA ODPORNOŚCI BETONU NA WNIKANIE CHLORKÓW

Abstract

The experimental methods for determination of concrete resistance to chlorides – both the chloride permeability test methods (NT Build 492 NordTest – Non-Steady State Migration Test, AASHTO T 277-ASTM C 1202 Test) and the methods for testing concrete resistance to surface scaling due to cyclic freezing and thawing in the presence of NaCl solution (deicing salts, saline sea water, etc.) (e.g. Slab Test according to CEN/TS 12390-9, based on the Borås method according to Swedish Standard SS 13 72 44) are presented in the paper. The Rapid Chloride Test – the method used "in situ" to determine the chloride ion content in concrete is also described.

Keywords: *concrete durability*, *exposure classes (XD, XS, XF)*, *chloride diffusion*, *scaling resistance*

Streszczenie

W artykule przedstawiono doświadczalne metody określenia odporności betonu na działanie chlorków – metody badania przepuszczalności chlorków (NT Build 492 NortTest – Test migracji chlorków przy nieustalonym przepływie, AASHTO T 277-ASTM C 1202 Test) oraz metody badania odporności betonu na powierzchniowe łuszczenie spowodowane cyklicznym zamrażaniem i odmrażaniem w obecności roztworu NaCl (soli odladzających, słonej wody morskiej itd.) (np. Slab Test według normy CEN/TS 12390-9, wzorowany na metodzie Borås według szwedzkiej normy SS 13 72 44). Opisano również Rapid Chloride Test – metodę „in situ" badania zawartości jonów chlorkowych w betonie.

Słowa kluczowe: *trwałość betonu*, *klasy ekspozycji (XD, XS, XF)*, *dyfuzja chlorków*, *odporność na powierzchniowe łuszczenie*

* Ph.D. Teresa Zych, Institute of Building Materials and Structures, Faculty of Civil Engineering, Cracow University of Technology.

1. Introduction

Concrete exposed to various environmental conditions can be penetrated by many aggressive ions. Chloride ions affect the durability of concrete subjected to the action of sea water, chloride-bearing air in marine areas and de-icing salts. The penetration of chloride ions can cause corrosion of concrete and corrosion of rebars embedded in concrete.

Corrosion of concrete is caused by the expansive products obtained in the reaction of chloride ions with the components of concrete (mainly calcium hydroxide $Ca(OH)_2$), e.g. expansive alkaline calcium chloride $Ca(OH)_2 \cdot H_2O \cdot CaCl_2$, which increases its volume during crystallization and causes destruction of concrete, is formed during the following reactions:

$$Ca(OH)_2 + 2NaCl \rightarrow CaCl_2 + 2NaOH \tag{1}$$

$$Ca(OH)_2 + CaCl_2 + H_2O \rightarrow Ca(OH)_2 \cdot H_2O \cdot CaCl_2 \tag{2}$$

Chlorides also affect corrosion of steel reinforcement. Chloride ions, CO_2, etc. destroy the protective ferric oxide film which is stable in alkaline (high pH) environment around the steel rebar. This depassivation induces corrosion of steel (lack of the passive layer on the surface of reinforcement leads to the reaction of chloride ions Cl^- with iron, which results in ferric chloride $FeCl_2$; then $FeCl_2$ reacts with water to form rust $Fe(OH)_2$ and the resulting hydrochloric acid HCl causes formation of pits on the surface of reinforcing bars [17, 19]:

$$Fe + 2Cl^- \rightarrow FeCl_2 + 2e^- \tag{3}$$

$$FeCl_2 + 2H_2O \rightarrow Fe(OH)_2 + HCl \tag{4}$$

Corrosion of steel reinforcement causes its expansion in volume due to corrosion products and subsequent cracking and spalling of concrete from the reinforcement.

Moreover, chloride ions (from de-icing salts) together with frost attack can cause another form of concrete deterioration – concrete scaling [7, 17, 19].

The threat of corrosion from chlorides is addressed in the European standard EN 206-1 [35] under two sets of exposure classes: chlorides from sea water (XS) and chlorides other than from sea water (XD). Exposure class XS1 covers concrete that is exposed to airborne salts from sea water but not in direct contact with sea water. The examples of such structures are those situated along the coast beyond the spray zone. Exposure class XS2 includes concrete that is permanently submerged in sea water, i.e. marine and coastal structures. This concrete may be subjected to considerable chloride penetration but significant corrosion may not occur due to the low level of oxygen supply. Exposure class XS3 means that concrete is in the tidal, splash and spray zones. The examples of structures exposed to these conditions include marine and coastal structures. Exposure class XD1 includes the case of concrete of moderate humidity and in contact with airborne chlorides from sources other than sea water, e.g. structures in proximity to highways. Exposure class XD2 covers concrete that is wet, rarely dry, in contact with water containing chlorides other than from sea water. The examples of such structures are swimming pools or structures exposed to industrial waters containing chlorides. Exposure class XD3 means that concrete is exposed to cyclically wet and dry

environment and chlorides are not from sea water. The examples of structures are pavements, car park slabs, parts of bridges, highways subjected to de-icing salts or spray from water containing de-icing salts.

The action of chlorides (de-icing agents) together with the freeze-thaw attack is classified in EN 206-1 [35] as: XF2 exposure class when concrete is moderate water saturated, XF4 exposure class in the case of high water saturated concrete. The examples of such structures are pavements, road and marine structures [4, 7, 13, 19, 29].

The problem of concrete resistance to chloride ingress occurs in many various structures. The chloride resistance is one of the most important properties of concrete in the design, construction and maintenance of structures. The paper presents the test methods used for determining the chloride permeability of concrete, chloride content in concrete and concrete scaling caused by frost and de-icing salts. It is also an attempt at a comparative analysis of the afore-mentioned test methods.

2. Chloride permeability of concrete – Standard test methods

The most common methods used to determine the resistance of concrete to the penetration of chloride ions (the chloride diffusion coefficients) are two methods: the **NordTest** – the **Rapid Chloride Migration Test** (RMT), described in the Scandinavian standard **NT Build 492** [39], which is very popular in Europe and the **Rapid Chloride Permeability Test** (RCPT), presented in two American standards **ASTM C 1202** [33] and **AASHTO T 277** [31], which is widespread in the USA and Canada.

In both methods, the penetration of chloride ions is exerted by an external electrical field. The transport processes that take place during the tests are **diffusion** and **electromigration**. Diffusion, which is the transfer of ions from the region of higher ion concentration to the region of lower ion concentration, is the principal chloride ion transport mechanism from the external environment into concrete [13]. Electromigration is caused by the applied voltage. The electrical field is used to accelerate the transfer of chloride ions [8, 18].

In both tests, cylinders with the dimensions of **100 mm (diameter) × 50 mm (thickness)** are used as concrete specimens. The major **differences** between the two methods are the concentration of **NaCl** solution (**3%** in the Rapid Chloride Migration Test /RMT/ versus **10%** in the Rapid Chloride Permeability Test /RCPT/), the voltage used across the electrodes (**30 V** in RMT versus **60 V** in RCPT) and the test duration (from 6 to 96 hours, usually **24 hours** in RMT versus **6 hours** in RCPT).

The RMT and RCPT tests are **non-steady state** tests (in reality, chloride penetration into concrete is a non-steady-state process [8, 18, 23]). The rapid non-steady-state tests are popular, in contrast to the steady-state tests.

Tests for measuring steady-state flux of chlorides are described in the literature [18, 19, 21, 23]. Steady-state tests are very time consuming (it takes several months or even several years to obtain the steady-state chloride flow /diffusion/ across the specimen). The common procedure is the diffusion cell test method (Fig. 1) [18, 21].

In this method a thin specimen forms a barrier between an ion source solution and another solution free of the ions. This allows ions to diffuse in a concentration gradient. When steady-state conditions are achieved, the diffusion coefficient is calculated (using

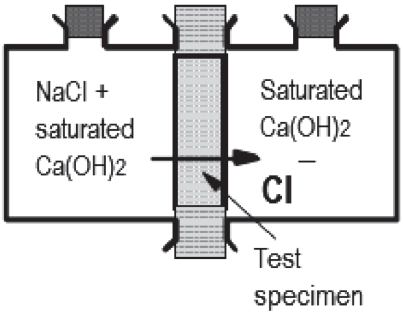

Fig. 1. Test of the chloride resistance of concrete – The steady-state test method. A typical ion diffusion cell [18]

the Fick's First Law of diffusion). Certain migration cell methods in which an electric field is applied to a concrete specimen have been developed in recent years. However, it is difficult to evaluate the diffusion coefficient since all the ions involved in the test affect the flux of chloride ions.

2.1. NT Build 492 (NordTest) method

NT Build 492 (NordTest) – Non-Steady State Migration Test [39], also known as the Rapid Chloride Migration Test (RMT), proposed initially by **Tang and Nilsson** (in 1991) [26, 28] is a very simple and reliable test. The test can be use for **different types of concrete**. To determine the chloride migration coefficient under non-steady state, the depth of chloride penetration in concrete is measured [11, 13, 15, 18, 27]. The concrete specimen (**$Ca(OH)_2$ saturated**) is subjected to the external electrical voltage and chloride ions are forced to move into concrete (Fig. 2). Due to the potential difference between the electrodes, chloride ions migrate from the **10% NaCl solution**, through the concrete specimen, towards the **0.3 M NaOH solution** (Fig. 3), for a defined period of time. Afterwards, the specimen is split and sprayed with $AgNO_3$ – an indicator for chlorides – and thus the chloride penetration depth is measured (Fig. 4). The chloride migration coefficient is calculated on the basis of the value obtained by the measurement.

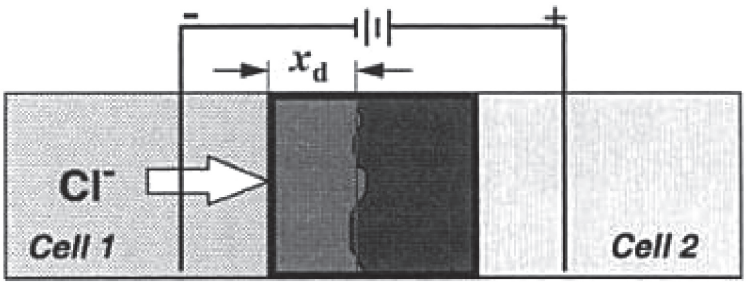

Fig. 2. Test of the chloride resistance of concrete – Schematic diagram of the NT Build 492 (NordTest) method [27]

The method is applicable to the specimens cast in a laboratory or drilled from field structures. The method requires cylindrical specimens with a diameter of 100 mm and thickness of 50 mm, sliced from cast cylinders or drilled cores with a minimum length of 100 mm (e.g. if a Ø100 × 100 mm cast cylinder is used, a 50 mm thick slice should be cut from the central portion of the cylinder; the preparation of the test specimen in the case of longer cast cylinders and drilled cores is described in the standard). Three specimens should be used in the test. After sawing, washing, drying and the vacuum treatment (10–50 mbar /1–5 kPa/ for three hours), the specimens are **saturated with $Ca(OH)_2$** for 19 hours (one hour with the maintained steady vacuum level and subsequently 18 hours after turning off the pump). The saturated concrete sample is set in the test apparatus as shown in Fig. 3.

The catholyte and anolyte reservoirs are filled with the solutions. The catholyte solution is **10% NaCl** solution (100 g NaCl in 900 g distilled or de-ionised water, about 2 N) and the anolyte solution is **0.3 N NaOH** solution (approximately 12 g NaOH in 1 litre water). Thus, the solution on one side of the sample contains chloride ions, while the other solution is chloride free. The electrical potential (**30 V** DC) is applied and the chloride ions are driven into concrete. The initial current is measured. Based on the **initial current**, the **test voltage** and the **test duration** should be selected (as shown in Tab. 1). For example, if the initial current is between 120 and 180 mA, the test voltage is reduced to 15 V DC and the test duration is 24 hours [23, 39].

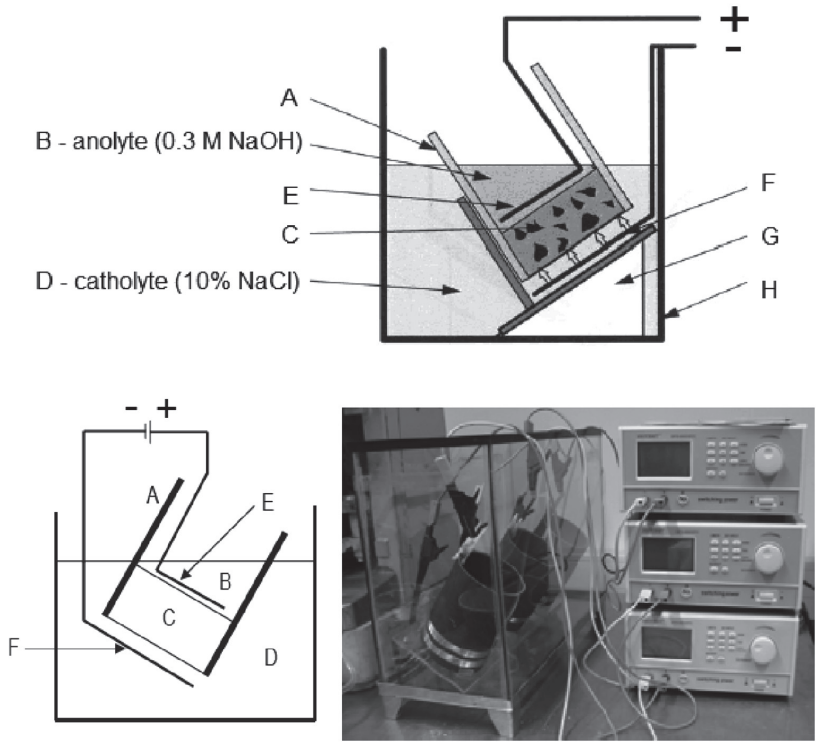

Fig. 3. Test of the chloride resistance of concrete – the NT Build 492 (NordTest) method. Test set-up: A – silicone rubber sleeve, B – anolyte (0.3 M NaOH), C – concrete sample, D – catholyte (10% NaCl), E – anode, F – cathode, G – plastic support, H – plastic box [2, 22, 23]

Table 1

NT Build 492 (NordTest) method – Test voltage and duration [39]

Initial current I_{30V} (with 30 V) [mA]	Applied voltage U (after adjustment) [V]	Possible new initial current I_0 [mA]	Test duration t [hour]
$I_0 < 5$	60	$I_0 < 10$	96
$5 \le I_0 < 10$		$10 \le I_0 < 20$	48
$10 \le I_0 < 15$		$20 \le I_0 < 30$	24
$15 \le I_0 < 20$	50	$25 \le I_0 < 35$	
$20 \le I_0 < 30$	40	$25 \le I_0 < 40$	
$30 \le I_0 < 40$	35	$35 \le I_0 < 50$	
$40 \le I_0 < 60$	30	$40 \le I_0 < 60$	
$60 \le I_0 < 90$	25	$50 \le I_0 < 75$	
$90 \le I_0 < 120$	20	$60 \le I_0 < 80$	
$120 \le I_0 < 180$	15	$60 \le I_0 < 90$	
$180 \le I_0 < 360$	10	$60 \le I_0 < 120$	
$I_0 \ge 360$		$I_0 \ge 120$	6

After a specified period of time the sample is removed and then it is split (in 10-mm thick slices) (see Fig. 4) and sprayed with 0.1 N **$AgNO_3$ (silver nitrate) solution**. When $AgNO_3$ solution is sprayed on concrete containing chloride ions, a chemical reaction occurs. $AgNO_3$ converts to AgCl (silver chloride), a whitish substance ($Ag^+ + Cl^- \rightarrow$ **AgCl /white/**). In the non-chloride area the silver binds with hydroxides present in concrete, creating a brownish colour ($Ag^+ + OH^- \rightarrow AgOH \rightarrow Ag_2O$ /brown/). The chloride penetration depth is measured on the basis of the **white AgCl precipitation** (clearly visible after about 15 minutes) (Fig. 4) [12, 13].

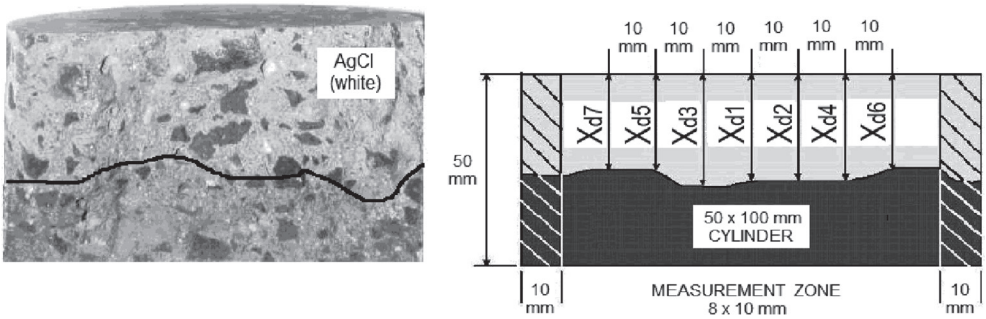

Fig. 4. Test of the chloride resistance of concrete – the NT Build 492 (NordTest) method. Measurement of chloride penetration depths [2, 23, 39]

A quick and easy method of spraying $AgNO_3$ (silver nitrate) on a cross-section of split concrete to identify the **depth of chloride penetration** into a specimen is called

the **colourimetric method** (technique) (in which $AgNO_3$ is used as a colourimetic indicator) [3, 12, 22]. The penetration depths should be measured (to an accuracy of 0.1 mm) in the concrete sample starting from the centre towards both edges at intervals of 10 mm (Fig. 4) (using a slide caliper or a suitable ruler). No measurements should be made in the zone within about 10 mm from the edge to obviate the edge effect due to a non-homogeneous degree of saturation or possible leakage [12]. An average of the seven measurements is used for determining the **non-steady-state chloride migration coefficient** (also known as the chloride diffusion coefficient) $\boldsymbol{D_{nssm}}$. The coefficient is calculated on the basis of the voltage magnitude, temperature of anolyte measured at the beginning and the end of test and the depth of penetration of chloride ions, using Eq. (6), obtained from Eq. (5) [2, 28, 39].

$$D_{nssm} = \frac{RT}{zFE} \frac{x_d - \alpha\sqrt{x_d}}{t} \tag{5}$$

$$E = \frac{U-2}{L}, \quad \alpha = 2\sqrt{\frac{RT}{zFE}}\, erf^{-1}\left[1 - \left(2\, C_d / C_0\right)\right]$$

where:

- D_{nssm} – non-steady-state chloride migration coefficient [m²/s],
- R – gas constant, $R = 8.314$ [J/(°K mol)],
- T – average value of the initial and final temperatures in the anolyte solution [K],
- z – absolute value of ion valence, for chloride ions $z = 1$,
- F – Faraday constant, $F = 9.648 \times 10^4$ [J/(V mol)],
- E – electric field [V/m],
- U – absolute value of the applied voltage (potential difference across the specimen) [V],
- L – thickness of the specimen [m],
- x_d – average value of the penetration depths [m],
- α – laboratory constant [$m^{1/2}$],
- t – test duration [s],
- erf^{-1} – inverse of error function,
- C_d – chloride concentration at which the colour changes, $C_d = 0.07$ N for Portland cement concrete [mol/dm³],
- C_0 – chloride concentration in the catholyte solution, $C_0 = 2$ N [mol/dm³].

Since $erf^{-1}\left[1 - \left(2 \times 0.07 / 2\right)\right] = 1.28$, the equation is simplified to

$$D_{nssm} = \frac{0.0239\,(273+T)\,L}{(U-2)\,t}\left(x_d - 0.0238\sqrt{\frac{(273+T)\,L\,x_d}{U-2}}\right) \tag{6}$$

where:

D_{nssm} – non-steady-state chloride migration coefficient [$\times 10^{-12}$ m^2/s],
T – average value of the initial and final temperatures in the anolyte solution [°C],
U – absolute value of the applied voltage [V],
L – thickness of the specimen [mm],
x_d – average value of the penetration depths [mm],
t – test duration [h].

The mathematical formulae (Eq. (5), Eq. (6)) were provided by Tang and Nilsson (in 1991) [28]. Equal (5) has been obtained as the analytical solution of the following equation (describing the flux of chloride ions due to diffusion and migration) (the Nernst–Plank equation) [2, 8, 19, 22, 28]:

$$J = J_D + J_M = -D\left(\frac{\partial C}{\partial x} - \frac{zFE}{RT}C\right) \tag{7}$$

where:

J – total flux of chloride ions [g/ m^2 s],
J_D – flux of chloride ions due to diffusion (the Fick's Law) [g/m^2 s],
J_M – flux of chloride ions due to electromigration (electrically forced migration) [g/m^2 s],
C – concentration of chloride ions [g/m^2],
x – distance from the surface exposed to the source solution of ions [m],
$\partial C / \partial x$ – concentration gradient (at position "x").
T – solution temperature [°K],
D, z, F, E, R – as shown in Eq. (5).

The chloride migration coefficient under non-steady-state (D_{nssm}) is used for evaluating the concrete resistance to chloride penetration, according to the criteria presented in Tab. 2 [15, 26]. The depth of chloride penetration itself may also be a useful parameter.

Table 2

Estimation of the concrete resistance to chloride ion penetration [15, 26]

Chloride migration coefficient *D* [m^2/s]	**Resistance to chloride penetration**
$< 2 \times 10^{-12}$	very good
$2 – 8 \times 10^{-12}$	good
$8 – 16 \times 10^{-12}$	acceptable
$> 16 \times 10^{-12}$	unacceptable

2.2. ASTM C 1202 and AASHTO T 277 test method

ASTM (American Society of Testing and Materials) C 1202 [29] and AASHTO (American Association of States Highway and Transportation Officials) T 277 [31] test, also known as the Rapid Chloride Permeability Test (RCPT) or the **Coulomb Test**, first developed by **Whiting** (in 1981) [30] is an easy to conduct and time-efficient test. To determine the permeability of concrete to chloride ions, the total charge passed through concrete during a 6-hour period under a 60 V potential difference is measured [8, 11, 18, 20]. Three specimens with the diameter of 100 mm and thickness of 50 mm (obtained by sawing the central part of 100 × 200 mm concrete cylinders) should be used. Before conditioning, the side of the concrete specimen is coated with epoxy. Then the specimen is placed in a vacuum chamber for 3 hours, vacuum saturated with water (de-aerated) for 1 hour and soaked for 18 hours (after turning off the pump). The procedure of sample preparation is the same as that in the NT Build 492 test, but the medium used for saturation is different (water in Coulomb Test versus $Ca(OH)_2$ in the NT Build 492 test). The **water saturated** concrete sample is placed in the test apparatus between two cells as shown in Fig. 5. One of the cells is filled with **3% NaCl** solution and the other cell is filled with **0.3 N NaOH** solution. The system is connected (the NaCl electrode is the cathode, the NaOH electrode is the anode) and a constant voltage of **60 V** DC is applied across the two sides of the sample for **6 hours**. The amount of charge passing through the specimen is measured by recording the current as a function of time. After 6 hours the total **charge** (in Coulombs) is determined by calculating the area under the plot of current versus time [1, 18, 20, 30, 31, 33]. The analysis of **chloride ion concentration in the anode cell** is also conducted by an ion chromatograph at specified intervals.

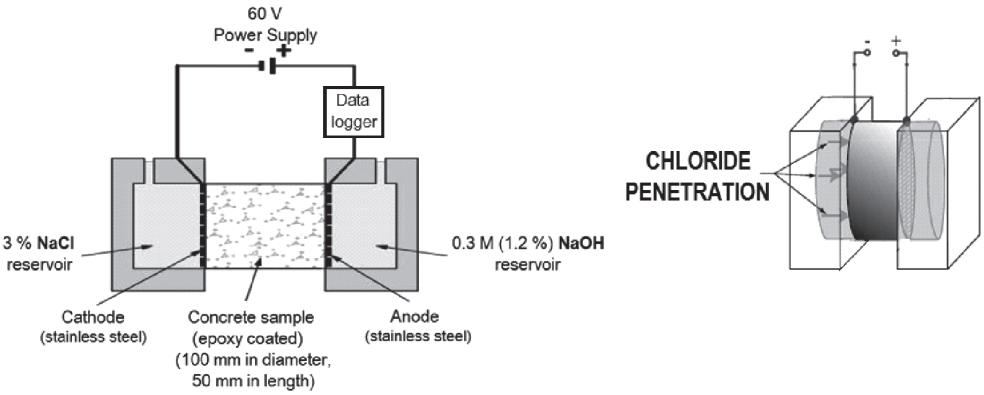

Fig. 5. Test of the chloride resistance of concrete – the ASTM C 1202 / AASHTO T 277 method. Test set-up [2, 22, 23, 30]

ASTM C 1202 [33] and AASHTO T 277 [31] specify the rating of chloride permeability of concrete based on the charge passed, as listed in Tab. 3 [20, 30, 31, 33]. For example, for bridge concrete, which should be of low chloride permeability (w/c ratio is less than 0.4), the required measurement result is between 1,000 and 2,000 Coulombs [9].

Table 3

Chloride permeability of concrete based on charge passed [18, 20, 30, 31, 33]

Charge [Coulombs]	Chloride permeability	Type of concrete
> 4,000	high	high water-to-cement ratio (> 0.5) conventional Portland cement concrete
2,000–4,000	moderate	moderate water-to-cement ratio (0.4–0.5) conventional Portland cement concrete
1,000–2,000	low	low water-to-cement ratio (< 0.4) conventional Portland cement concrete
100–1,000	very low	latex-modified concrete, internally sealed concrete
< 100	negligible	polymer-impregnated concrete, polymer concrete

The Rapid Chloride Permeability Test (ASTM C 1202 and AASHTO T 277 test) has been criticized by many scientists because the charge passed affects **all the ions**, not only **chloride ions** [1, 18, 20]. For concretes with fly ash, ground blast furnace slag, silica fume or other chemical additives the measured charge strongly depends on the composition of concrete (the chemistry of pore solution), i.e. the concentration of various ions (Cl^-, OH^-, SO_4^{2-}, Na^+, Ca^{2+}, etc.) in the pore solution. Due to the presence of the chemical additives the reduction in alkalinity of pore solution (before 90 days) can occur and concrete electrical conductivity (the amount of Coulombs) decreases [20]. The procedure is also under criticism because the high voltage applied (60 V) leads to an increase in temperature, which affects the amount of charge measured in the test [1]. Although the test of Tang and Nilsson (NT Build 492 test) obviates these problems, the ASTM C 1202 / AASHTO T 277 test is still widely used because it is so quick to administer [1, 20].

3. Chloride permeability of concrete – "In situ" test methods

"In situ" tests for the rapid assessment of concrete resistance to chloride ion penetration are very useful to control the durability of existing and newly constructed concrete bridges, pavements, marine structures, etc. [9]. "In situ" diagnosis of concrete is based on the procedures presented in the standards and it is carried out with the special testing set-up (e.g. the **Proove'it** system [35] (Fig. 6)).

The Proove'it system is typically used to measure the total charge passed according to ASTM C 1202 / AASHTO T 277 (the **Rapid Chloride Permeability Test**) (see Section 2.2). This rapid test takes 6 hours. But the system is also applied to conduct longer tests to determine the depth of chloride penetration in accordance with standard NT Build 492 (the **Rapid Chloride Migration Test**) (see Section 2.1).

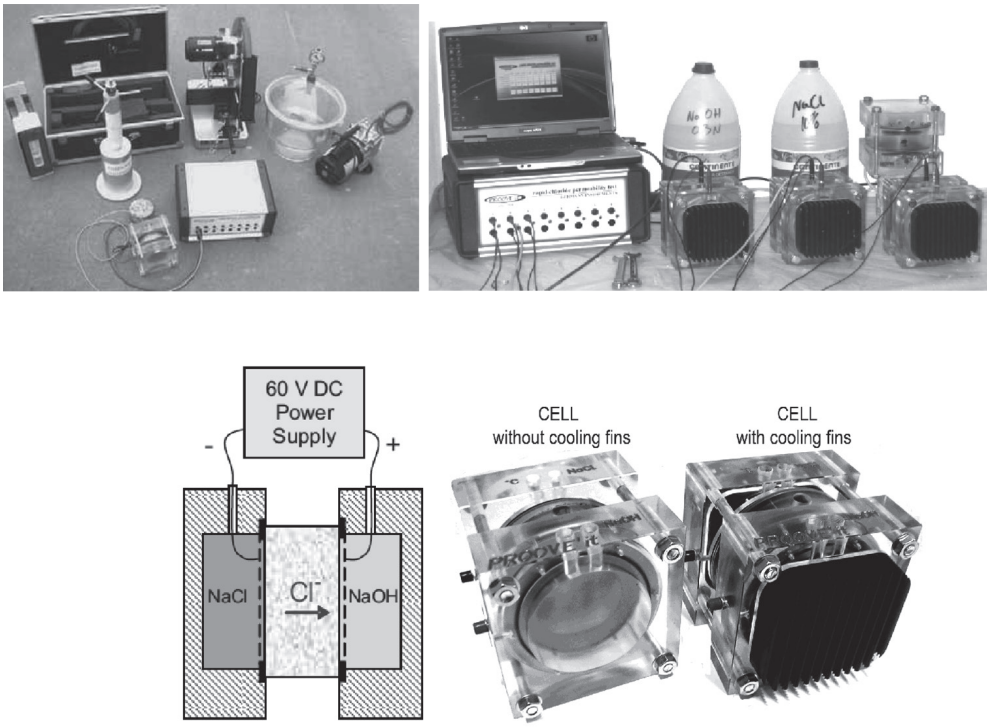

Fig. 6. Test of the chloride resistance of concrete – Proove'it system (with two types of Proove'it cells – with and without cooling fins) [21, 42]

The testing kit includes the following items (Fig. 6):

- moulds for cylindrical specimens (100 mm in diameter and 50 mm in length),
- electrodes (e.g. copper meshes),
- water cooled diamond saw,
- vacuum desiccator,
- vacuum pump,
- sealer (e.g. acrylic) + brush,
- cells (e.g. made of plexiglass) (each cell consists of two reservoirs) (two types – with or without cooling fins /ribs/; cooling fins are needed if the temperature is required to be kept constant, e.g. in the test of chloride ions migration, according to the NT Build 492),
- computer controlled microprocessor power supply,
- temperature probe,
- 3% NaCl solution (ASTM C 1202 test), 10% NaCl solution (NT Build 492 test),
- 0.3 N NaOH solution.

The example of the recorded results after completion of 8 simultaneous tests according to ASTM C 1202 / AASHTO T 277 (the Rapid Chloride Permeability Test) is presented in Fig. 7.

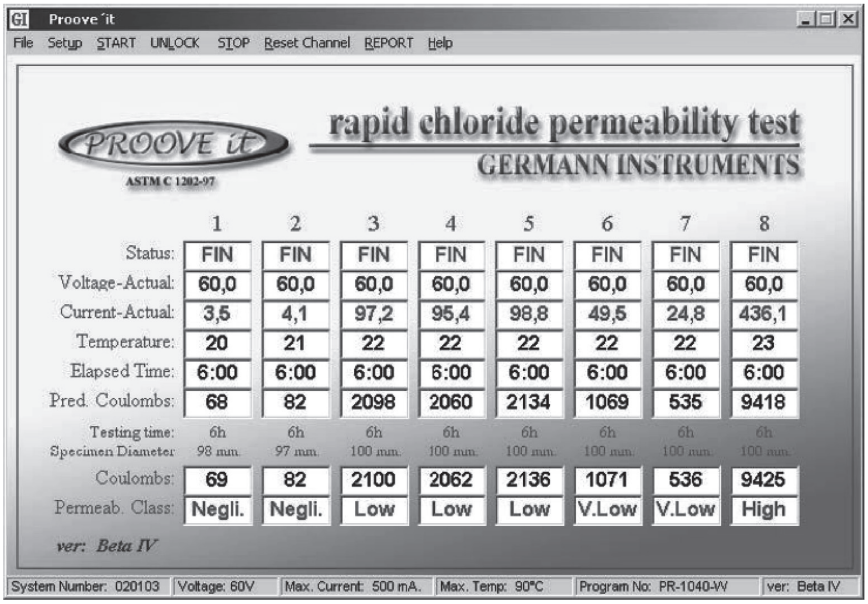

Fig. 7. Test of the chloride resistance of concrete – "Proove'it" system. Screen-shot after completion of 8 simultaneous tests according to the ASTM C 1202 [35]

The "Status" line (for the eight cells) is either OFF, ON or FIN (FIN indicates that the test has been completed). The "Voltage-Actual" line points out to the test voltage. The "Current--Actual" line shows the instantaneous current during testing. The "Temperature" line indicates the instantaneous temperature in the reservoir solutions during testing. The "Elapsed Time" line points out to the time since the start-up of each cell. The "Pred. Couloms" line shows the predicted Coulombs at 6 hours, which are estimated after every 5 minutes of testing. The "Testing time" indicates the selected testing time. The "Specimen Diameter" points out to the actual diameter of the specimen. The "Coulombs" line indicates the measured Coulombs at any time during testing. The last line shows the "Chloride ion permeability" classification according to ASTM C 1202.

4. Chloride content in concrete – "In situ" test method

An "in situ" diagnosis of the chloride ion content in concrete can be carried out with a special testing set-up, e.g. the Rapid Chloride Test (RCT) kit (Fig. 8) [41].

The **Rapid Chloride Test** (RCT) is fast and easy to perform. Both hardened and fresh concrete can be tested. A powder sample of hardened concrete, obtained from the structure by drilling and grinding, or a sample taken from fresh concrete is mixed with the extraction liquid in a plastic vial and shaken for 5 minutes. The liquid extracts the chloride ions. Then, a calibrated electrode is submerged into the solution (as shown in Fig. 8) to determine the amount of chloride ions, which is expressed as a percentage of concrete mass (the reading in mV is converted by means of the calibration chart to chloride content) [41].

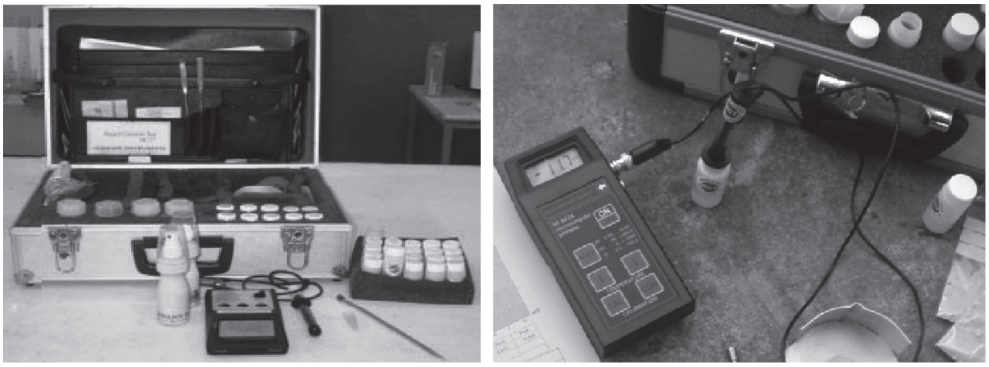

Fig. 8. Test of the chloride content in concrete – Rapid Chloride Test (RCT) system [41]

5. Concrete scaling caused by frost and de-icing salts – Standard test methods

When concrete freezes in the presence of a salt solution, **scaling** (the loss of material from the surface of concrete) can occur. Scaling does not occur if there is no free liquid on the surface of concrete, i.e. saturated concrete does not scale. Small particles of paste and mortar break away from the concrete, and the mass of broken particles increases with the number of cycles, gradually exposing the coarse aggregate [7, 17, 19]. Concrete roads and pavements exposed to deicing salts during winter or marine structures exposed to saline sea water are examples of applications in which salt-frost resistance concrete is required in order to prevent damage. To determine the concrete resistance to scaling, several standardized methods can be used [14, 32, 34]. The European standard **CEN/TS 12390-9** [34] presents three test methods: the **Slab** Test (reference method) and the alternative methods – the **Cube** Test and the **CDF** Test (**C**apillary suction of **D**e-icing solution and **F**reeze thaw Test). In the USA, the **ASTM C 672** method [32] is applied.

5.1. CEN/TS 12390-9 test method (Slab Test)

The standard **CEN/TS 12390-9**, **Slab** Test (**reference** method) [34] is based on the criteria in the Swedish standard SS 137244 – the Boraas method. The concrete durability (resistance) during freezing and thawing in the presence of de-icing salts (3% NaCl solution) is evaluated on the basis of the **mass** of scaled material **related to the concrete surface** subjected to the specified number of cycles of freezing and thawing.

Four **150 × 150 × 50 mm** specimens should be used in the test. A 50 mm thick specimen is sawn from a 150 mm concrete cube (perpendicular to the top surface so that the saw cut for the test surface is located in the centre of the cube – Fig. 9) after 21 days of concrete curing (1 day in the mould, protected against drying by use of a polyethylene sheet, 6 days in tap water at +20(±2)°C and 14 days in the climate chamber /+20(±2)°C and 65(±5)% of relative humidity/). When the concrete is 25 days old, a rubber sheet is glued to all surfaces of the specimen except the test surface. The edge of the rubber sheet should reach 20 mm above the test surface (Fig. 9). After fixing the rubber sheet the specimen is returned

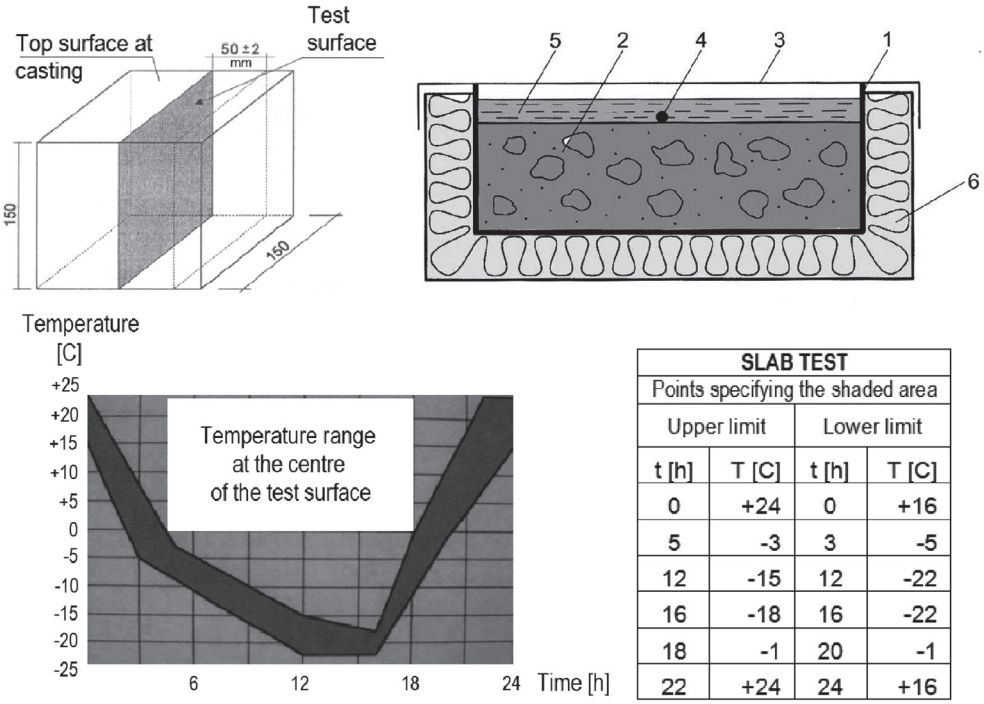

SLAB TEST			
Points specifying the shaded area			
Upper limit		Lower limit	
t [h]	T [C]	t [h]	T [C]
0	+24	0	+16
5	-3	3	-5
12	-15	12	-22
16	-18	16	-22
18	-1	20	-1
22	+24	24	+16

Fig. 9. Test of the concrete resistance to freezing and thawing in the presence of 3% NaCl. CEN/TS 12390-9 (Slab Test) method – Test set-up: 1 – rubber sheet, 2 – concrete specimen (150 × 150 × 50 mm), 3 – polyethylene sheet, 4 – temperature measuring device in contact with the test surface, 5 – freezing medium (3% NaCl solution), 6 – thermal insulation [15, 34, 40]

to the climate chamber. When the concrete is 28 days old, all surfaces of the specimen with the exception of the test surface are thermally insulated and the top exposed surface is covered with de-mineralized water for 72 hours. Directly before placing the specimen in the freezing chamber, water is replaced by **3% NaCl** solution (the freezing medium). The freezing medium is prevented from evaporating by applying a polyethylene sheet. Then the cooling and thawing cycles (each of 24 hours) are applied. During the test, the temperature (measured at the centre of the test surface) in the freezing medium shall remain within the shaded area shown in Fig. 9 (in the range from +20(±4)°C to –20(±2)°C). The scaled material is collected, dried and weighed after **56** freeze-thaw **cycles**; in some cases the test should end after 28 cycles, e.g. for precast concrete products (paving blocks [36], paving flags [37], kerb units [38]) or after 112 cycles in order to obtain the results after longer exposure. The mean mass of scaled material per unit area after 28, 56 and 112 cycles is used for evaluating the scaling resistance, according to the criteria presented in Tab. 4.

Table 4

Criteria of the scaling resistance evaluation [15]

Requirements	Scaling resistance
$m_{56} < 0.1$ kg/m^2	very good
$m_{56} < 0.2$ kg/m^2 or $m_{56} < 0.5$ kg/m^2 and $m_{56}/m_{28} < 2$ or $m_{112} < 0.5$ kg/m^2	good
$m_{56} < 1.0$ kg/m^2 and $m_{56}/m_{28} < 2$ or $m_{112} < 1.0$ kg/m^2	admissible
$m_{56} > 1.0$ kg/m^2 and $m_{56}/m_{28} > 2$ or $m_{112} > 1.0$ kg/m^2	inadmissible

5.2. CEN/TS 12390-9 test method (Cube Test)

In the **Cube** Test, described in standard **CEN/TS 12390-9** [34], cube specimens immersed in **3% NaCl solution** are subjected to freeze-thaw attack and the **mass loss** of the cubes after 56 freeze-thaw cycles is evaluated.

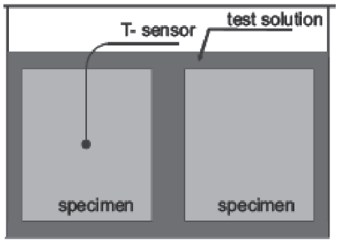

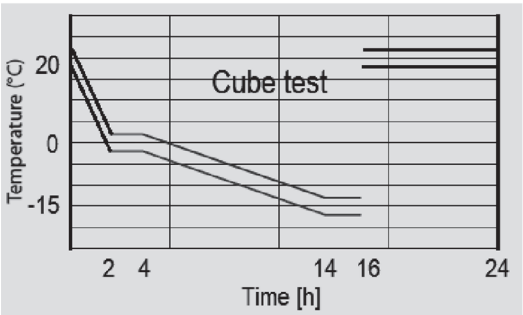

CUBE TEST			
Points specifying the shaded area			
t [h]	T [C]		
	Upper limit	Nominal value	Lower limit
0	+22	+20	+18
2	+2	0	-2
4	+2	0	-2
14	-13	-15	-17
16	-13	-15	-17

Fig. 10. Test of the concrete resistance to freezing and thawing in the presence of 3% NaCl. CEN/TS 12390-9 (Cube Test) method – Test set-up [34, 40]

The test requires four **100 mm** cubes. After 27 days (1 day in the moulds, covered by a polyethylene sheet, 6 days in tap water at +20(±2)°C and 20 days in the climate

chamber /+20(±2)°C and 65(±5)% of relative humidity/) the specimens are placed in two containers (2 containers with 2 cubes each = 4 cubes). The face which was uppermost during casting should be perpendicular to the base of the container. Each of two containers is filled with the freezing medium for 24 hours. The mass of freezing medium absorbed by each specimen in 24 hours is measured and the mean value of the four cubes is calculated. After 28 days the containers containing the cubes immersed in the freezing medium are placed in the freeze-thaw chests and freeze-thaw cycles are applied. After **56 cycles** of freezing and thawing (or 7, 14, 28, 42 cycles) (16 h air freezing between +20(±2)°C and -15(±2)°C and 8 h thawing in a water bath at +20(±2)°C /the range of temperature: within the shaded area shown in Fig. 10/) the percentage of mass loss is calculated for every two cubes in each container and the mean value of the two containers is determined to evaluate the scaling resistance. The tested concrete may be regarded as scaling resistant if the percentage loss of mass after 56 freeze-thaw cycles is less than 5%, as suggested by Boos and Giergiczny (who tested a range of concretes containing various cement types) [5].

5.3. CEN/TS 12390-9 test method (CDF test)

In the **CDF** Test (**C**apillary suction of **D**e-icing solution and **F**reeze thaw Test) (Fig. 11), presented in standard **CEN/TS 12390-9**, the scaling resistance is evaluated by the measurement of concrete mass scaled from specimens after 28 freeze-thaw cycles. The **mass** per 1 m^2 of the **test surface** is determined.

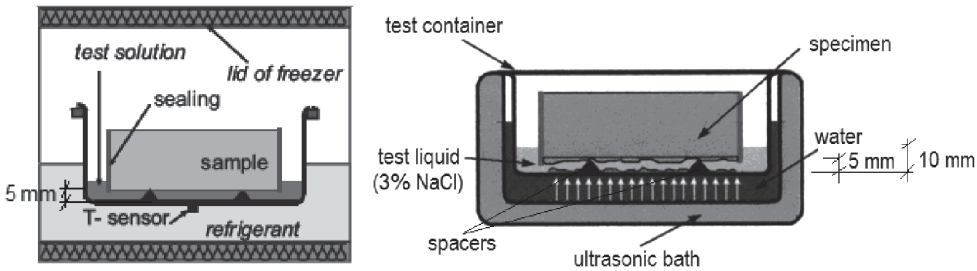

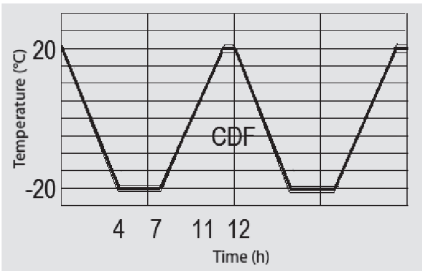

CDF TEST			
Points specifying the shaded area			
t [h]	T [C]		
	Upper limit	Nominal value	Lower limit
0	+21	+20	+19
4	-19.5	-20	-20.5
7	-19.5	-20	-20.5
11	+21	+20	+19
12	+21	+20	+19

Fig. 11. Test of the concrete resistance to freezing and thawing in the presence of 3% NaCl. CEN/TS 12390-9 (CDF Test) method – Test set-up [34, 40, 43]

Table 5

Overview of test methods according to CEN/TS 12390-9 [4, 5, 15, 34, 40]

Test parameter	**SLAB Test (reference method)**	**CUBE Test (alternative method)**	**CDF Test (alternative method)**
		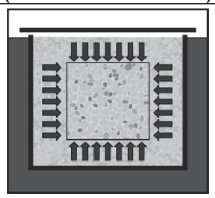	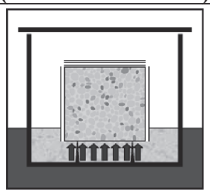
Curing conditions	1 day in the mould W – 6 days A – 21 days H – 3 days L – without contact	1 day in the mould W – 6 days A – 20 days H – without contact L – 1 day	1 day in the mould W – 6 days A – 21 days H – without contact L – 7 days
	W – under water A – in standard climate of 20°C/65% relative humidity H – in contact with water L – in contact with the freezing medium (3% NaCl) before freezing and thawing		
Number of specimens	4		5
Specimen dimensions [mm]	150 × 150 × 50	100 × 100 × 100	150 × 140 × 70
Test surface	cut (centre of the cube)	formed	
Tested specimen age	min 31 days	28 days	min 35 days
Test direction	one surface of the specimen tested from the top downwards	all surfaces of the specimen	one surface of the specimen tested from the bottom upwards
Tmax/Tmin	+20(±4)°C/-20(±2)°C	+20(±2)°C/-15(±2)°C	+20(±1)°C/-20(±0.5)°C
	measured in the test solution at the centre of the test surface	measured in the centre of the cube	measured below the test vessel
Freezing medium (test liquid/ solution)	3% NaCl		
Duration of one freeze-thaw cycle	24 hours		12 hours
Number of freeze-thaw cycles	56 cycles		28 cycles
Collecting the scaled material			ultrasonic bath for 3 minutes
Test criterion	mass of scaled material per 1 m^2 of concrete surface [kg/m^2]	the percentage loss of weight (mass) [% by mass]	mass of scaled material per 1 m^2 of concrete surface [kg/m^2]
Limit value [4, 5, 15]	< 1 kg/m^2 after 56 cycles	< 5% by mass after 56 cycles	< 1,5 kg/m^2 after 28 cycles

The **CDF** Test requires 5 specimens with the dimensions of **150 × 140 × 70 mm** (prepared by splitting a 150 mm cube mould with plates which have hydrophobic surfaces and a thickness of less than 5 mm; see the standard). The specimen are stored during 28 days (1 day in the mould, covered by a polyethylene sheet, 6 days in tap water at +20(±2)°C and 21 days in the climate chamber /+20(±2)°C and 65(±5)% of relative humidity/). After 21–26 days of storing, the side surfaces are either covered with aluminum foil glued with butyl rubber or sealed with epoxy resin (after this treatment the specimens are returned to the climate chamber). After 28 days each specimen is placed in the test container on the 5 mm high spacers with the test surface downwards (see Fig. 11). The freezing medium (**3% NaCl solution**) is poured into the container to the height of 10 mm. The pre-saturation by capillary suction lasts 7 days at the temperature of +20(±2)°C. Then, a number of 12 hour freeze-thaw cycles are applied. Two freeze-thaw cycles are carried out once a day. Starting at +20(±1)°C, the temperature is lowered to –20(±0.5)°C in 4 h and kept constant for 3 h. Then the temperature is increased to +20(±1)°C in 4 h and kept constant for 1 h (Fig. 11). After **28** freeze-thaw **cycles** (or 14 cycles), when the temperature is above 15°C, the specimen is placed in a ultrasonic bath for 3 minutes to remove any loose particles from the test surface. The scaled material is collected using a paper filter (see the standard). The mass of dried scaled material after 28 freeze-thaw cycles is determined in relation to the concrete surface exposed to the NaCl solution [kg/m^2]. The mean value of the five specimens is calculated to evaluate the scaling resistance. The tested concrete is considered to be scaling resistant, as proposed by Boos and Giergiczny [5], and also Beblacz and Kaminski [4], if the mass of scaled material per unit area after 28 freeze-thaw cycles is less than 1.5 kg/m^2.

The overview of the test methods presented in CEN/TS 12390-9 [4, 5, 34] is shown in Tab. 5.

5.4. ASTM C 672 test method

The ASTM C 672 method [32] is similar to the CEN/TS 12390-9 – Slab test.

ASTM C 672 requires two specimens (the surface area of at least 0.045 m^2 and the thickness of at least 75 mm, e.g. 300 mm × 200 mm × 90 mm [14]). The specimen is demoulded after 24 hours and subjected the standard moist curing for 13 days. Thereafter, the specimen is stored in air for 14 days (at standard room temperature of 23(±2)°C and 45–55% relative humidity). When the concrete is 28 days old, it is covered with **4% $CaCl_2$ solution** (cover thickness of 6 mm) [15].

The specimen is subjected to **50 freeze-thaw cycles**. Each cycle lasts 24 hours (16 to 18 h of freezing at around **-18**(±2)°C and 6 to 8h of thawing at **+23**(±2)°C and 45–55% relative humidity). Every five cycles the salt solution is washed off and replaced. A **qualitative** surface assessment (**visual evaluation** from 0 to 5, where "0" indicates "no scaling" and "5" indicates "severe scaling") is done in accordance with the classification presented in Tab. 6. In many laboratories loose scaled material is collected, dried and weighed at regular intervals during the test for a **quantitative** assessment of scaling apart from the subjective judgment of visual rating.

The ASTM C 672 exposure regime is reported to be harsh (4% $CaCl_2$ solution!) [4, 15].

Table 6

Test of concrete scaling – ASTM C 672 visual assessment [6, 15]

Rating	Condition of surface
0	No scaling
1	Very slight scaling (max 3 mm in depth, no coarse aggregate visible)
2	Slight to moderate scaling
3	Moderate scaling (some coarse aggregate visible)
4	Moderate to severe scaling
5	Severe scaling (coarse aggregate visible over entire surface)

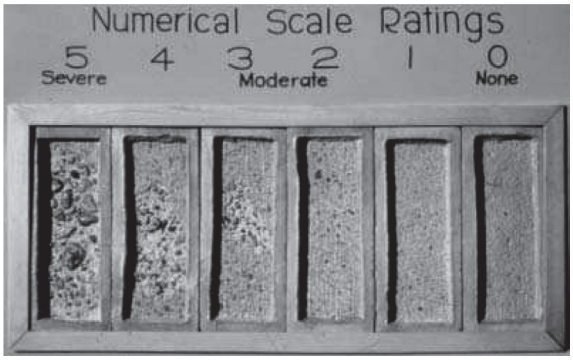

6. Conclusions

Chloride ingress in concrete structures induces corrosion and consequent concrete cracking, spalling, scaling, etc. The long service life of coastal structures, highways, bridges, pavements, etc. requires the concrete used to build them to be resistant to chlorides.

The paper provides details of the test methods (laboratory and applicable in-field) used to determine the chloride permeability of concrete, chloride ion content in concrete and concrete scaling due to cyclic freezing and thawing in the presence of NaCl solution (de-icing salts, saline sea water, etc.).

The most common laboratory test methods used to determine the resistance of concrete to the penetration of chloride ions: the NT Build 492 (NordTest) – the Rapid Chloride Migration Test (RMT) (popular in Europe, including the Polish laboratories) and the ASTM C 1202/ AASHTO T 277 Test – the Rapid Chloride Permeability Test (RCPT) (widespread in the USA and Canada) are described in the paper, specifying the major differences between them (in concentration of the NaCl solution: 3% – RMT, 10% – RCPT, in voltage: 30 V – RMT, 60 V – RCPT and in the test duration: 6 – 96 hours, usually 24 hours – RMT, 6 hours – RCPT), and emphasizing the fact that the tests are non-steady state tests (in reality, chloride penetration into concrete is a non-steady-state process). The paper also

points out to certain disadvantages of the Rapid Chloride Permeability Test: the charge passed is related not only to chloride ions, but to all the ions present in the pore solution (e.g. Cl^-, OH^-, SO_4^{2-}, Na^+, Ca^{2+}, etc.) whose concentration may vary in different pozzolanic concretes and the high voltage applied (60 V) leads to an increase in temperature, which affects the amount of charge measured in the test. Nevertheless, the Rapid Chloride Permeability Test is widely used because it is so quick. The special testing set-up (e.g. the Proove'it system) applied for a quick and easy "in situ" diagnosis of the resistance of concrete to chloride ion penetration (in existing and newly constructed concrete bridges, pavements, marine structures, etc.) is based on the procedures presented in the RCPT. The Proove'it system can be used either to measure the total charge passed (in the RCPT) or the depth of chloride penetration (in the RMT). Besides, the paper describes the "in situ" test (fast and easy to perform) for chloride ion content in concrete which can be carried out with e.g. the Rapid Chloride Test (RCT) kit.

Moreover, the paper reviews the test methods for estimation of concrete resistance to scaling during freezing and thawing in the presence of de-icing salts: the Slab Test (based on the criteria in the Swedish standard SS 137244 – the Boraas method) – as the reference method and the Cube Test and the CDF Test (Capillary suction of De-icing solution and Freeze thaw Test) as alternative methods described in the European standard CEN/TS 12390-9 as well as the ASTM C 672 method. All the above-mentioned methods are applicable to the specimens cast in a laboratory or drilled from field structures. It should be noted that there is no correlation between the results obtained from these test methods, because the test procedures are different.

In all the three European standardized methods, the temperature range of freezing and thawing (from +20°C to –20°C) is identical. Another factor that is comparable are curing conditions. The methods differ in all the other parts of the procedure regarding concrete preservation before the test, the properties of test specimens (age, number, shape, dimensions, production/casting, etc.), the way in which the test surface is prepared, the characteristics of freeze-thaw cycles (number, duration, upper and lower limits for temperature, evolution of temperature, etc.), the surface of the test specimen in contact with the test liquid (NaCl) (upper or lower face or fully immersed test specimen), the type of thaw salt (NaCl or $CaCl_2$; most typically 3% NaCl solution is used as it is most critical for the degree of surface scaling), the position of the temperature sensor (at the centre of the test surface, in the centre of the specimen, below the test vessel), the way in which the scaled material is collected (by rinsing or ultrasonic cleaning), the way in which the test specimens are cooled off (with air or liquid), etc. (Tab. 5) [40]. In all the three tests there is no recommendation for limit values. However, the paper specifies the suggested limit values presented in the literature on the subject [4, 5, 15].

The paper also attempts to provide a brief analysis of each test method. The Slab Test is used to test e.g. concrete paving elements (the freezing in this method progresses verically from top to bottom, i.e. in the way that resembles the naturally occurring freezing cycles). The main disadvantage of the Slab Test and the Cube Test methods is the long duration of the study (56 days). In the case of the Slab Test the short duration of action of the lowest temperature entails too mild testing conditions (in cold regions, the temperature of a concrete structure may remain at sub-freezing levels for longer periods of time). In the CDF Test method the scaling resistance is evaluated quite soon – after 14 days (28 freeze-thaw cycles, each of 12 hours). In all three European standardized methods the process of sample

preparation is laborious. The paper also illustrates several shortcomings of the ASTM C 672 method. The ASTM C 672 method has been criticized because the salt solution is not covered with a plastic sheet and thus not protected against evaporation, the time of freezing and thawing is not precisely specified, the exposure regime is harsh (50 freeze-thaw cycles, the presence of 4% $CaCl_2$ solution), and the visual, qualitatively evaluation of scaling is a subjective assessment (the rating scale can only be used for a relative comparison of concretes whereas the assessment of scaling in the European standard CEN/TS 12390-9 methods is quantitative). However, the tests have also been criticized for the short period of pre-saturation, which can be insufficient for concrete with e.g. slag cement (because it can produce the osmotic effect).

A deterioration process takes years in the field, but in the laboratory it may take only weeks. Natural conditions are varied, complex and extremely difficult to reproduce. Tests usually amplify the severity of exposure conditions and consequently the damage of the material. It is hard to represent true field conditions in a laboratory test. The basic reason for the severity of most laboratory tests is unlimited access to water at all time, which is not always the situation in the field. The moisture content of the specimens and also the maturity of concrete at the test beginning are important factors related to concrete durability.

A comparative analysis of the test results derived from both laboratory and field studies may indicate the most suitable method for a given type of concrete. The choice of method should depend, on the one hand, on the environmental conditions in which the material works and, on the other hand, it should be based on the expertise obtained in the course of concrete laboratory testing [24–26]. The more experience is gained with the tests, the more appropriate procedures for determining chloride permeability are invented. So, modified and new test methods are undoubtedly to be expected in the nearest future.

References

[1] Andrade C., *Calculation of chloride diffusion coefficients in concrete from ionic migration measurement*, Cement and Concrete Research, Vol. 23, 1993, 724–742.

[2] Audenaert K., Yuan Q., De Schutter D., *On the time dependency of the chloride migration coefficient in concrete*, Construction and Building Materials, Vol. 24, 2010, 396–402.

[3] Baroghel-Bouny V., Belin P., Maultzsch M., Henry D., *$AgNO_3$ spray test: advantages, weaknesses, and various applications to quantify chloride ingress into concrete*, Part 2: *Non-steady-state migration tests and chloride diffusion coefficients*, Materials and Structures, No. 8, Vol. 40, 2007, 783–799.

[4] Bebłacz D., Kamiński P., *Methodology of testing and assessment criteria of resistance of pavement concretes to de-icing salts*, 3rd Conference "Concrete Days" ("Dni Betonu"), Wisła, Poland, 11–13 October, 2004, 804–821 (in Polish).

[5] Boos P., Giergiczny Z., *Testing the frost resistance of concrete with different cement types – experience from laboratory and practice*, Architecture-Civil Engineering-Environment, The Silesian University of Technology, No. 2, 2010, 41–51.

[6] Bortz B.S., *Salt-scaling durability of fly ash concrete*, M.Sc. Thesis, Kansas State University, Manhattan, Kansas 2010.

[7] Brandt A.M., *Cement based composites: materials, mechanical properties and performance*, Taylor&Francis, 2009.

[8] Claisse P.A., Elsayad H.I., Ganjian E., *Modelling the rapid chloride permeability test*, Cement and Concrete Research, Vol. 40, 2010, 405–409.

[9] Flaga K., *Diagnosis of concrete bridges*, Bridges, No. 1, 2011, 48–53 (in Polish).

[10] Flaga K., *In-situ test methods in the diagnosis of the state of concrete in engineering structures*, 2nd Scientific and Technical Symposium on Durability of Concrete, Cracow, April 2008, 121–139 (in Polish).

[11] Giergiczny Z., *Test methods for corrosion resistance of concrete to chloride and sulphate*, 2nd Scientific and Technical Symposium on Durability of Concrete, Cracow, April 2008, 77–96 (in Polish).

[12] He F., Shi C., Yuan Q., Chen Ch., Zheng K., *$AgNO_3$ – based colorimetric methods for measurement of chloride penetration in concrete*, Construction and Building Materials, Vol. 26, 2012, 1–8.

[13] Hearn N., Hooton R.D., Nokken M.R., *Pore structure, permeability and penetration resistance characteristics of concrete*, [in:] J.F. Lamond, J.H. Pielert (eds.), *Significance of tests and properties of concrete & concrete-making materials*, Chapter 23, ASTM STP 169D, 2006, 238-252.

[14] Hooton R.D., Vassilev D., *Deicer scaling resistance of concrete mixtures containing slag cement. Phase 2: Evaluation of different laboratory scaling test methods*, Iowa State University/Federal Highway Administration, USA, Report No. DTFH61-06-H-00011 (Work Plan 24), July 2012.

[15] Jóźwiak-Niedźwiedzka D., *Effect of fluidized bed combustion fly ash on the chloride resistance and scaling resistance of concrete*, RILEM TC 211-PAE Final Conference on Concrete in Aggressive Aqueous Environments. Performance, Testing and Modeling, Toulouse, France, 3–5 June, 2009, Vol. 2, 556–563.

[16] Jóźwiak-Niedźwiedzka D., *Frost resistance test methods*, 2nd Scientific and Technical Symposium on Durability of Concrete, Cracow, April 2008, 161–181 (in Polish).

[17] Kurdowski W., *Cement and concrete chemistry*, Polish Cement Association, Cracow/Polish Scientific Publishers (PWN), Warsaw 2010 (in Polish).

[18] Ramachandran V.S., Beaudoin J.J., *Handbook of analytical techniques in concrete science and technology*, Noyes Publications/William Andrew Publishing, New York 2001.

[19] Richardson M.G., *Fundamentals of durable reinforced concrete*, Spon Press, 2002.

[20] Shi C., *Effect of mixing proportions of concrete on its electrical conductivity and the rapid chloride permeability test (ASTM C 1202 or ASSHTO T 277) results*, Cement and Concrete Research, Vol. 34, 2004, 537–545.

[21] Sillanpää M., *The effect of cracking on chloride diffusion in concrete*, M.Sc. Thesis, Aalto University, Espoo, Finland 2010.

[22] Spiesz P., Brouwers H.J.H., *Analysis of the theoretical model of the Rapid Chloride Migration test*, 8th International Ph.D. Symposium in Civil Engineering, The Technical University of Denmark, Kgs. Lyngby. Denmark, 20–23 June, 2010, (online) homepage: http://josbrouwers.bwk.tue.nl/publications/Conference64.pdf, (access: 12.03.2014).

[23] Stanish K., Hooton R.D., Thomas M.D.A., *A novel method for describing chloride ion transport due to an electrical gradient in concrete*, Part 2: *Experimental study*, Cement and Concrete Research, Vol. 34, 2004, 51–57.

[24] Szweda Z., Zybura A., *Analysis of chloride diffusion and migration in concrete*, Part I: *Theoretical model*, Architecture – Civil Engineering – Environment, Silesian University of Technology, Vol. 5, No. 1, 2012, 47–54.
[25] Szweda Z., Zybura A., *Analysis of chloride diffusion and migration in concrete*, Part II: *Experimental tests*, Architecture – Civil Engineering – Environment, Silesian University of Technology, Vol. 5, No. 1, 2012, 55–62.
[26] Tang L., *Chloride transport in concrete – Measurement and prediction*, Ph.D. Thesis, Chalmers University of Technology, Gothenburg, Sweden, Publication P-96:6, 2010.
[27] Tang L., Nilsson L.-O., *Prediction of chloride penetration into concrete by using the computer program "ClinConc"*, [in:] O.E. Gjørv, K. Sakai, N. Banthia (eds.), *Concrete under severe conditions 2. Environment and loading*, E & FN Spon, Vol. 1, 1998, 625–634.
[28] Tang L., Nilsson L.-O., *Rapid determination of the chloride diffusivity in concrete by applying an electrical field*, ACI Materials Journal, Vol. 89, 1992, 49–53.
[29] Tang L., Nilsson L.-O., Basheer P.A.M., *Resistance of concrete to chloride ingress*, Spon Press, 2011.
[30] Whiting D., *Rapid determination of the chloride permeability of concrete*, Federal Highway Administration, USA, Report No. FHWA/RD-81/119, August 1981.
[31] AASHTO T 277 (2007). Standard method of test for electrical indication of concrete's ability to resist chloride ion penetration, AASHTO (American Association of State Highway and Transportation Officials), USA.
[32] ASTM C 672 (2012). Standard test method for scaling resistance of concrete surfaces exposed to deicing chemicals, ASTM (American Society for Testing and Materials), USA.
[33] ASTM C 1202 (2012). Standard test method for electrical indication of concrete's ability to resist chloride ion penetration, USA.
[34] CEN (European Committee for Standardization). CEN/TS 12390-9:2006. Testing hardened concrete – Part 9: Freeze-thaw resistance – Scaling (PKN-CEN/TS 12390-9:2007E – in Polish).
[35] EN 206-1:2000. Concrete – Part 1: Specification, performance, production and conformity (PN-EN 206-1:2003P – in Polish).
[36] EN 1338:2003/AC:2006. Concrete paving blocks. Requirements and test methods (PN-EN 1338:2005/AC:2007P – in Polish).
[37] EN 1339:2003/AC:2006. Concrete paving flags. Requirements and test methods (PN-EN 1339:2005/AC:2007P – in Polish).
[38] EN 1340:2003/AC:2006. Concrete kerb units. Requirements and test methods (PN-EN 1340:2004/AC:2007P – in Polish).
[39] NT BUILD 492 (1999). NordTest Method: Concrete, mortar and cement-based repair materials: Chloride migration coefficient from non-steady-state migration experiments, Finland.
[40] http://www.crr.be/pdf/15/webpages/e03c.pdf (access: 12.03.2014).
[41] http://www.germann.org/Brochures/Catalog-NDT-2010.pdf (access: 12.03.2014).
[42] http://www.germann.org/TestSystems/PROOVEit/PROOVEit.pdf (access: 12.03.2014).
[43] http://www.uni-due.de/ibpm/projekte/CIF-eng.pdf (access: 12.03.2014).

CONTENT

TREŚĆ